Numerical study of a channel flow including a surface-mounted fence and particles

G.J.G. Pouls

MEAH - 225

Delft, march 2003

Laboratory for Aëro- and Hydrodynamics
Subfaculty of Applied Physics
Faculty of Applied Sciences
Delft University of Technology

Graduation committee:
Prof. Dr. Ir. F.T.M. Nieuwstadt
Dr. Ir. M.J.B.M. Pourquié
Dr. Ir. B.A. van Haarlem
Dr. Ir. W.S.J. Uijttewaal
Dr. Ir. J.J. Derksen

Chapter 1

Abstract

Exhaust gasses flowing flowing through catalyst reactors often contain fine dirt particles, like for example soot. These particles clog the reactor in due time. It would be very helpful if these particles could somehow be separated from the flow upstream of the reactor. One idea to improve separation is by placing obstacles in the channel flow.

In this numerical study we focus on using fences as obstacles. We make use of Large Eddy Simulation (LES) and RANS simulation to simulate a channel flow with one or two fences.

In one case a high fence is placed close after a low fence. The second fence is intended for particles to collide with and get caught in the wake between the fences. We find this idea not to work for particular particles.

A second case consists again of two fences, but now with equal heights placed far apart. The idea is for particles to get caught in vortices shedded from the first fence and to deposit near the second fence where the vortices break up. We find the shedding phenomenon to be very sensitive for various parameters most notably the Reynolds number, making the idea hard to implement. It seems the idea is hardly beneficial to separation.

Concerning the RANS simulations, we find that the Re-stress model is only able to correctly simulate a fence flow when no vortex shedding takes place. The $k-\epsilon$ model is found to incorrectly simulate the flow even when no vortices are present. The LES seems to predict fence flow well, but no hard conclusions could be made.

Chapter 2

Symbols

Symbol	Description	Unit
δ	Boundary layer thickness	m
η	Kolmogorov length scale	m
ϵ	Viscous dissipation rate	Nm/s
μ	Dynamic viscosity	kg/ms
μ_t	Eddy viscosity	-
ν	Kinematic viscosity	m^2/s
ρ	Fluid density	kg/m^3
ρ_p	Particle density	kg/m^3
τ_p	Particle relaxation time	-
τ_v	Time scale associated with vortex	-
τ_w	Wall shear stress	N/m^2
a	Particle radius	m
$\mathbf{a}$	Particle acceleration	m/s^2
C_D	Drag coefficient	-
$E_{subgrid}$	Dimensionless subgrid energy	-
f	Shedding frequency	s^{-1}
g	Gravity acceleration	m/s^2
$\mathbf{F}$	Force	N
H	Height of the channel	m
h	Height of the fence	m
k	Kinetic energy	Nm
$\mathcal{L}$	Length scale	m
L	Length of channel	m
l	Thickness of the fence	m
l_{mix}	Mixing length	-
m_f	Mass of the fluid displaced by a particle	kg
m_p	Mass of particle	kg
Pe	Grid Peclet number	-
p	Pressure	Pa
Re_h	Reynolds number based on the fence height and bulk velocity	-
Re_H	Reynolds number based on the channel height and bulk velocity	-
Re_p	Particle Reynolds number based on the particle radius and the relative particle velocity.	-
Re_*	Reynolds number based on the shear velocity and channel height	-
r	Vortex radius	m
St	Stokes number	-
Str	Strouhal number	-

Symbol	**Description**	**Unit**
t	Time	s
$\mathcal{U}$	Velocity scale	m/s
U_0	Bulk velocity	m/s
U_{inf}	Upstream velocity	m/s
$\mathbf{u}$	Fluid velocity	
$\mathbf{u_p}$	Particle velocity	
u	Velocity component in streamwise direction	m/s
u_*	Shear velocity	m/s
v	Velocity component in spanwise direction	m/s
w	Velocity component in normal direction	m/s
x	Distance in streamwise direction	m
$\mathbf{x_p}$	Particle position	m
x_R	Reattachment length	m
y	Distance in spanwise direction	m
z	Distance in normal direction	m
z_+	Distance to the wall in wall units	-

Contents

Chapter 3

Introduction

Often in the process industry exhaust gasses contain certain components that must be removed in order to comply with emission standards. Various catalyst reactors exist for this purpose, most notably the packed-bed reactor. This type of reactor consists of a shell made of wire netting filled with catalyst grains. The exhaust gas flows through the space inbetween the grains in order for the desired components to diffuse into these grains where a chemical reaction takes place. However the packed-bed reactor has a big drawback. It is not suitable for gas flows containing fine particles, like for example soot. Such gas flows would clog the reactor in due time. It would be very helpful if these particles could somehow be separated from the flow upstream of the reactor. One idea to improve separation is by placing obstacles in the channel flow. This constitutes the practical idea behind this study.

In this study we focus on one particular kind of obstacle, namely a fence. First we aim at increasing our understanding of flow phenomena related to a channel with a surface-mounted fence. Such a fence flow falls under the general heading of separating and reattaching flows. These include separated boundary layers, flow over a backward-facing step and flow over a normal flat plate attached to a splitter plate. All these flows share some common characteristics apart from the basic structure of a large recirculation zone.

The flow over a surface-mounted fence has several features that distinguish it from the other separated and reattaching flows. Unlike the separated boundary layer, the separation point in the flow over such an obstacle is fixed and is not expected to fluctuate. Unlike the flow over the backward-facing step, the flow is accelerated over the separation point and continues to accelerate part of the way to reattachment. Also, because of the geometry, the shear layer has more curvature than the shear layer formed in the flow over a backward facing step. In figure 3.1 a sketch by Leonardo da Vinci is shown for flow over a fence. Apparently fence flow was already a subject of investigation some centuries ago. What Da Vinci meant to indicate with the three recirculation zones is unclear. Maybe he tried to depict the wake behind the fence, a region of turbulence or he tried to depict shedded vortices.

Another aim of this study is to investigate the possibility of using a fence to entrain particles. We hope to gain some insight in the usefulness of the fence for the application discussed above. We concentrate on two scenarios for entraining the particles.

In the first one, two fences are present in the channel. The first somewhat smaller fence is used to concentrate the particles in the shear layer of the wake. The second somewhat larger fence is placed at such a position, that the particles collide with it. They are supposed to get caught in the wake between them.

The second scenario is based on the principle found in a patent [5] by Wai and Rogers. They found that a surface-mounted fence in a channel flow sheds vortices under certain circumstances. This finding is also observed by others, for example Lee [7]. The patent tells us that certain sizes of particles will accumulate in these vortices. A second fence is then placed further downstream to destroy these vortices through which the particles will deposit in the vicinity of this second fence.

This study is done numerically using both Large Eddy Simulation (LES) and RANS-simulations.

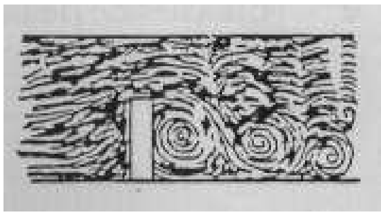

Figure 3.1: *Sketch by Leonardo da Vinci from his Codex Leicester (1506-1510).*

The RANS-simulations are performed with the commercial CFD package FLUENT 6. Our third aim for this study is to make a comparison between the LES and RANS turbulence models and to find out whether or not these RANS simulations simulate a fence flow well enough. If so they can be used in the industry to simulate these flows instead of a time consuming LES.

Summarizing we have three goals for this study. First of all we want to study the general flow behaviour for a channel with a surface-mounted fence. Second we want to say something about the usage of a fence to extradite particles from the flow. And third we want to make a comparison between a LES and simulations using turbulence models.

Chapter 4

Theory

4.1 Turbulent Channel Flow

Turbulent flow is the most common type of flow encountered in nature. It does not look anything like laminar flow. A laminar flow is a flow in which the fluid moves in layers without any fluctuations. In turbulent flow however the fluid moves in irregular paths. Such a flow is not totally without structure due to the existence of whirling structures, called eddies. The presence of structure implies that the velocity of the flow, measured in two different points, is correlated as a function of space but also as a function of time.

In turbulent flow two scales are of importance, namely a macro scale and a micro scale. The macro scale, defined by the large dimensions of the flow, consists of large eddies with energy taken from the mean flow via an instability process. These large eddies break up into smaller eddies in what is called the cascade-process. The smallest eddies are found in the micro scale, defined by the smallest dimensions in the flow. In this microstructure the energy of the eddies is dissipated into heat through the effect of viscosity. Turbulence on this scale is isotropic.

In this study, a turbulent channel flow is considered which is incompressible as well as isothermal. See figure 4.1. Such a channel flow without a fence is described by the equations for conservation of mass and momentum:

$$\nabla \cdot \mathbf{U} = 0 \tag{4.1}$$

$$\frac{D\mathbf{U}}{DT} = \mathbf{g} - \frac{1}{\rho}\nabla P + \nu\nabla^2\mathbf{U} \tag{4.2}$$

with $\mathbf{U}$ the fluid velocity, ρ the fluid density, P the pressure and ν the kinematic viscosity. The material derivative $\frac{D}{DT}$ is defined by

$$\frac{D}{DT} = \frac{\partial}{\partial T} + \mathbf{U} \cdot \nabla \tag{4.3}$$

The equations 4.1 and 4.2 form a closed set of equations and will be referred to as the Navier Stokes equations.

In order to write these equations in a dimensionless form, a characteristic length and velocity scale must be found. From these two, a characteristic time scale can be defined. For a channel flow, the channel height H is taken for the length scale. For the velocity scale, the shear velocity u_* is used:

$$u_* = \sqrt{\frac{\tau_w}{\rho}} \tag{4.4}$$

where τ_w is the wall shear stress and ρ the fluid density. The time scale then becomes $t^* = H/u_*$. Using these characteristic scales, we can define dimensionless variables and substitute these in the Navier Stokes equations. This results in the dimensionless form of the equations for conservation of mass and momentum:

$$\nabla \cdot \mathbf{u} = 0 \tag{4.5}$$

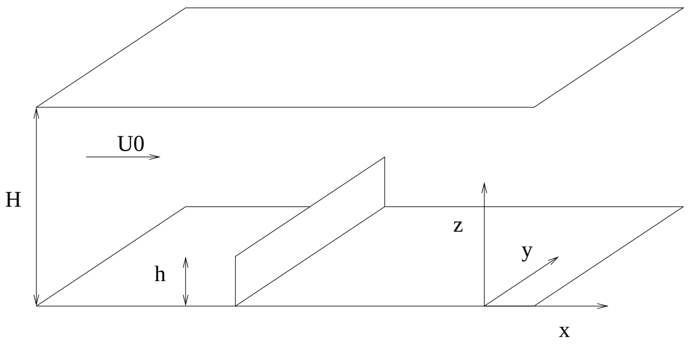

Figure 4.1: *Geometry used in this study of the channel with a surface-mounted fence.*

$$\frac{D\mathbf{u}}{Dt} = -\nabla p + \frac{1}{Re_*}\nabla^2\mathbf{u} + F \tag{4.6}$$

where F is an extra constant pressure gradient term which drives the flow. Re_* is the Reynolds number. In this geometry it is defined as

$$Re_* = \frac{u_* H}{\nu} \tag{4.7}$$

The wall shear stress can be written as:

$$\tau_w = -H * F \tag{4.8}$$

In the simulations of a channel including a fence, a velocity field is prescribed on the inlet and we do not longer need the constant pressure gradient F to drive the flow.

4.2 Numerical Method

In this section we look at some numerical aspects.

4.2.1 Finite volume method

In a channel flow the dimensionless Navier-Stokes equations 4.5 and **??** are used, which can be written in the following form:

$$\frac{\partial \mathbf{u}}{\partial t} = \mathrm{Adv} + \mathrm{Diff} - \nabla p \tag{4.9}$$

where $\mathrm{Adv} = -\mathbf{u} \cdot \nabla \mathbf{u}$ is the advection term and $\mathrm{Diff} = \nu \nabla^2 \mathbf{u}$ is the diffusion term. Both terms will be discretised using the finite volume method. This method consists of integrating the equations of motion over a grid volume. The first step is to use the Gauss theorem to reduce the volume integrals to surface integrals. Next all quantities are approximated with the aid of the midpoint rule. This leaves a set of discretised equations of second order accuracy. However the time derivatives are still not discretised.

For the temporal discretisation we use an explicit second-order Adams-Bashforth scheme. Applying this scheme to (4.9) we get for the time derivative

$$\frac{\mathbf{u}^{n+1} - \mathbf{u}^n}{\Delta t} = \frac{3}{2}[\mathrm{Adv} + \mathrm{Diff}]^n - \frac{1}{2}[\mathrm{Adv} + \mathrm{Diff}]^{n-1} - \nabla p \tag{4.10}$$

where n refers to the discrete time level $n\Delta t$, with Δt the discrete time step. This time step is determined using a stability criterion

$$\Delta t = \frac{\alpha}{\frac{|u|}{\Delta x} + \frac{|v|}{\Delta y} + \frac{|w|}{\Delta z} + \nu(\frac{1}{\Delta x^2} + \frac{1}{\Delta y^2} + \frac{1}{\Delta z^2})} \tag{4.11}$$

In this study the α has a value of $\alpha = 0.3$, a value which should guarantee a stable solution. To ensure continuity for the numerical solution of the discretised equation a pressure correction method is used. The first step, i.e. the predictor step, consists of determining a predicted velocity $\mathbf{u}^*$ from (4.10). Generally mass is not conserved in the intermediate velocity field $\mathbf{u}^*$ or in other words the continuity equation is not satisfied. For this we use a pressure equation

$$\frac{\mathbf{u}^{n+1} - \mathbf{u}^*}{\Delta t} = -\nabla p' \tag{4.12}$$

where $\Delta p'$ is the fluctuating pressure field. When $\nabla \cdot \mathbf{u}^{n+1} = 0$ then (4.12) can be rewritten as

$$\nabla^2 p' = \frac{\nabla \cdot \mathbf{u}^*}{\Delta t} \tag{4.13}$$

Once this pressure has been calculated, the corrected velocity $\mathbf{u}^{n+1}$ follows from the corrector step

$$\mathbf{u}^{n+1} = \mathbf{u}^* - \Delta t \nabla p' \tag{4.14}$$

And in this corrected velocity field, mass is conserved.

4.2.2 Large eddy simulation

The advantage of solving turbulence problems numerically, instead of experimentally, is the fact that the total 3-dimensional velocity field is solved and quantities that are difficult to measure, like pressure, can be calculated relatively easy. One way to simulate the turbulence is to use a Direct Numerical Simulation (DNS) of the flow. However, this method is only applicable for low Reynolds numbers due to limited computer power. To study flows with high Reynolds numbers a Large Eddy Simulation (LES) can be used. In LES the large scale turbulent structures are solved directly. A filter is used to get rid of the smaller structures and their influence on the large scale structures is taken into account by a so-called subgrid model.

A spatial filter is applied to the velocity field in order to remove the small scale eddies. This way, only the remaining large scales need to be resolved for LES. Each flow variable can be decomposed in

$$\phi = \phi_{GS} + \phi_{SGS} \tag{4.15}$$

where ϕ_{SGS} is the subgrid component in the subgridscale (SGS), and ϕ_{GS} the variable component as defined by the gridscale (GS). This ϕ_{GS} is defined by making use of a spatial moving average filter

$$\phi_{GS}(\mathbf{x}, t) = \int_V G(\mathbf{x} - \mathbf{x}')\phi(\mathbf{x}', t)d\mathbf{x}' \tag{4.16}$$

where $G(\mathbf{x} - \mathbf{x}')$ is a spatial filter function. When we apply this filter operation to the velocity $\mathbf{u}$, the dimensionless Navier-Stokes equations for the gridscale velocity $\mathbf{u_{GS}}$ become

$$\nabla \cdot \mathbf{u_{GS}} = 0 \tag{4.17}$$

$$\frac{\partial \mathbf{u_{GS}}}{\partial t} + \nabla(\mathbf{u_{GS}}\mathbf{u_{GS}}) = -\nabla p_{GS} + \frac{1}{Re_*}\nabla^2\mathbf{u_{GS}} - \nabla\tau \tag{4.18}$$

with τ the subgrid stress tensor is given by

$$\tau = (\mathbf{uu})_{GS} - \mathbf{u_{GS}}\mathbf{u_{GS}} \tag{4.19}$$

This tensor represents the influence of the subgridscale motion on the gridscale velocity in the form of stress. Because τ is still dependent on $\mathbf{u}$ and thus on $\mathbf{u_{SGS}}$, we have to find a model which describes τ in terms of $\mathbf{u_{GS}}$. The first step is to decompose τ in an isotropic and non-isotropic part

$$\tau_{ij} = \frac{1}{3}\tau_{kk}\delta_{ij} + (\tau_{ij} - \frac{1}{3}\tau_{kk}\delta_{ij}) = \frac{1}{3}\tau_{kk}\delta_{ij} + \tau'_{ij} \tag{4.20}$$

where τ'_{ij} is the non-isotropic part. The isotropic part can be combined with the pressure to form the modified pressure π_{GS}

$$\nabla\pi_{GS} = \nabla(p_{GS} + \frac{1}{3}\tau_{kk}) \tag{4.21}$$

For τ'_{ij} several models are known. In this study we make use of the following first-order model

$$\tau' = -\nu_t(\nabla\mathbf{u_{GS}} + (\nabla\mathbf{u_{GS}})^T) \tag{4.22}$$

where ν_t denotes the subgridscale eddy viscosity. To find an expression for ν_t we use the Smagorinsky model which relates the deformation of the GS velocity field to ν_t,

$$\nu_t = l^2{}_{mix}|(\nabla\mathbf{u_{GS}} + (\nabla\mathbf{u_{GS}})^T)| \tag{4.23}$$

l_{mix} Is the mixing length of the subgridscale motion. This length is given by

$$l_{mix} = C_s \cdot \Delta \tag{4.24}$$

C_s is called the Smagorinsky constant. Δ Is the characteristic grid distance defined as

$$\Delta = (\Delta x\Delta y\Delta z)^{1/3} \tag{4.25}$$

Now the mixing length l_{mix} is proportional to the filter length l_f. This way C_s can essentially be used to regulate the effective resolution of our LES. One obvious condition for C_s is that $l_f > \Delta$. In our simulations we use a value of $C_s = 0.085$, which has proven to give good results for a channel flow.

The value of the subgrid stress tensor has to large a value near the wall. To make sure this is corrected for, the mixing length is corrected for by the Van Driest damping function

$$l_{mix} = C_s\Delta(1 - exp(-\frac{z^+}{A^+}))^2 \tag{4.26}$$

where A^+ is a constant, given a value of 26 in this study. The z^+ denotes the distance to the wall in wall units, i.e. $z^+ = Z\frac{u_*}{\nu}$.

4.3 Boundary conditions

A no slip condition is applied along the rigid walls, i.e. both the upper and lower wall as well as the fence. Throughout our simulations, a non-equidistant grid is used for the z-direction, resulting in grid refinement near the upper and lower wall. As a result the viscous sublayer near both walls is resolved in our simulations. It is assumed that the instantaneous velocity distribution vertical to these walls follows the linear law-of-the-wall, $u_+ = z_+$, for $z_+ \leq 5$. In the spanwise direction we employ periodic boundary conditions. For simulations of channels without a fence, periodic boundary conditions are also applied for the streamwise direction.

4.3.1 Force method

In order to simulate an infinitely thin fence we use boundary body forces as proposed by Fadlun a.o. [11]. They introduce a body-force field $\mathbf{f}$ such that a desired velocity distribution $\mathbf{V}$ can be assigned over a boundary $\mathbf{S}$. This amounts to adding to the NS equations the body-force $\mathbf{f}$

$$\frac{D\mathbf{u}}{Dt} = -\nabla p + \frac{1}{Re_*}\nabla^2\mathbf{u} + \mathbf{f} \tag{4.27}$$

Equation 4.5 doesn't change. An expression for $\mathbf{f}$, which is a function of time since the force is dependent on the fluid velocity, can be derived by first discretizing the equation above

$$\frac{\mathbf{u}^* - \mathbf{u}^l}{\Delta t} = RHS^{l+1/2} + \mathbf{f} - \nabla p \tag{4.28}$$

where $RHS^{l+1/2}$ contains the convective and viscous terms. Next the $\mathbf{u}^*$ is given the value zero for the positions on the fence. After this step the pressure-correction step, formula 4.12, is performed.

4.3.2 Wengle's law-of-the-wall

For the x-direction we have confined ourselves to using an equidistant grid. This could make it impossible to refine the grid near the fence to within the viscous sublayer without increasing the computation time of the simulation to an unreasonable amount. So for the fence it is not enough to only apply the linear law-of-the-wall. Now for $z_+ > 11.81$ we assume a power-law description $u_+ = A(z_+)^B$ with $A = 8.3$ and $B = 1/7$. Then according to Werner and Wengle [2] the velocity components tangential to a wall, at the grid point next to the wall, can be related to the corresponding wall-shear stress components as follows

$$|\tau| = \frac{2\mu|\mathbf{u_{tan}}|}{\Delta x} \quad \text{for} \quad |\mathbf{u_{tan}}| \leq \frac{\mu}{2\rho\Delta x}A^{\frac{2}{1-B}} \tag{4.29}$$

$$|\tau| = \rho\left[\frac{1-B}{2}A^{\frac{1+B}{1-B}}\left(\frac{\mu}{\rho\Delta x}\right)^{1+B} + \frac{1+B}{A}\left(\frac{\mu}{\rho\Delta x}\right)^{B}|\mathbf{u_{tan}}|\right]^{\frac{2}{1+B}} \quad \text{for} \quad |\mathbf{u_{tan}}| > \frac{\mu}{2\rho\Delta x}A^{\frac{2}{1-B}} \tag{4.30}$$

where Δx is the horizontal width of the grid cell next to the fence and $\mathbf{u_{tan}}$ the velocity vector tangential to the wall. Throughout this study we will refer to this method as Wengle's law-of-the-wall.

4.4 RANS Turbulence Models

When we use Reynolds Averaged Navier Stokes (RANS) equations, the computational effort involved is greatly reduced. These RANS equations represent transport equations for the averaged flow quantities only, with all the scales of the turbulence being modelled. They do present one with a closure problem, specificially the need for a turbulence model to determine the Reynolds stress tensor. In this study we will make use of two turbulence models as provided by the commercial CFD package FLUENT, namely the $k-\epsilon$ model and the Reynolds stress model.

4.4.1 $k-\epsilon$ model

The $k-\epsilon$ model employs the Boussinesq hypothesis to relate the Reynolds stresses to the mean velocity gradients

$$-\rho\overline{u_i'u_j'} = \mu_t\left(\frac{\partial\overline{u_i}}{\partial x_j}+\frac{\partial\overline{u_j}}{\partial x_i}\right)-\frac{2}{3}(\rho k)\delta_{ij} \tag{4.31}$$

where μ_t is the eddy viscosity or turbulent viscosity. In the $k-\epsilon$ model μ_t is a function of the turbulent kinetic energy k and the viscous dissipation rate ϵ

$$\mu_t = \rho c_\mu \frac{k^2}{\epsilon} \tag{4.32}$$

where c_μ represents an emperical turbulence constant with value $c_\mu = 0.09$. The disadvantage of the Boussinesq hypothesis as presented is that it assumes μ_t is an isotropic scalar quantity. This makes it a poor model when applied to situations in which the anisotropy of turbulence has a dominant effect on the mean flow. Both k and ϵ are obtained from their transport equations and form the two equation $k-\epsilon$ model

$$\frac{Dk}{Dt} = P + \frac{\partial}{\partial x_j}\left(\frac{\mu_t}{\sigma_k\rho}\frac{\partial k}{\partial x_j}\right)-\epsilon \tag{4.33}$$

$$\frac{D\epsilon}{Dt} = \frac{\partial}{\partial x_j}\left(\frac{\mu_t}{\sigma_\epsilon\rho}\frac{\partial \epsilon}{\partial x_j}\right)+\frac{\epsilon}{k}(C_{1\epsilon}P - C_{2\epsilon}\epsilon) \tag{4.34}$$

where $C_{1\epsilon} = 1.44$ and $C_{2\epsilon} = 1.92$. Both $\sigma_k = 1.0$ and $\sigma_\epsilon = 1.3$ are the turbulent Prandtl numbers. P represents the production term

$$P = -\overline{u_i'u_j'}\frac{\partial\overline{u_i}}{\partial x_j} = \mu_t\left(\frac{\partial\overline{u_i}}{\partial x_j}+\frac{\partial\overline{u_j}}{\partial x_i}\right)\frac{\partial\overline{u_i}}{\partial x_j} \tag{4.35}$$

where the Reynolds stress is modelled using the Boussinesq hypothesis. The dissipation rate ϵ is large where production of k is large. I.e. the production and destruction terms are proportional to those of k.

4.4.2 Reynolds stress model

The Reynolds stress model is a second order closure model. It differs from the above described $k-\epsilon$ model in that it can account for the directional effects of the Reynolds stress field. The exact transport equation for the Reynolds stresses $\overline{u_i'u_j'}$ is

$$\frac{D\overline{u_i'u_j'}}{Dt} = \frac{\partial\overline{u_i'u_j'}}{\partial t} + \overline{u_k}\frac{\partial\overline{u_i'u_j'}}{\partial x_k} = P_{ij} + D_{T,ij} + D_{L,ij} + \Phi_{ij} - \epsilon_{ij} \tag{4.36}$$

where P_{ij} represents the stress production term, $D_{T,ij}$ the turbulent diffusion term, $D_{L,ij}$ the molecular diffusion term, Φ_{ij} the pressure strain term and ϵ_{ij} the dissipation term. The production term retains its exact form

$$P_{ij} = -\overline{u_i'u_k'}\frac{\partial\overline{u_j}}{\partial x_k} - \overline{u_j'u_k'}\frac{\partial\overline{u_i}}{\partial x_k} \tag{4.37}$$

and so does the molecular diffusion term

$$D_{L,ij} = \frac{\partial}{\partial x_k}\left(\nu\frac{\partial\overline{u_i'u_j'}}{\partial x_k}\right) \tag{4.38}$$

For the other terms we need closure approximations. The exact form for the turbulent diffusion terms $D_{T,ij}$ is

$$D_{T,ij} = -\frac{\partial}{\partial x_k}\left(\frac{1}{\rho_0}\overline{p'u'_j}\delta_{ik} + \frac{1}{\rho_0}\overline{p'u'_i}\delta_{jk} + \overline{u'_iu'_ju'_k}\right) \tag{4.39}$$

Here we use the following approximation for

$$\overline{u'_iu'_ju'_k} = -c_s\frac{e}{\epsilon}\overline{u'_ku'_m}\frac{\partial\overline{u'_iu'_j}}{\partial x_m} \tag{4.40}$$

where c_s is a constant The dissipation rate ϵ_{ij} is modelled assuming isotropy of the small dissipative eddies

$$\epsilon_{ij} = \frac{2}{3}\epsilon\delta_{ij} \tag{4.41}$$

The pressure strain term is the most important one to model accurately. Its effect on the Reynolds stresses is caused by two distinct physical processes: pressure fluctuations due to two eddies interacting with each other and pressure fluctuations due to the interaction of an eddy with a region of different velocity. It is modelled as

$$\Phi_{ij} = -C_1\frac{\epsilon}{k}(\overline{u'_iu'_j} - \frac{2}{3}k\delta_{ij}) - C_2(P_{ij} - \frac{2}{3}P\delta_{ij}) + {\Phi_{ij}}^w \tag{4.42}$$

with $C_1 = 1.8$ and $C_2 = 0.6$. ${\Phi_{ij}}^w$ is called the wall reflection term and accounts for the effects of a wall on the turbulence. It suppresses the fluctuating components normal to the wall and increases the streamwise components. The turbulent kinetic energy k can be found by adding the three normal stresses

$$k = \frac{1}{2}(\overline{{u'_1}^2} + \overline{{u'_2}^2} + \overline{{u'_3}^2}) \tag{4.43}$$

Summarized this means that six equations for the Reynolds stress transport are solved plus a model equation for the scalar dissipation rate ϵ in order to solve equation 4.41. Since the Reynolds stresses are solved directly, the model can capture anisotrpic turbulence when it occurs.

4.4.3 Near-wall approach

Both the models discussed above are primarily valid for turbulent flow in regions far from the walls and hence need adjustments for wall-bounded flows. FLUENT has two approaches for modelling the near-wall region. In the first approach, default in FLUENT, the viscous sublayer and buffer layer are not resolved. Instead standard wall-functions are used for this region. When $y_+ < 11.225$ the function is

$$\tag{4.44}$$

For $y_+ > 11.225$ the function is

$$u_+ = \frac{1}{\kappa}ln(Ey_+) \tag{4.45}$$

where E is an empirical constant with value $E = 9.81$. In most high Reynolds number flows this wall-function approach is used. For low Reynolds number situations, FLUENT provides a second approach, termed the near-wall modelling approach. The approach consists of a combination of resolving the whole viscosity affected region by means of a two-layer model, in case of a fine enough mesh, and using enhanced wall functions, in case of a coarser mesh.

In the two-layer approach the whole domain is subdivided into a viscosity affected region and a fully turbulent region. The demarcation of the two regions is determined by

$$Re_y = \frac{y\sqrt{k}}{\nu} \tag{4.46}$$

where y is the normal distance to the nearest wall. In the fully turbulent region, $Re_y > 200$, the turbulence models described above are employed to determine μ_t. In the viscosity affected near-wall region, $Re_y < 200$, another turbulent viscosity is computed from

$$\mu_{t,2layer} = \rho c_\mu l_\mu\sqrt{k} \tag{4.47}$$

where l_μ is

$$l_\mu = y c_{l,1}(1 - e^{\frac{-Re_y}{c_{l,2}}}) \tag{4.48}$$

with $c_{l,1}$ and $c_{l,2}$ constants. The two-layer definition then smoothly blends both viscosities using

$$\mu_{t,enh} = \lambda_a \mu_t + (1 - \lambda_a)\mu_{t,2layer} \tag{4.49}$$

where λ_a is a blending function with a value equal to unity far from the walls and zero very near to the walls

$$\lambda_a = \frac{1}{2}\left[1 + tanh\left(\frac{Re_y - 200}{A_\lambda}\right)\right] \tag{4.50}$$

The ϵ field for $Re_y < 200$ is computed from

$$\epsilon = \frac{k^{3/2}}{l_\epsilon} \tag{4.51}$$

where l_ϵ is

$$l_\epsilon = y c_{l,1}(1 - e^{\frac{-Re_y}{c_{l,2}}}) \tag{4.52}$$

FLUENT formulates the law-of-the-wall as a single law for the entire region, by blending the laminar and logarithmic laws-of-the-wall

$$u_+ = e^\Gamma u_{+,lam} + e^{1/\Gamma} u_{+,turb} \tag{4.53}$$

with Γ the following blending function

$$\Gamma = -\frac{a(y_+)^4}{1 + by_+} \tag{4.54}$$

with a and b two constants. $u_{+,lam}$ And $u_{+,turb}$ refer respectively to equation 4.44 and equation 4.45. Substituting these wall functions in equation 4.53 results in an overall law-of-the-wall.

4.5 Particle Motion

In this study we presume 'one-way coupling' for the dispersed flow. This means that particle motion is influenced by the fluid, but fluid motion is not influenced by the particles. The justification of this classification of the multiphase flow is dependent on the volume fraction of the particles which must be less than approximately 10^{-6}. In this study this is the case.

4.5.1 Equation of motion

In order to calculate the trajectory of a particle as it moves through the flow field the force $\mathbf{F}$ acting on the particle must be obtained. This is done analytically by integrating the stress tensor τ over the surface of the particle

$$\mathbf{F} = -\int\int \tau \cdot \mathbf{n}\, dS_{particle} \tag{4.55}$$

where $S_{particle}$ is the surface of the particle and $\mathbf{n}$ is a unit vector normal to the surface. Although it is a theoretically correct way to determine the particle trajectory, it would require far too much computational resources when simulating large ensembles of particles, as is done in this study. Therefore a model is needed to describe the forces acting on the particle as a function of the ambient flow conditions. One such a model for the acting force is based on the unsteady Stokes equation for a small rigid sphere in a nonuniform flow. Because it is based on the Stokes equations, the following restriction on the magnitude of the particle Reynolds number Re_p applies

$$Re_p = \frac{2a \mid \mathbf{u} - \mathbf{u_p} \mid}{\nu} < 1 \tag{4.56}$$

where a is the particle radius, $\mathbf{u_p}$ is the particle velocity and $\mathbf{u}$ the fluid velocity. Also the particle size is restricted to be much smaller than the smallest flow scale, so that the effect of the flow field on the particle can be treated as a point force. For a turbulent flow this means

$$\frac{a}{\eta} < 1 \tag{4.57}$$

where η is the Kolmogorov length scale. When both of these conditions are met, the force acting on the particle is given by the following equation, often referred to as the Basset- Boussinesq-Oseen (BBO) equation

$$\begin{aligned}
\mathbf{F} &= 6\pi\mu a(\mathbf{u} - \mathbf{u_p}) + m_p\mathbf{g} + && (4.58)\\
\frac{1}{2}m_f\frac{d}{dt}(\mathbf{u} - \mathbf{u_p}) &+ 6a^2\sqrt{\pi\rho\mu}\int_0^t \frac{\frac{d}{d\tau}(\mathbf{u} - \mathbf{u_p})}{\sqrt{t-\tau}}\, d\tau + && (4.59)\\
&\left(m_f\frac{D\mathbf{u}}{Dt} - m_f\mathbf{g}\right) && (4.60)
\end{aligned}$$

where μ is the dynamic viscosity, ρ is the density of the fluid, m_f is the mass of the fluid displaced by the particle and m_p is the mass of the particle. The so called Faxen terms are excluded from the equation, where they would have appeared in the first, third and fourth term. These Faxen terms give the correction to the relative velocity which results due to nonuniformity of the flow field. The magnitude of this correction is in the order of a^2/η^2, which according to restriction 4.57 may be neglected. The different components of equation 4.58 represent the following forces:

- The first term on the right-hand side of the equation represents the drag force which is due to steady-state viscous drag. For spherical particles the steady drag force is given by

$$\mathbf{F}_D = \frac{1}{2}\rho C_D A \mid \mathbf{U} - \mathbf{U_p} \mid (\mathbf{U} - \mathbf{U_p}) \tag{4.61}$$

  where C_D is the drag coefficient, A the particle radius and $\mathbf{U_p}$ the particle velocity. For the drag coefficient several relations are known. The drag coefficient for small particle Reynolds numbers is given by the Stokes drag

$$C_D = \frac{24}{Re_p} \tag{4.62}$$

The Stokes drag is derived for values of Re_p fulfilling equation 4.56. Substituting this drag coefficient in 4.61 yields the first component in the BBO equation. In the simulations a simple empirical relation of Brown and Hutchinson is used

$$C_D = \frac{24}{Re_p} + 0.44 \tag{4.63}$$

This coefficient is also valid for larger particle Reynolds numbers.

- The second term gives the effect of gravity on a particle. For a horizontal channel, like in this study, only the vertical particle motion will be influenced.
- The third term represents the added mass term which is due to non-viscous unsteady drag. This force is needed to accelerate the fluid surrounding and moving with the particle. It can be interpreted as if the particle has an extra, so called added mass. This added mass is equal to one half of the mass of the fluid being displaced. The actual mass of the particle plus the added mass is called the virtual mass. For particles with a density much larger than the fluid the contribution to the overall force will be small and in this case negligible.
- The fourth term is the Basset force due to viscous unsteady drag. It appears as a memory integral over the relative acceleration of the particle to that of the fluid. In the case of a heavy particle the instantaneous fluid acceleration and the particle acceleration become decorrelated. As a result the contribution is negligible for the case of heavy particles.
- The last term equals the pressure gradient force. It is a result of pressure differences occuring in the ambient flow. Again for heavy particles this term is negligible relative to the total force, due to the appearance of m_f in 4.60.

From above it is clear that when a third restriction is made

$$\rho_p \gg \rho \tag{4.64}$$

the first and second term of equation 4.58 will become the leading terms. Throughout this study we will work with a ratio of $\frac{\rho_p}{\rho} = 2000$. This simplifies the equation into the following form

$$\mathbf{F} = \frac{m_p}{\tau_p}(\mathbf{u} - \mathbf{u_p}) + m_p\mathbf{g} \tag{4.65}$$

where τ_p is the particle response time. It is defined as

$$\tau_p = \frac{2}{9}\frac{\rho_p a^2}{\rho\nu} \tag{4.66}$$

The particle response time can be interpreted as the time scale needed by the particle to respond to changes in the ambient flow conditions.

A force that is missing from 4.58 and hence from 4.65 is the lift force. The effect that the lift force may have on a particle as compared to the Stokes drag is proportional to a/η so that for small particles the effect of the lift force will be small.

4.5.2 Numerical method

The particle motion is given by the following equations

$$\frac{d\mathbf{u_p}}{dt} = \mathbf{a_p} \tag{4.67}$$

$$\frac{d\mathbf{x_p}}{dt} = \mathbf{u_p} \tag{4.68}$$

where the particle acceleration $\mathbf{a_p}$ is determined by the different contributions to the force on a particle. These equations are solved numerically using an Adams-Bashfort scheme

$$\mathbf{u_p}^{n+1} = \mathbf{u_p}^n + (\frac{3}{2}\mathbf{a_p}^n - \frac{1}{2}\mathbf{a_p}^{n-1})\Delta t \tag{4.69}$$

$$\mathbf{x_p}^{n+1} = \mathbf{x_p}^{n} + (\frac{3}{2}\mathbf{u_p}^{n} - \frac{1}{2}\mathbf{u_p}^{n-1})\Delta t \tag{4.70}$$

The time step used to solve the particle motion must be less than one tenth the particle response time in order to keep the scheme stable. In most cases, like in this study, the time step used to solve the fluid motion is small enough to act as the time step used to solve the particle motion.

The fluid velocity at the particle position is needed to solve the equations of motion. Because the fluid velocity is only known at the grid points, a second order interpolation routine is used to interpolate the fluid velocity.

4.5.3 Boundary conditions

Throughout this study for all simulations involving particles, the specific boundary conditions for these particles will be explicitly stated. However we can already make some general remarks concerning these conditions.

For the walls in the geometry, that is the lower and upper wall and the fence, we make use of two different boundary conditions. Either a particle will undergo an elastic collision or an inelastic collision at the wall. For the elastic collision routine this means that when a particle approaches the wall to within its particle radius, it is repositioned at a position from the wall greater than its radius with its vertical velocity component reversed. For the fence (back and front) this applies to the x-position and the horizontal velocity component. In the event of an inelastic collision the particle gets a new position at exactly one radius from the wall and a vertical velocity component with value zero. (Again x-position and horizontal velocity component for the fence.) Again, which of the above routines is used is stated for every simulation.

For the motion of the particles in the spanwise direction a periodic boundary condition is used. This means as much as when a particle leaves the domain in the spanwise direction it is reintroduced at the opposite surface at the same position and with the same velocity.

The boundary condition in the streamwise direction differs per simulation and will be defined per simulation.

Chapter 5

Results

5.1 Verification of the code

5.1.1 Channel flow

Here we perform a LES to verify if the code we use results in a correct channel flow with no fence. We use a Reynolds number based on values of the bulk velocity and the channel height which are in the order of the ones found in the everyday practice of catalyst reactors. Using a bulk velocity of $U_0 = 1,28m/s$ and a channel height of $H = 20cm$, a Reynolds number based on the channel height of $Re_H = 17067$ is found. This value corresponds to a Reynolds number based on the shear velocity of $Re_* = 1000$. The resolution we use is $48 \times 32 \times 80$ for a channel domain with size $3H \times 2H \times 1H$. The grid spacing in the streamwise and spanwise direction is equidistant. For the z-direction we use grid refinement near both the upper and lower wall, with the smallest grid cells having a height of $\Delta z = 0.0041H$ near the walls. The total simulation time is about $20t^*$, where the time scale is based on the shear velocity and H. The statistics are averaged over the last $10t^*$, where about every $0.1t$ a data field is stored.
In figure 5.1 the mean streamwise velocity profile is given.

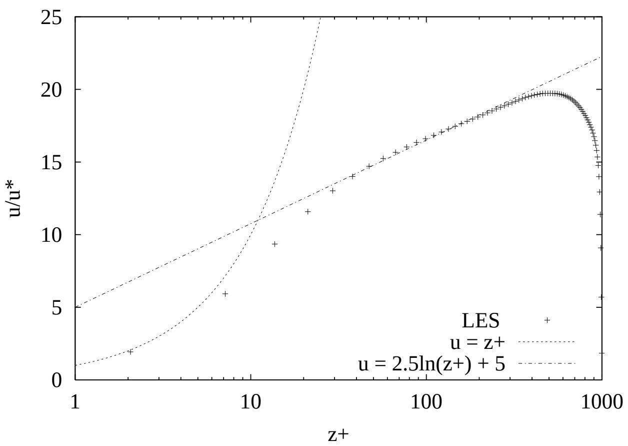

Figure 5.1: *Average streamwise velocity as a function of the distance to the wall.*

For comparison the theoretical curves are also plotted for the viscous sublayer ($z^+ < 5$) and the logarithmic layer ($z^+ > 30$). The LES results are in good agreement with these curves for the region where they apply.

In figure 5.2 the rms-velocities are shown. The LES results compare well to the numerical data of Moin and Kim [12], although they found smaller peaks for the streamwise direction due to a smaller Reynolds number.

The stress profiles are plotted in figure 5.3 and show the expected linear profile. This indicates

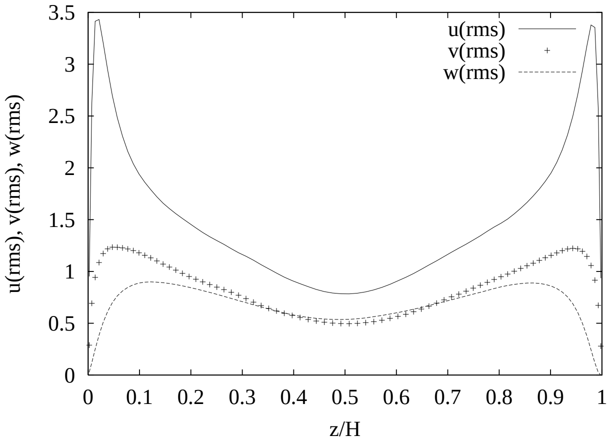

Figure 5.2: *RMS-velocities as a function of the distance to the wall.*

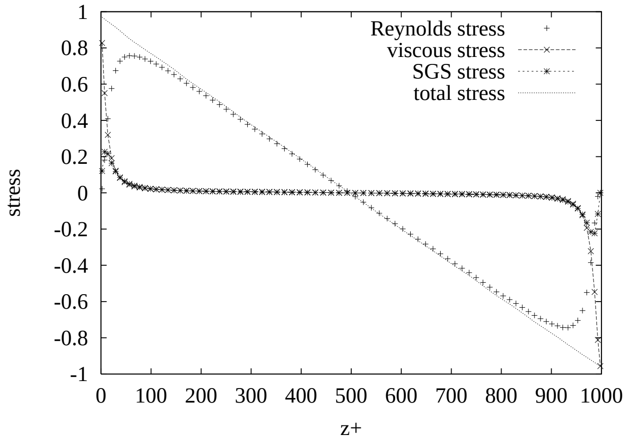

Figure 5.3: *Stress as a function of the distance to the wall.*

the flow is fully developed. From all these results it can be concluded that our code is capable of simulating a realistic channel flow.

5.1.2 Particle routine

In the same simulation particles are introduced at random positions throughout the channel. As soon as a particle leaves the channel in the streamwise or spanwise direction it is reintroduced at the opposite surface at the same position and with the same velocity and acceleration as it left the channel. On both the upper and lower wall elastic collissions take place, as described in section 4.5.3. Three different kind of particles are used with different relaxation times, specificially $\tau_p = 0.0125$, $\tau_p = 0.625$ and $\tau_p = 5$. For each kind 50000 particles are introduced. The density ratio we use is $\frac{\rho_p}{\rho} = 800$ and there is no gravity involved. They are introduced after the flow has already had $10t^*$ to establish itself. Of the following $10t^*$ only the last $5t^*$ are used to store data fields, about every $0.1t^*$. So over these last $5t^*$ the statistics are averaged.
In figure 5.4 the particle concentration, normalised by the theoretical uniform concentration, as a function of the vertical height is shown. Only the upper half of the channel is plotted, so the three lines are more clearly distinctive near the wall. They show a typical behaviour also observed by Mols [13]. The smallest particles, $\tau_p = 0.0125$, will accumulate in the near wall region. The larger the particles the further away from the wall they will start to accumulate, with a smaller peak near the wall. Particles with $\tau_p = 5$ have a concentration of zero near the wall, which is due to the elastic collision routine. To be more precise, these particular particles are the largest and

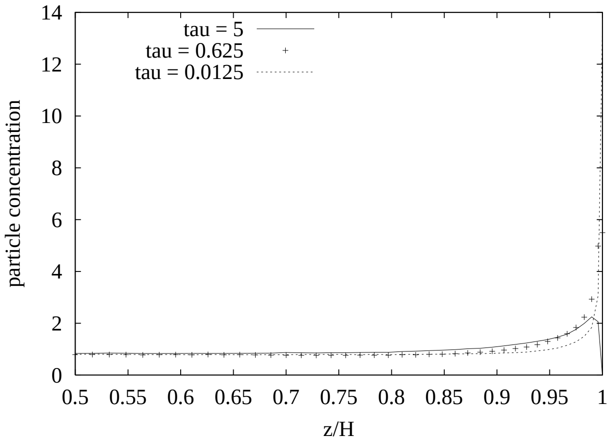

Figure 5.4: *Normalised particle concentration as a function of the height.*

have a radius in the order of the height of the smallest gridcell. The other two kind of particles have much smaller sizes.

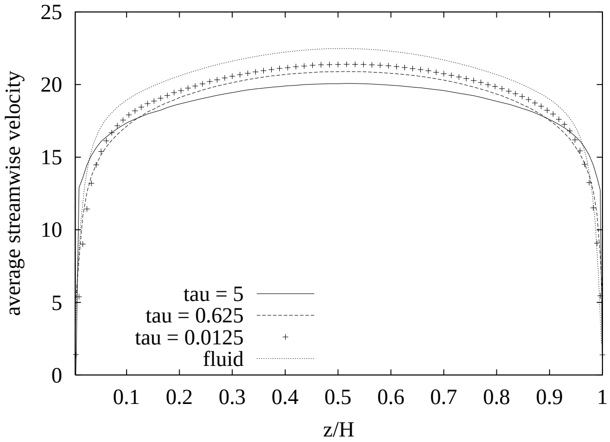

Figure 5.5: *Average streamwise velocity as a function of the channel height for the particles and the fluid.*

In figure 5.5 the averaged streamwise velocities of the particles and the fluid are shown. With increasing particle relaxation time, the particle velocity in the central part lags more and more behind that of the fluid. Whereas in the wall area the opposite behaviour is observed. This is in agreement with the findings of Mols [13]. The higher the particle inertia, the more a particle will keep its streamwise momentum when being transferred in the direction of the wall, hence the difference in fluid and particle velocity. A quantative comparison to the results of Mols has not been made since he uses a smaller Reynolds number of $Re_* = 800$. All the other parameters used are equal to those of Mols. From these results we can conclude that the particle routine in our simulations produces realistic results.

5.2 Observations fence flow

5.2.1 Fence in channel

In this section we perform a test LES of a channel with a fence. We like to find out if the grid we use is fine enough and if there are any subjects we need to give some extra attention. We use the same Reynolds number as in the previous section, i.e. $Re_* = 1000$. The fence is going to disturb the channel flow over an unknown distance. This makes it necessary to find an alternative for the periodic boundary condition previously used in the streamwise direction. It is for this reason that a second periodic channel flow without a fence is simulated simultaneously. An instantaneous velocity field of this channel at a certain x-position, will be the inlet field of the channel with the fence. The channel without the fence has a size of $4H \times 2H \times 1H$ with a grid resolution of $36 \times 60 \times 80$. For the channel with the fence the size of the domain is $10H \times 2H \times 1H$ with a grid resolution of $90 \times 60 \times 80$. For the z-direction a non-equidistant grid is applied, consisting of grid refinement at the upper and lower wall. Both channels use this same grid in the z-direction for obvious reasons. The fence is placed at a distance of $1.9H$ from the inlet of the channel and has a height of $0,26H$. We use Wengle's law-of-the-wall, as discussed in section 4.3.2, on the fence. When the flow has established itself, i.e. the extra (fenceless) channel has become turbulent and the flow at the inlet has had enough time to travel at least once through the channel with the fence, a data field is stored every $0.1t^*$, for about $13t^*$.

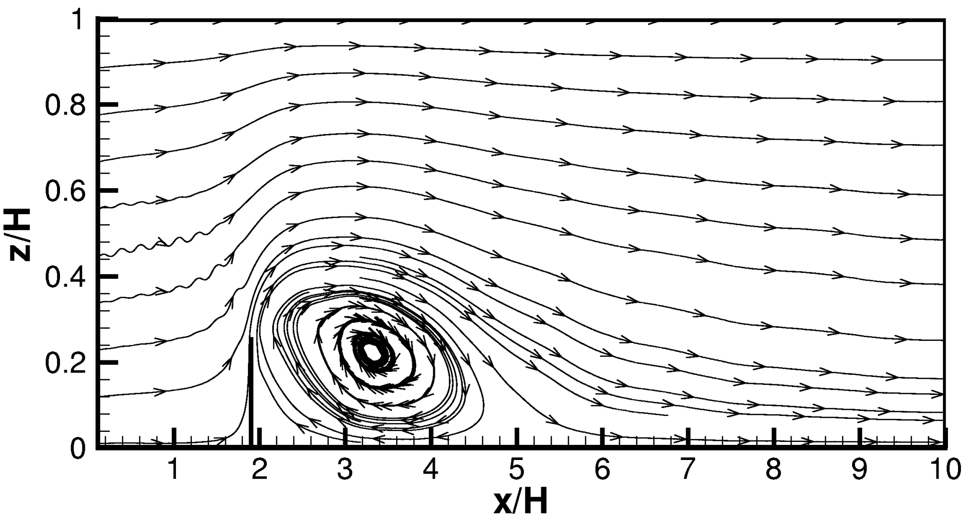

Figure 5.6: *xz-Cross-section of the channel with fence showing the time-averaged streamlines.*

In figure 5.6 the time-averaged streamlines are shown for a xz-cross-section of the channel. One clearly sees the existence of a large wake behind the fence. The averaged reattachment length is $x_R = 3H = 12h$. It has a maximum height of $z = 0,48H$ at x-position $x = 2,9H$, almost two times the fence height. This maximum height complies well with the findings of Durst and Rastogi [9], who also found a value of twice the fence height for various small blockage ratio's. Apparent are also wiggles in the streamlines in front of the fence. These wiggles are known as $2\Delta x$-waves and are a well known numerical phenomenon. They will be adressed later on.

In figure 5.12 the streamwise velocity as a function of the height of the channel is depicted for several x-positions. These velocities are averaged over the y-direction and over time. The profile at the inlet of the channel is shown in (a), and is the result of the extra channel without a fence. In (c) the profile at the x-position of the fence is shown, the u-velocity having a value zero on the fence. From (b) one can tell there is a recirculation zone just in front of the fence and from (d) it is clear there's an extra one, next to the large one, just behind the fence. This is indeed the general flow structure as expected for flow over obstacles and as found in the literature. Graph (f) gives the profile at the end of the channel. One can see that it still hasn't regained its initial shape, indicating how far the flow is disturbed in the streamwise direction. More disturbing and not as expected is the dent in the profiles at x-positions in front of and just around the fence, (b) to (d). Profiles of the w-velocities as a function of the height also show a dent at these x-positions. Whether this is a physical or a numerical phenomenon will be looked upon in the next few sections.

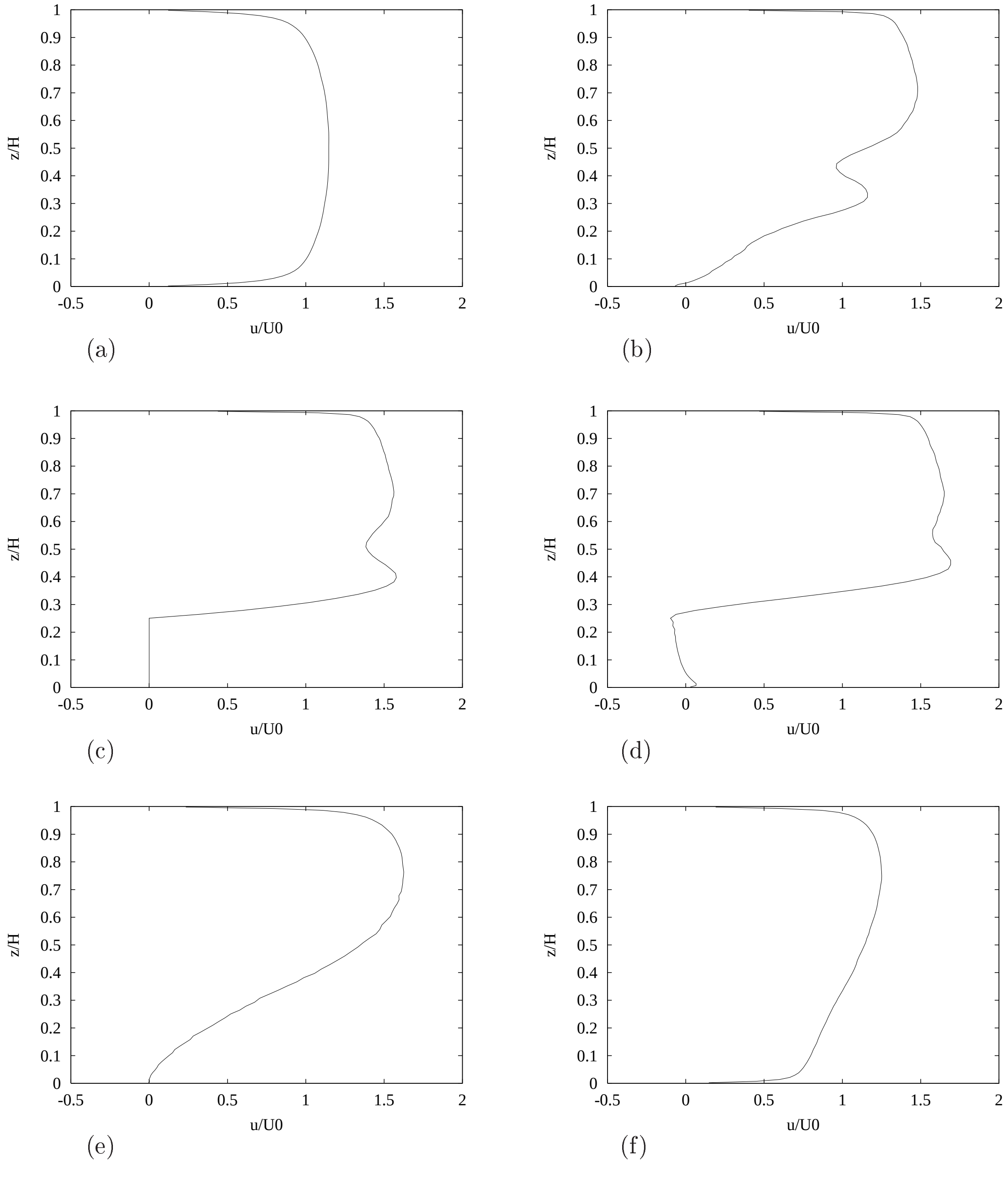

Figure 5.7: *The u-velocity u/U_0 as a function of the height z/H for the following x-positions: (a) $x/H = 0$ (b) $x/H = 1,8$ (c) $x/H = 1.9$ (d) $x/H = 2$ (e) $x/H = 5$ (f) $x/H = 10$*

In this same simulation 60000 particles are put randomly all over the channel. They all have the same particle response time $\tau_p = 0.01$. The density ratio is $\frac{\rho_p}{\rho} = 2000$ and this ratio will be used throughout this study. This response time corresponds to a dimensional radius of $a = 8,2\mu m$ when using the velocity scale and length scale discussed at the start of section 5.1. This is a value found for particles that clog the catalyst reactors discussed in the introduction. The boundary condition used on the walls and fence for the particle movement is an elastic collision routine.

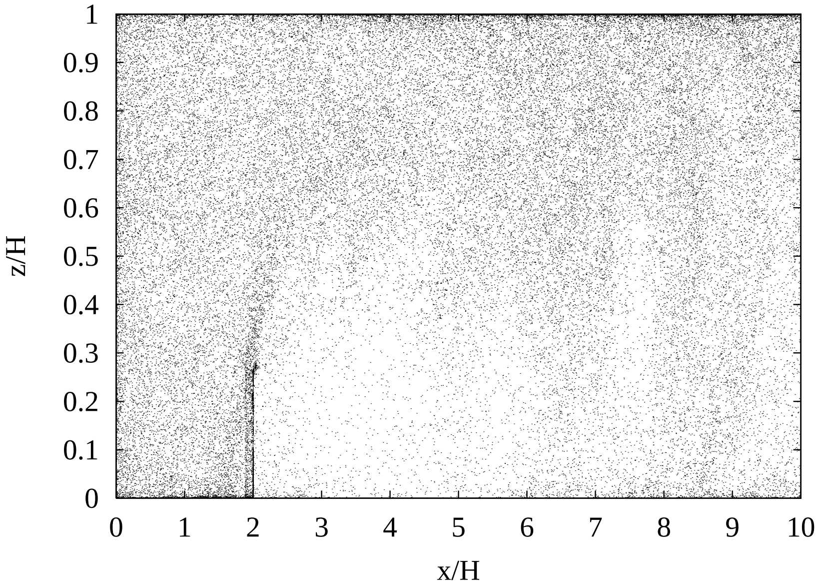

Figure 5.8: *xz-Projection of the channel with fence showing instantaneous positions of the particles at a certain time.*

Figure 5.8 shows an instantaneous plot of the particle positions in a xz-projection of the channel. At this time the flow in the channel has established itself and so have the particles. When (re-)introduced at the inlet of the channel, the distance to the fence is just long enough for the particles to have adapted themselves to the ambient flow. In the figure one can clearly see the majority of the particles being swept over the fence and over its wake, instead of being caught in it. Also one notices an accumulation just in front of the fence. This is due to the collision routine on the fence. Considering the fact that these particles are all exactly identical, the maximum distance at which they are repositioned after a collision with the fence is the same for all of them. Next they are instantly pushed back to the fence due to the flow direction of the fluid, keeping them within a certain distance of the fence. This creates the narrow strip of particles in front of the fence.
Now the question rises whether the wiggles and/or dent influence the particle trajectories downstream of the fence. Most likely the particles won't even notice the wiggles, due to their inertia. If this is the case we may conclude that the present geometry does produce the physically correct results concerning the particles. Whether or not we can make this conclusion will be adressed later on.

Since most of the particles are swept over the wake of the fence, we place a second higher fence somewhat further downstream. The idea, as explained in the introduction, is that most of the particles which are swept over the wake of the first fence will collide with the second fence. We perform a new simulation to study this idea of two fences in the channel. Again the Reynolds number is $Re_* = 1000$. The size of the domain is $15H \times 2H \times 1H$ with a grid resolution of $135 \times 50 \times 80$. The channel without a fence, which produces the inlet velocity field, remains the same. The total simulation time is about $10t$. The first fence is placed at $x = 1H$ with a height of $h = 0,14H$. The second fence is positioned at $x = 3H$ and with a height of $h = 0,5H$ is higher than the first one. The flow exhibits the same problems as for the simulation with one fence. I.e. from both fences wiggles originate and the velocity profiles at x-positions before the second fence have a dent (and two dents at x-positions before the first fence). See figure 5.9.

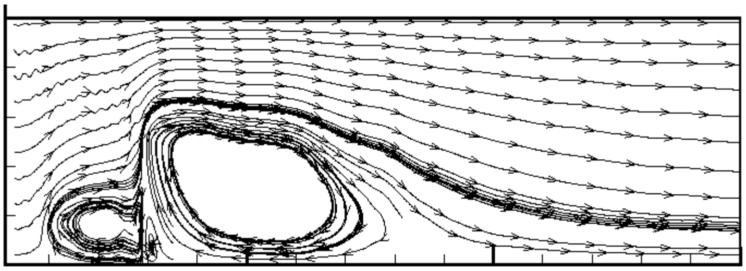

Figure 5.9: *xz-Cross-section of the channel with two fences showing the time-averaged streamlines.*

Again 60000 particles are introduced in the simulation with $\tau_p = 0.01$. We would like to see all the particles that are swept over the first fence collide with the second fence and get caught in the recirculation zone between the fences. The result is shown in the instantaneous plot of

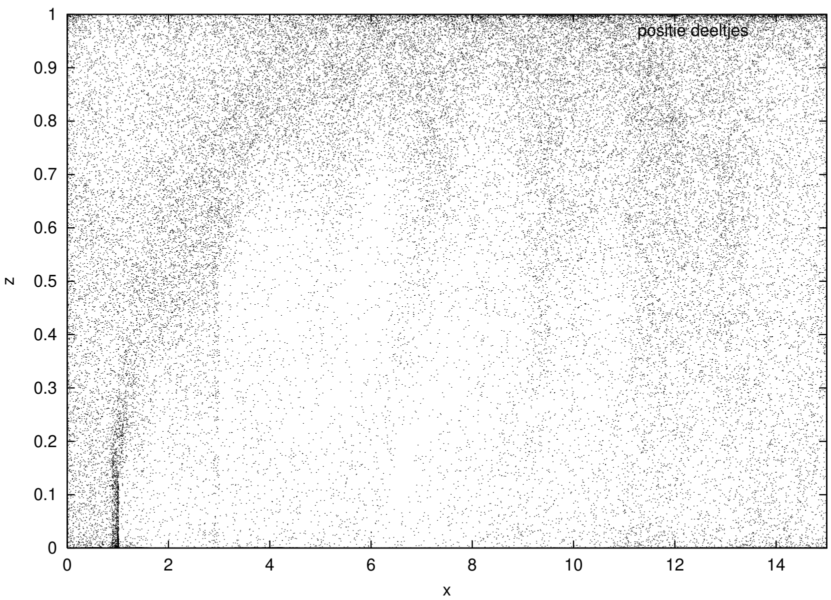

Figure 5.10: *xz-Projection of the channel with two fences showing instantaneous positions of the particles at a certain time.*

figure 5.10. It seems as if the shear layer in which the particle concentration is highest has gained a somewhat different curvature, compared to the one fence simulation. The shear layer seems to bend to the top of the second fence, where the particles again are swept over. Caution must be taken that wiggles and the profile dent are present in this simulation and this time at x-positions where the particle behaviour is of interest, notably between the fences.

All things considered the two test simulations present us with some problems. First there are the wiggles. Although studies have been published with wiggles present, for example Orellano and Wengle [2], we still want to see if they can at least be reduced. Second there is the dent in the velocity profile. Also it seems that our initial goal of trapping particles with one or two fences won't work. Here we make the assumption that the particle behaviour is not effected by the wiggles and/or dent. From the literature we found that there could be a possibility of using shedded vortices to trap the particles, as was discussed in the introduction and described in the patent [5]. Unfortunately clear shedding of vortices can not be detected in the two simulations described. That is no vortices are found when studying instantaneous contour plots or a animation of the velocity contours over time. In the following sections we will adress the shedding of vortices.

First however we concentrate on the wiggles and dent in the following subsections.

5.2.2 Wiggles

The wiggles observed are a result of the central differencing scheme used. Whether or not these wiggles are present is dependent on the size of the grid Peclet number. The nondimensional grid Peclet number Pe gives a measure of the relative strength of advection and diffusion

$$Pe = \frac{u\Delta x}{K} \tag{5.1}$$

where K is the diffusivity. The requirement for no wiggles to appear is $Pe < 2$. For $Pe > 2$ wiggles may appear. In the simulation without a fence the grid Peclet number is $Pe > 2$ for some positions and no wiggles exist. In this connection it must be said that it's usually the combination of a large Pe (> 2) with some singularity that gives rise to wiggles. In our geometry that singularity is the infinitely thin top of the fence and it is here that the wiggles originate. Calculating the time-averaged grid Peclet number for this simulation, gives values much larger than 2 around the top of the fence. This is shown in figure 5.12 (a) and (b) for both the x- and z-direction, i.e. Pe_x and Pe_z. For the y-direction, not shown in the figure, the value of Pe_y is smaller than 2. Now the wiggles can be removed by reducing the grid spacing for both directions. From graph (a) it is clear this means increasing the number by a factor 10 for the equidistant x-direction, but this results into a lot of extra computation time. In order to circumvent this option three other adjustments are suggested, specificially grid refinement in the z-direction at the top of the fence, softer boundary conditions at the top of the fence and lower Reynolds number. These adjustments are implemented in the simulation with one fence. The adjusted simulations are performed starting from a converged field of the original simulation. They have had $2t^*$ to settle and all the results shown are averaged over an extra $2t^*$.

- *Grid refinement in the z-direction.* The grid is now refined at the height of the top of the fence. This won't make the wiggles dissappear but could make them much smaller since the grid Peclet number for the z-direction becomes smaller.

  In figure 5.12 (c) it is shown that the refinement reduces the grid Peclet number enough for the z-direction. For the x-direction Pe is unchanged. When looking at the averaged streamlines the amplitude of the waves is still the same. Apparently and as expected the high grid Peclet number in the x-direction is much more important in inducing the wiggles.

- *Softer boundary conditions.* This adjustment consists of no longer imposing the value zero on the u-velocity at the top of the fence. It allows the value of the u-velocity to gradually change for a small range of grid cells near the top of the fence and on the fence . The highest grid cell of this range gets a u-velocity that is equal to the u-velocity of the grid cell above it. (This latter grid cell being the first grid cell above the top of the fence.) The grid cell immediately beneath the highest grid cell in the range, gets a u-velocity of 0.9 times the u-velocity of the highest grid cell. The second grid cell in the range beneath the highest grid cell, gets a u-velocity of 0.8 times the u-velocity of the highest grid cell. This goes on, until the lowest grid cell in the range on the fence gets a u-velocity of zero value.

  This adjustment however gives no change to the result. Also an extra adjustment besides the first one was done by doing the same for the w-velocity next to the u-velocity. This gives no result either, as can be seen in (d).

- *Lower Reynolds number.* Lowering the Reynolds number will increase the viscosity and thereby lower the amplitude of the waves. To check this the Reynolds number is decreased by a factor 3 from $Re_* = 1000$ to $Re_* = 333$. This last value translates into a value of $Re_H \approx 5000$ with a dimensional bulk velocity $U_0 = 0,36 m/s$. From (e) and (f) it is clear that the grid Peclet number becomes much smaller for all directions, though still not small enough for the x-direction. From the resulting streamline plot it can be seen that the waves have become indeed somewhat smaller, though slightly, but have not disappeared. Besides the effect the lower Reynolds number has on the wiggles, it can also be noted that the recirculation zone in front of the fence becomes slightly larger and the dent in the u-velocity profiles becomes somewhat smaller.

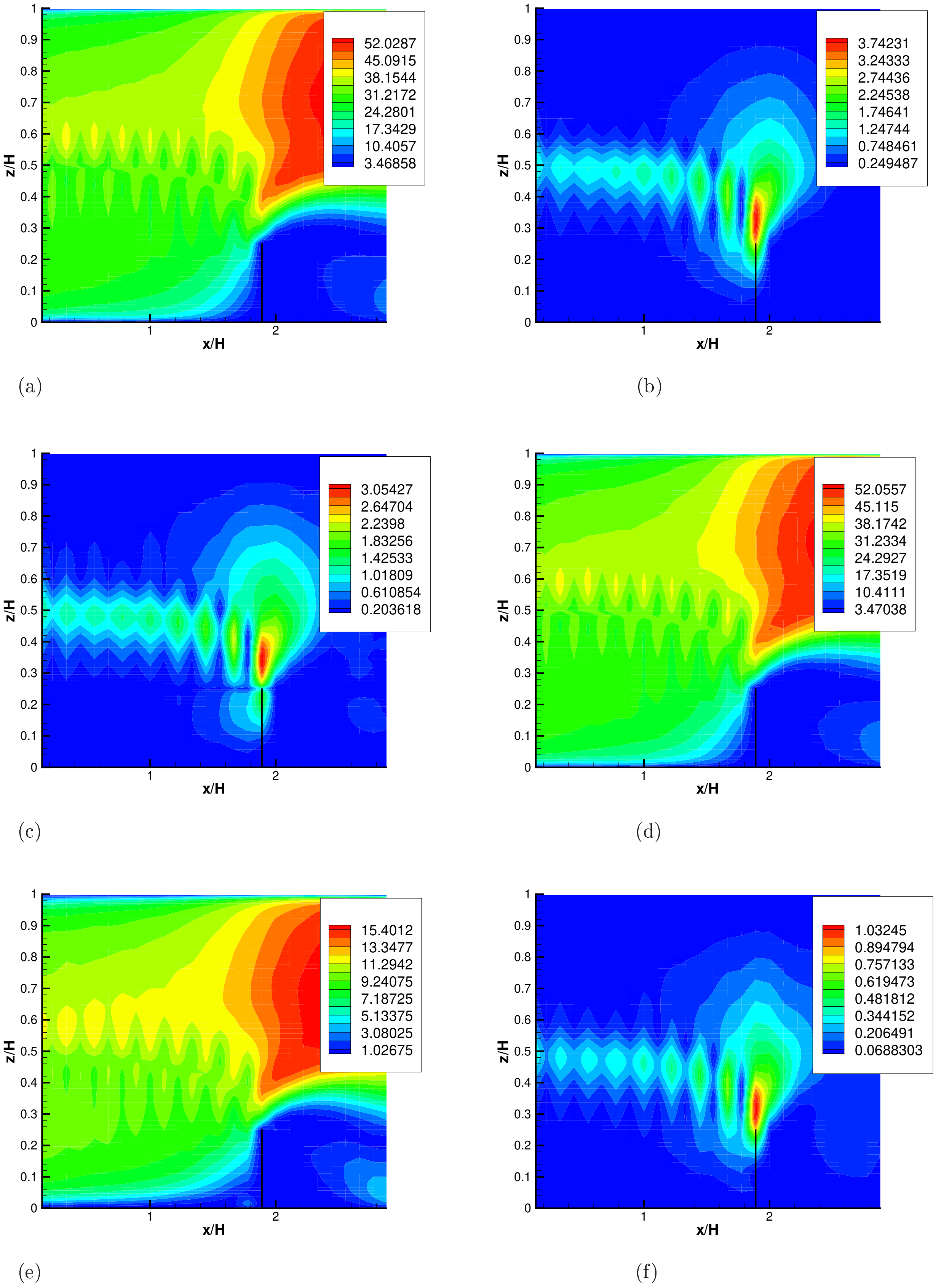

Figure 5.11: *Grid Peclet number for: (a) x-direction (b) z-direction (c) z-direction with grid refinement (d) x-direction with softer boundary condition (e) x-direction with* $Re_* = 333$ *(f) z-direction with* $Re_* = 333$.

From all of this we can conclude that to eliminate the wiggles we simply must increase the resolution around the fence, because we don't want to restrict ourselves to low Reynolds numbers. It must be noted that wiggles are a well known numerical phenomenon and present in various published results, for example Orellano and Wengle [2]. They claim that the effect on the statistics is limited to a narrow zone upstream of the obstacle and that the results outside of this zone and downstream are unaffected.

We now know what to do to remove the wiggles. Still two questions remain. First there is the dent in the velocity profile and we like to know whether or not the wiggles and the dent are related phenomena. In that case making the wiggles disappear could be enough to make the dent go away. This will be adressed in section 5.2.3. Second do the wiggles in any way influence the particle behaviour? This question will be briefly looked upon in section 5.3.2. First we concentrate on how to make the dent disappear.

5.2.3 Resolution tests

In this section we study what the effect is of using different resolutions on the wiggles and dent. As a starting point we use a 2-dimensional laminar simulation instead of using the LES of section 5.2. This saves computation time since we only need 1 grid cell for the y-direction. Furthermore we don't use any extra fenceless channel to provide an inlet profile and neither do we apply Wengle's law-of-the-wall on the fence. We now use a Reynolds number based on the fence height of $Re_h = 500$ and an inlet velocity of $U_0 = 1$. The blockage ratio has a value of $H = 4h$ and the fence is placed at $x/h = 2$ downstream of the inlet. The resolution used is $400 \times 1 \times 40$ for a channel of size $40h \times 1h \times 4h$.

Now when looking at the streamwise velocity as a function of the height for certain x-positions in the channel, some abnormalities are found. In figure 5.12 the u-velocity profiles are depicted for different x-positions in the channel. The profiles are a result of averaging over $20t$, where the time scale t is no longer based on the shear velocity and channel height but on the inlet velocity and fence height. (Note that there's a gap at the upper part of these profiles in the figure which is due to the very large grid cells used in the upper part of the channel.) In these graphs two abnormalities present themselves.
First of all there appears a dent in the profiles around $z = 1.5h$. It only exists at x-positions upstream of the fence ((a) to (c)) and decays very rapidly for positions downstream. In (d), determined at a distance of $0,1h$ behind the fence, the dent has as good as disappeared. This is kind of the same dent we encounter in the turbulent flow with one fence, section 5.2.1. It must be noted that the wiggles are also present in this simulation.
Second there's a small irregularity in the profile around $z = 0,5h$ which is clear from (b), i.e. the profile is not smooth. At several x-positions throughout the channel these irregularities appear although they are very small. It seems that a single point creates this irregularity, and thus it is probably ascribable to the low resolution in the z-direction. The w-velocity as function of the height also shows a dent and profile irregularities for the same x-positions. These graphs are not shown here.

Instantaneous profiles instead of averaged ones also systematically result in profiles like the ones shown in figure 5.12 for both velocity components. From this it can be concluded that the abnormalities are not a result of too few data used for averaging. Neither are they a result of a non-established flow. Because running a simulation for an extremely long time ($135t$), before collecting the necessary data, results in similar graphs. [1] Since we encounter the same problems in this section as when simulating a turbulent flow, section 5.2.1, the wiggles and dent are not likely to be a result of Wengle's law-of-the-wall, which we only used for the fence in the LES.

There's always the possibility that the dent could be a physical phenomenon. However in the literature this dent in the velocity profile is never mentioned. Furthermore running a similar simulation with a commercial package (FLUENT 6) neither results in velocity profiles with dents.

[1] In the literature it is found that for laminar fence flow an extra recirculation zone is found on the upper channel wall. Both Peng, Hwang [3] as Tropea, Gackstatter [4] found this eddy. However after $135t$, equal to the time of Peng, Hwang's simulations, this recirculation zone doesn't exist in our simulation. This complies well with Tropea's findings that this extra recirculation zone only appears for blockage ratio's of $h/H = 0.5$, $h/H = 0.75$ and not for $h/H = 0.25$, the ratio used here.

It thus seems very likely that the dent is not a physical phenomenon. The experiment described in the next section will confirm this conclusion.

Then there is the possibility that the dent is connected with a lack of resolution, just like the wiggles discussed in section 5.2.2, which are present when using this particular x-resolution. One indication for this is that the dent exists roughly at the same z-positions as the wiggles exist. Furthermore when studying the dent as it develops in time, one can see the dent originate just above the fence at the beginning of the simulation and slowly appear for x-positions further upstream of the fence, until it eventually appears in the profile near the inlet of the channel. This process is similar to that of the wiggles. However the wiggles do not appear above the fence for the x-position of the fence or for x-positions downstream of the fence, as does the dent.

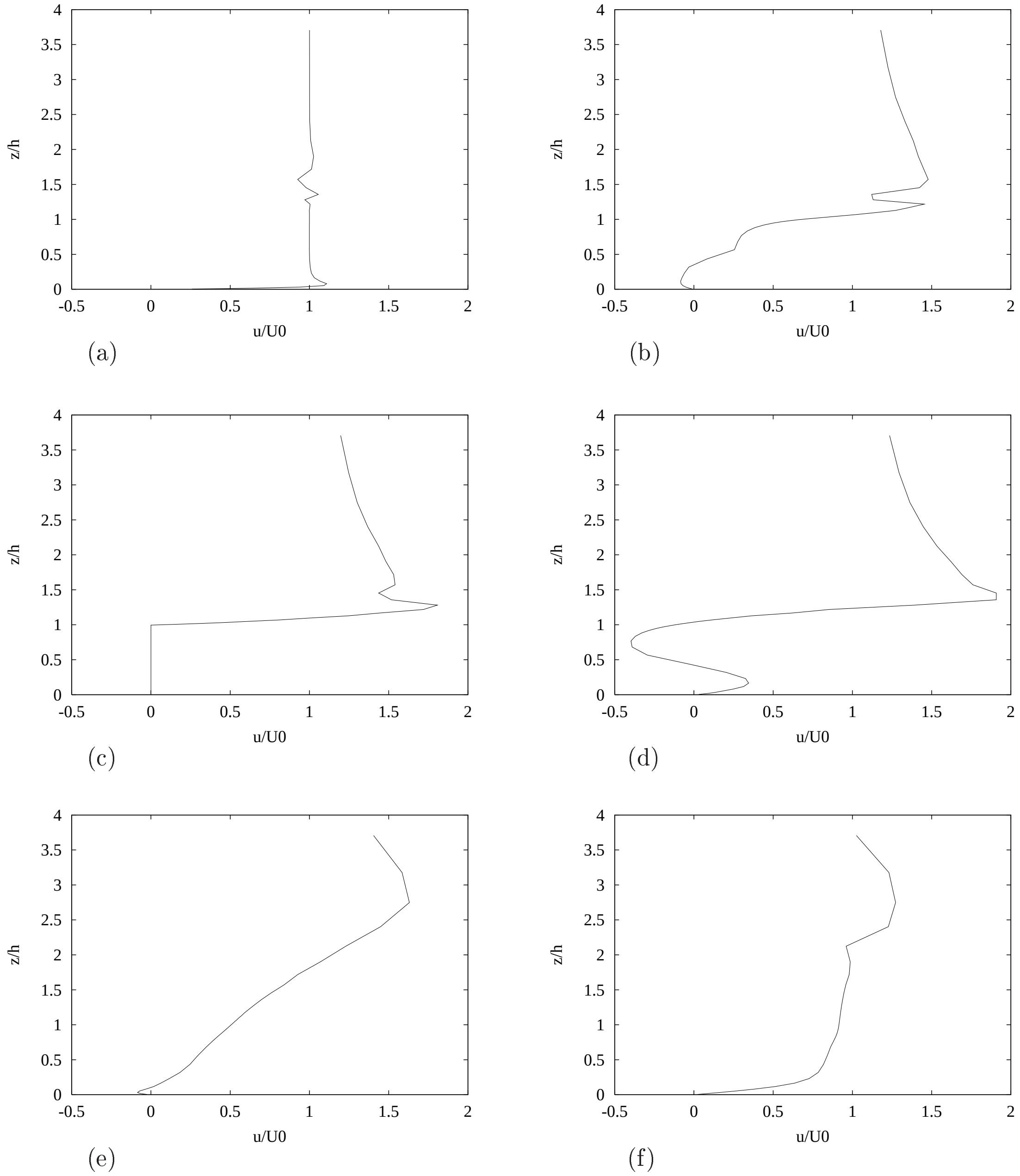

Figure 5.12: *The u-velocity u/U_0 as a function of the height z/h for the following x-positions: (a) $x/h = 0,1$ (b) $x/h = 1,8$ (c) $x/h = 2$ (d) $x/h = 2,1$ (e) $x/h = 7,1$ (f) $x/h = 40$*

	Resolution	Dent	Profile irregularity
I	$400 \times 1 \times 40$	one dent	present
II	$400 \times 4 \times 40$	one dent	present
III	$400 \times 4 \times 160$	multiple dents	none
IV	$800 \times 4 \times 80$	smaller dent	small irregularity
V	$1600 \times 4 \times 40$	almost gone	present
VI	$2400 \times 4 \times 40$	none	large irregularity
VII	$2400 \times 4 \times 80$	none	none
VIII	$1800 \times 20 \times 80$	none	none

Table 5.1: Observations made for different resolutions concerning the profiles of the u- and w-velocity as function of the height of the channel.

Increasing the resolution will make the wiggles disappear. It is interesting to see whether it will do the same for the dent in the profile. In order to determine the influence of the resolution on the two abnormalities in the flow, several simulations are done with different grids. All the other parameters remain equal to the ones given in the beginning of this section. The results are shown in table 4.1.

The velocities used in the graphs from which the observations, noted in the table, are made, are all averaged over at least $10t$ and the y-direction. All the simulations make use of 4 grid cells in the y-direction instead of 1. This difference in grid cells in the y-direction has no impact on the abnormalities, which is concluded by comparing simulation I to II, both defined in the table. Also it must be noted that when applying 80 grid cells or more for the z-direction, 40 grid cells are used over the fence instead of 20 grid cells. From the table two conclusions can be drawn.
First when only increasing the resolution in the z-direction the irregularity in the lower part of the profile, $z/h < 1$, disappears. Also multiple dents instead of one appear above the fence. The level of these changes is dependent on how the number of grid cells is divided between the fence and the gap above it. The more grid cells for one of both regions, the clearer the changes. 40 Grid cells or more for the fence height results in a smooth profile, i.e. irregularities of the profile are no longer present.
Second when only increasing the resolution in the x-direction the dent eventually disappears. However the irregularities increase.

In order to understand why the x-resolution is so important we take a look at the time-averaged streamlines around the fence. For simulations II, VI and VII, defined in the table, the streamlines around the fence are plotted in figure 5.13. In (a) one sees a streamline pattern as expected.

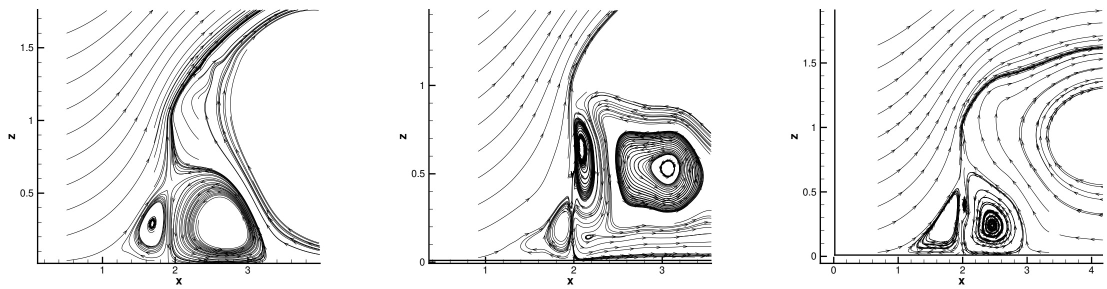

(a) (b) (c)

Figure 5.13: *xz-Cross-section of the channel plotting the streamlines around the fence for three different resolutions: (a) simulation II (b) simulation VI (c) simulation VII*

There are two recirculation zones behind the fence and one in front of the fence. When increasing the x-resolution a third recirculation zone appears behind the fence, see graph (b). Apparently the grid in simulation II wasn't fine enough to see this third recirculation. This does explain why the profile irregularities have grown for positions behind the fence for higher x-resolutions. When next to the x-resolution the z-resolution is raised, the third eddy disappears, see graph (c). And so do the fluctuations in the velocity profiles.

From figure 5.13 it is still not clear why the dent disappears. As mentioned a high enough x-resolution makes also the wiggles next to the dent disappear. We know now that the dent and the wiggles are related to the resolution, but if there is a relation between the dent and the wiggles remains unclear.

Simulation number VIII results in smooth velocity profiles using a reasonable resolution. Reasonable meaning that the computation time needed for this simulation lies within the time restrictions for this study. It is the only simulation in the table with a length of the channel of $30h$ instead of $40h$. Hence it will be the resolution used later on for simulating a correct fence flow.

5.2.4 Experiment

We have also performed an experiment and for two reasons. First we want to get an impression of the flow in physical reality. Especially the curvature of the shear layer at the separation point and the (non-)existence of a dent in the streamwise velocity profile are of interest. Second we want to know if the fence sheds vortices, since the simulation doesn't give vortices and it is not clear whether it should or not.

To do this a fence is put in a windtunnel. The fence and the channel have a respective height of $5cm$ and $20cm$. The thickness of the fence is roughly $2mm$. With an upstream velocity $U_{\text{inf}} = 1m/s$ this gives a Reynolds number of $Re_H = 13333$. Since this is the lowest upstream velocity achievable for the tunnel, it is also the lowest Reynolds number we can work with for this particular blockage ratio. It must be emphasized that the experiment is not intended to provide data for a quantative comparison with the previous simulation for several reasons. Among other things the performance of the hotwire is poor for the low value of $1m/s$ of the upstream velocity. Furthermore the hotwire technique used is unable to detect negative values of the streamwise velocity and has a large imprecision near the wall. Also the thickness of the fence and the shape of the top of the fence have a big impact on the resulting flow, as was found by Durst and Rastogi [9] in their experiments.
The streamwise velocity profile is measured using a hotwire at four different positions behind the fence. Two of these positions are within the range of x-positions from the simulation that exhibit a dent in the velocity profile. None is found in the measurements, indicating that the dent is a numerical phenomenon rather than a physical one.

In order to detect the shedding of vortices the streamwise velocity was measured as a function of time behind the fence using the hotwire technique. The resulting spectrum is shown in figure 5.14. It is measured at an x-position of $1cm$ behind the fence (x/H = 2,05) and at the same height as the top of the fence (z/H = 0,25). In the spectrum no clear peak, which indicates vortex shedding, can be detected. Again when using an upstream velocity $U_{\text{inf}} = 5m/s$, i.e. $Re_H = 66667$, no peak is found. Next we introduce smoke in front of the fence for both cases, but no clear shedding can be detected visually. From this we conclude that for this particular geometry and regime of Reynolds number Re_H the fence does not shed vortices. Neither does the fence in the previous simulation with a Reynolds number inbetween the ones used above.

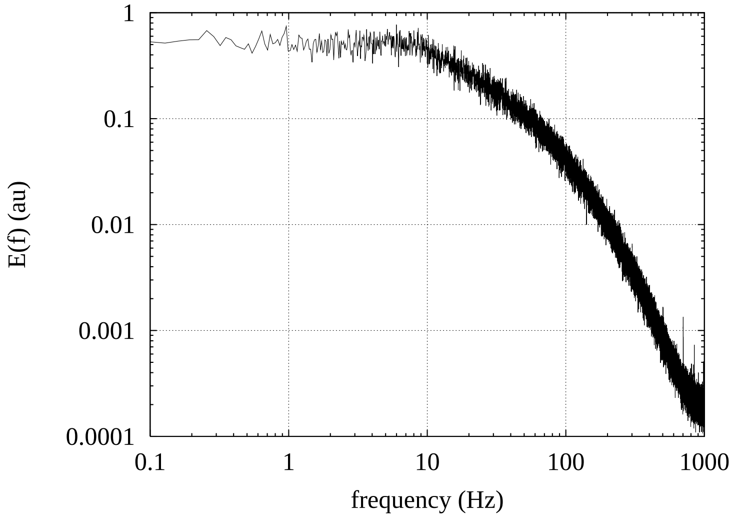

Figure 5.14: *Energy spectrum of the u-velocity* 1*cm behind the fence* 5*cm above the lower wall.*

5.3 Laminar simulations

In this section we will concentrate on two main subjects. First we will study the shedding of vortices using different values of physical parameters. We do this by studying laminar flows for reasons explained in the following subsection. Second we will study particle behaviour for particles of different sizes and take a closer look at particle behaviour around vortices.

5.3.1 Shedding of vortices

The simulated turbulent channel flow, using the parameters as discussed, does not shed vortices. Neither took there any vortex shedding place in the experiment. In order to get an indication of the values of the different parameters for which a channel fence flow sheds vortices, we first look at the laminar case. Experience tells us that a obstacle in a laminar flow often more easily and clearly sheds vortices than a turbulent one, since there is no third direction for the vortices. Furthermore for a laminar flow a less fine grid can be used. This strongly reduces the simulation time. From these laminar results we hope to get an indication whether a turbulent flow will shed vortices. Several laminar runs were performed using different parameters. For the z-direction at least 40 grid cells are used over the fence. For the y-direction only 1 grid cell is used and for the x-direction enough grid cells are used to prevent the existence of wiggles and a dent. All simulations have run for at least $60t$ after the flows have established themselves.

The results are listed in table 4.2. The frequencies are determined from time-series of the u-velocity at different positions in the channel. These frequencies can be transformed into the non-dimensional Strouhal number defined by

$$Str = f\frac{h}{U_0} \tag{5.2}$$

From the different simulations summarized in the table, a few conclusions can be drawn.
First of all increasing the Reynolds number, for the range we study, does not seem to have much effect on the shedding frequency and hence the Strouhal number. This complies well with the findings of Fang a.o. [1]. They found the same relation between Reynolds number and Strouhal number for a broad range of Reynolds numbers.
Increasing the Reynolds number also gives need for a longer channel. This is not a result of the wake becoming to long as can be seen in figure 5.15. More likely the shedded vortices stay stronger for a longer distance since the value of the viscosity decreases.
Applying a free-slip condition on to the upper wall instead of a no-slip condition, has no impact

H/h	U_0	Re_h	L/h	upper wall	Str
14	1	100	10	free-slip	0,05
14	1	500	10	free-slip	0,08
4	1	500	20	free-slip	0,1
4	1	100	10	free-slip	0
4	1	100	30	no-slip	0
4	1	125	30	no-slip	0
4	1	150	30	no-slip	0,08
4	1	200	30	no-slip	0,1
4	1	300	30	no-slip	0,09
4	1	500	30	no-slip	0,1
4	1	700	30	no-slip	0,11
4	1	800	70	no-slip	0,15
4	5	100	20	no-slip	0,5
4	5	100	20	free-slip	0,5
2	1	200	70	no-slip	0,07

Table 5.2: The shedding frequency found for simulations with different parameters.

on the shedding. The same goes for grid refinement for the z-direction near the upper wall.

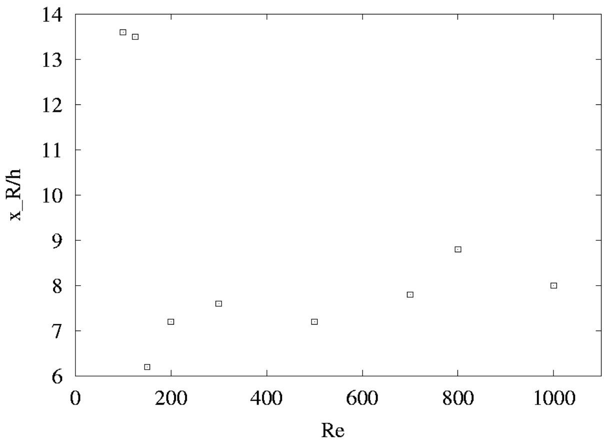

Figure 5.15: *The reattachment length x_R/h as a function of the Reynolds number Re_h.*

In figure 5.15 the first two Reynolds numbers result in very long wakes. These two Reynolds numbers correspond to the simulations in the table that don't shed vortices. From this result one can tell the big impact the shedding has on the reattachment length. For larger Reynolds numbers the recirculation length seems to increase slowly. That is what one would expect for flow in the laminar region. To be more precise Tropea and Gackstatter [4] found, that when looking to the dependence of x_R on the Reynolds number, three regions can be identified. A laminar region with a steady increase of x_R with the Reynolds number, a transitional region with an abrupt drop of x_R and a turbulent region in which x_R doesn't vary much with the Reynolds number.

Next we take a closer look at a fence flow and especially at the shedding, for one particular set of physical parameters. We perform a simulation using a Reynolds number of $Re_h = 750$ and a blockage ratio of $h/H = 0.375$. This blockage ratio, and not the previously used ratio of $H/h = 4$, is well within the range of conditions as defined in the US patent [5]. So is the Reynolds number. We like to find out if the fence sheds vortices for these parameters. Second, if shedding takes place, we want to determine the shedding frequency more accurately. The upstream velocity at the inlet is set at $U_0 = 1$. The resolution used is $300 \times 1 \times 40$ for a channel of size $20h \times 0.7h \times 2.7h$, with grid refinement for the z-direction at the top and bottom of the fence. The fence is positioned at a distance of $x/H = 1.3$ downstream of the inlet.

When looking at the u-velocity respectively the w-velocity as a function of time, a periodic movement of the velocity is found. So shedding does occur, as can be seen in figure 5.16. In

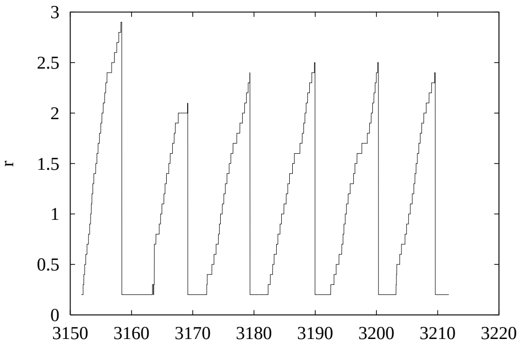

(a)

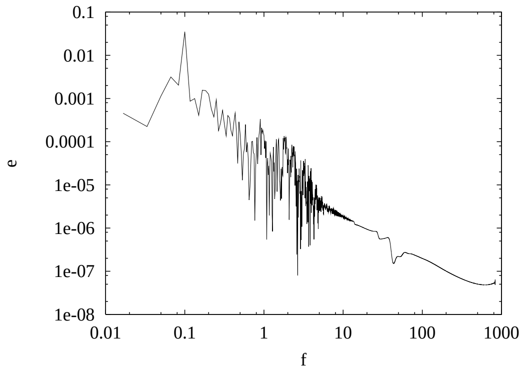

(b)

Figure 5.16: *(a) The vortex radius r as a function of time t determined at the height $z/h = 1$. (b) Energy spectrum of the u-velocity at position $x/h = 2.3$, $z/h = 1$. The frequency is depicted on the horizontal axis.*

(a) the vortex radius is shown as a function of time. The radius is determined by the distance from the x-position of the fence to the x-position where the w-velocity stops being positive and becomes negative. This distance is determined perpendicular to the fence. In (a) the radius is determined at the z-position of the top of the fence. The graph shows how a vortex slowly grows and suddenly separates from the top of the fence in a approximately periodic manner. The radius doesn't start growing at a value of zero due to the coarse resolution. This is because one can only start comparing the w-velocity with the velocity of the second grid cell from the fence, resulting in a threshold radius of $2 * 0,1$. For different z-positions on the fence approximately periodic results are found but with different values of the radius. In (b) the energy spectrum of the u-velocity produced by a fast-fourier transform is depicted at the position $x/h = 2.3$ and $z/h = 1$. It has a clear peak at $f = 0.1$. Using the upstream velocity and fence height, this leads to a Strouhal number of $Str = 0.15$. This value is very near to the Strouhal number in the order of $Str = 0.2$ for the shedding from cylinders. For different positions in the channel and also for the w-velocity similar graphs can be produced, but these are not shown here. Also note that using a coarse grid instead of a fine grid, like the one used in the simulations in table 4.2, and thus the appearence of wiggles and a dent has no impact on the shedding.

Thus a flow is established which sheds well defined vortices periodically and fulfills the conditions mentioned in the US patent [5]. Next we like to find out if changing the resolution for the z-direction has any influence on the shedding. The x-resolution is not refined in order to save computation time.

To study this the exact same simulation is performed except for the grid spacing in the z-direction. Next to refinement at the bottom and top of the fence, the grid was refined near the upper wall. The number of grid cells in the z-direction is raised to 80 resulting in a resolution of $300 \times 1 \times 80$ for a similar channel size. The fence now consists of 20 grid cells in the z-direction and the gap above the fence of 60 grid cells. The total simulation time is about $120t$. Again in figure 5.17 the vortex radius as a function of time is shown with the according energy spectrum. This velocity was taken at the same position as in figure 5.16.
From these graphs, especially from the peak in the spectrum, it is clear that shedding does occur. The earlier runs with only 20 grid cells for the gap, as was the case with the run described above, resulted in somewhat more regular shedding of vortices, i.e. the value of the vortex radius fluctuates less. This again indicates how important the resolution is for the geometry of a fence in a channel. .

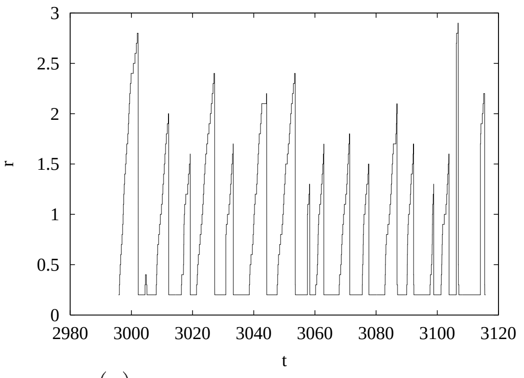

(a)

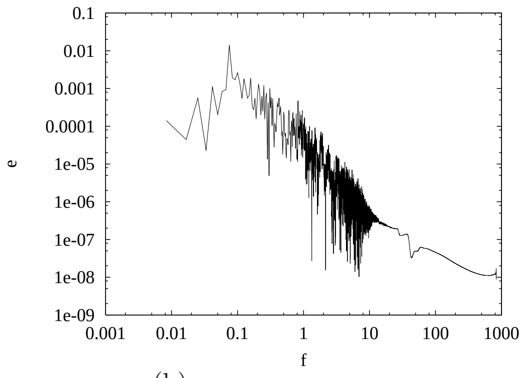

(b)

Figure 5.17: *(a) The vortex radius r as a function of time t determined at the height $z/h = 1$. (b) Energy spectrum of the u-velocity at position $x/h = 2.3$, $z/h = 1$. The frequency is depicted on the horizontal axis.*

5.3.2 Particles

Interaction particles/vortices

Until now particles were not of primary interest. As explained earlier the vortices are meant to trap the particles. In order to check whether particles will indeed agglomerate in the vortices, we first look how the particles interact with the vortices. What one expects is for very light particles to be in equilibrium with the fluid and to follow the streamlines of the flow. Heavy particles, on the other hand, will be unaffected by the vortex flow because of their large inertia. This gives way for an intermediate size of particles that tend to be centrifuged from the vortex cores and accumulate at the edges of the vortices. The extent of the particle-vortex interaction will depend also, apart from inertia, on fluid properties. Both particle and fluid properties are captured respectively in the relaxation time of the particles and the time associated with the fluid motion in the vortex scales. The latter time scale is defined as

$$\tau_v = \frac{\mathcal{L}}{\mathcal{U}} \tag{5.3}$$

where $\mathcal{L}$ is the length scale associated with the vortex and $\mathcal{U}$ is a representative flow velocity of the vortex. The responsiveness of a particle to the vortical flow depends on the ratio of the particle relaxation time to the fluid time. This ratio is called the Stokes number

$$St = \frac{\tau_p}{\tau_v} = \frac{2}{9}\frac{\rho_p a^2 \mathcal{U}}{\rho \nu \mathcal{L}} \tag{5.4}$$

Particles with Stokes number $St \ll 1$ tend to follow the fluid, while particles with Stokes number $St \gg 1$ will be unaffected by the flow. At intermediate Stokes number $St \approx 1$ particles will get strongly influenced by the global vortex structures.

To investigate the interaction, a laminar flow is simulated which is known to shed vortices. The Reynolds number used is $Re_h = 750$ with a blockage ratio of $h/H = 1/3$. The resolution is $1800 \times 1 \times 80$ for a channel of size $30h \times 1h \times 3h$, with grid refinement for the z-direction at the bottom of the channel and at the height of the top of the fence. From section 5.2.3 we know this results in a flow without a dent and without wiggles. In order to determine what size of particles we introduce to the channel, we first have to make an approximation of τ_v. To do this we look at the w-velocity profiles around a vortex, as shown in figure 5.18. Here the instantaneous w-velocities as a function of the x-direction around a vortex are shown. They are plotted for two different times, so for two different vortices. For other t's similar values can be found. We take the positions of maximum values of the w-velocity as the positions of the edges of the vortex. We find the following length scale $\mathcal{L} = 2h$ and velocity scale $\mathcal{U} \approx 1.8$, resulting in a $\tau_p \approx 1$. Since we would like to see how different sizes of particles behave differently, we use particles corresponding to

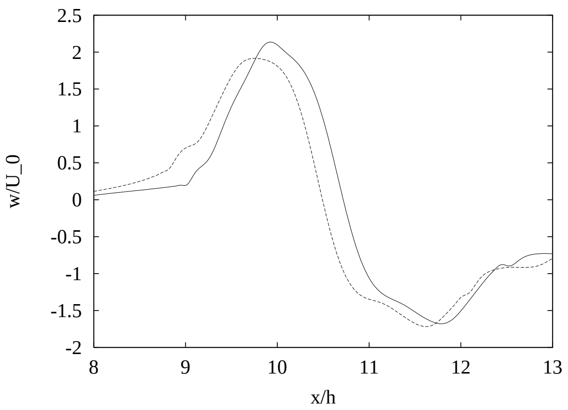

Figure 5.18: *Instanteneous w-velocity as a function of the length of the channel for 2 different times at a certain height.*

values of the Stokes number that are smaller and larger than unity. To be more precise, particles with the following four kind of relaxation times $\tau_p = 4 * 10^{-4}$, $\tau_p = 0.04$, $\tau_p = 0.4$ and $\tau_p = 4$. Since the particles with $\tau_p = 0.4$ correspond to a Stokes number with a value closest to $St = 1$, we expect these to be most strongly influenced by the vortices.

Since we are interested only in the behaviour of the particles due to the force applied by the fluid, the gravity force is ignored for this case. The boundary condition for the particles on the upper and lower channel wall and on the fence is an elastic collision routine. This way the particles are kept in the flow without them lingering near the walls and therefore more of the particles interact with the vortices. We are not yet interested in deposition. For every value of τ_p, 5000 particles are included after the flow has had $35t$ to establish itself. The total simulation time including the particles is another $35t$.

In figure 5.19 the velocity vectors of the particles at their instantaneous positions are shown for all four relaxation times. In (a) the smallest particles are spread all over the channel, including just behind the fence, indicating that these adjust to the flow very fast. This is also clear from the circular forms at the position of the vortices created by the vectors. Although these vectors are plotted too small to detect separately, together they create the circular form since their direction complies well with the direction of the flow in the vortices. In (b) the somewhat larger particles are centrifuged outside of the vortices leaving particle-free spaces. In (c) this effect is even stronger creating particle filled lines between consecutive vortices. Finally in (d) the particles, due to their high inertia, start to ignore the vortices. We can conclude that the different sizes of particles indeed behave as expected and that the size of particles with a Stokes number closest to $St = 1$, which is $\tau_p = 0.4$, are influenced most by the vortices.

One wonders whether or not the velocity- and length scale used to determine τ_v are still valid at the end of the channel. In other words whether or not the vortices change somewhat when travelling through the channel. If so this is bound to influence the interaction with the particles. However when looking at figure 5.19 one finds the same particle patterns in the second half of the channel as just behind the fence, suggesting no real differences. In figure 5.20 two instantaneous w-velocity profiles are again shown around a vortex and again corresponding to two different times. However this time the vortices are about $10h$ further downstream than the ones shown in figure 5.18. As one can see there aren't any significant differences between both figures, indicating that the vortex scales don't change much when travelling downstream.
Figure 5.20 also provides us with a x-resolution criterium for very large vortices. In this study we work with an equidistant x-resolution in order to be able to resolve vortices not just directly behind the fence but also at the end of the channel. If we set the criterium for resolving a vortex to having 10 gridcells in the x-direction over the length of a vortex, we can set a minimum x-resolution for this particular simulation. Since the vortices have a length of $\mathcal{L} = 2h$ we need a minimum of 5 gridcells per h. However we know that such an equidistant coarse grid results in wiggles and a dent. Moreover if we want to see particles accumulate at the narrow edges of vortices we need a

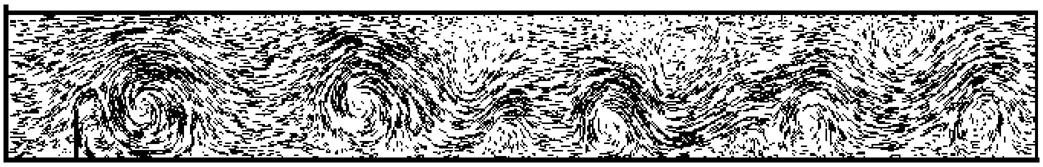

(a)

(b)

(c)

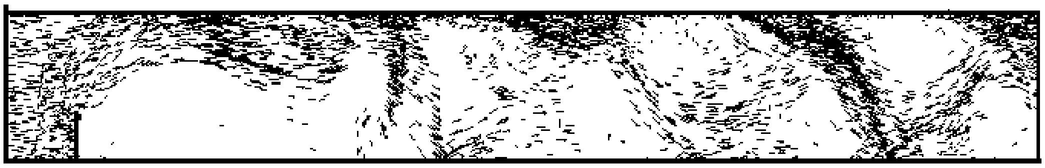

(d)

Figure 5.19: *xz-Cross-section of the channel with the velocity vectors of the particles plotted at their instantaneous positions for (a) $\tau_p = 0.0004$ (b) $\tau_p = 0.04$ (c) $\tau_p = 0.4$ (d) $\tau_p = 4$. Ratio length/height of the channel is x/z = 0.7*

much finer resolution.

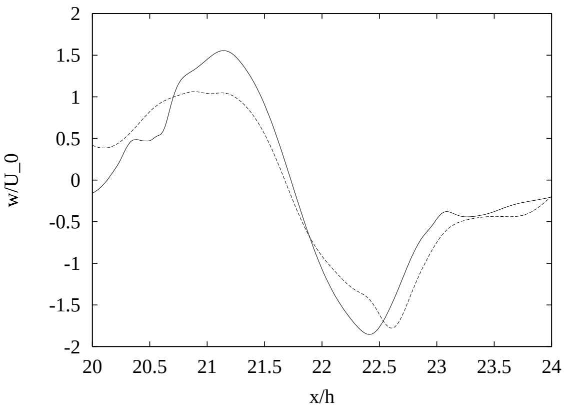

Figure 5.20: *Instanteneous w-velocity as a function of the length of the channel for 2 different times at a certain height.*

Effect of wiggles and dent

Exactly the same simulation is repeated but this time with much less resolution, resulting in a flow with a dent and wiggles. Our aim is to find out whether or not these wiggles and dent exert any influence on the particle behaviour. Hopefully this will give us some insight about the validity of the particle results in section 5.2 where wiggles and a dent are present.

The resolution used is $300 \times 1 \times 80$ for the same domain. The grid refinement in the z-direction remains the same. The same amount of particles are used with the same relaxation times and same boundary conditions. After the flow has established itself, flow- as well as particle-data is collected over a period of $45t$.

In the simulation the fence sheds vortices in a similar fashion as the previous high resolution simulation. There is a difference in reattachment length between both simulations. Whereas

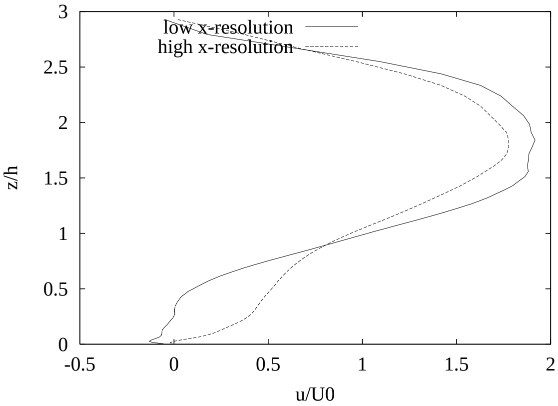

Figure 5.21: *Time-averaged u-velocity as a function of the height of the channel at a x-position of* $5.1h$ *downstream of the fence.*

for the low resolution it has a value of $x_R = 5,3h$, it has a smaller length $x_R = 4h$ for the high resolution. In figure 5.21 one can see the time-averaged u-velocity of the low x-resolution simulation still have negative values near the wall. The difference cannot be explained by the number of gridcells alone, i.e. the difference in the width of a gridcell Δx. From this we can conclude that a high resolution for the x-direction is absolutely essential to produce an accurate physical flow.

To study the particle behaviour, we construct time-averaged particle concentration profiles for all τ_p's. Our main interest for the concentration goes out to the area directly behind the fence in and above the wake, i.e. around $x/h = 5$. We like to find out after all if wiggles in front of the fence have any effect on the particle behaviour directly behind the fence. The concentration is determined over a vertical slab of the channel around $x/h = 5$ in order to calculate the concentration of a sizable amount of particles. This amount consists typically of around 500 to 600 particles. Since the concentrations are also averaged over a long period of time the profiles should give a good indication. In figure 5.22 the time-averaged particle concentration for this region is shown as a function of the height, where the concentration is normalized. From the figure it's clear that the concentrations compare relatively well for both resolutions. For example in graph (b) to (d) both simulations have low concentrations in the wake. The reason both profiles are not exactly alike is first of all a result of the randomized introduction of particles at the inlet. More importantly however, we just saw lack of x-resolution resulting in a larger wake. Thus when determining the concentration around $x/h = 5$, we determine the concentration over a different part of the wake for both resolutions. For the particle sizes depicted in graph (c) and (d), all particles accumulate in the area above the wake. The surface of this area differs for both resolutions ,due to their difference in wake height, and hence so do the particle concentrations. From all of this we can conclude that the wiggles and dent have no impact on the general flow behaviour downstream of the fence. With this we can make a case for the validity of the particle results from the original turbulent simulations performed in section 5.2. There is still the difference that in section 5.2 we performed a 3-dimensional turbulent run and here a 2-dimensional laminar run. Since the wiggles

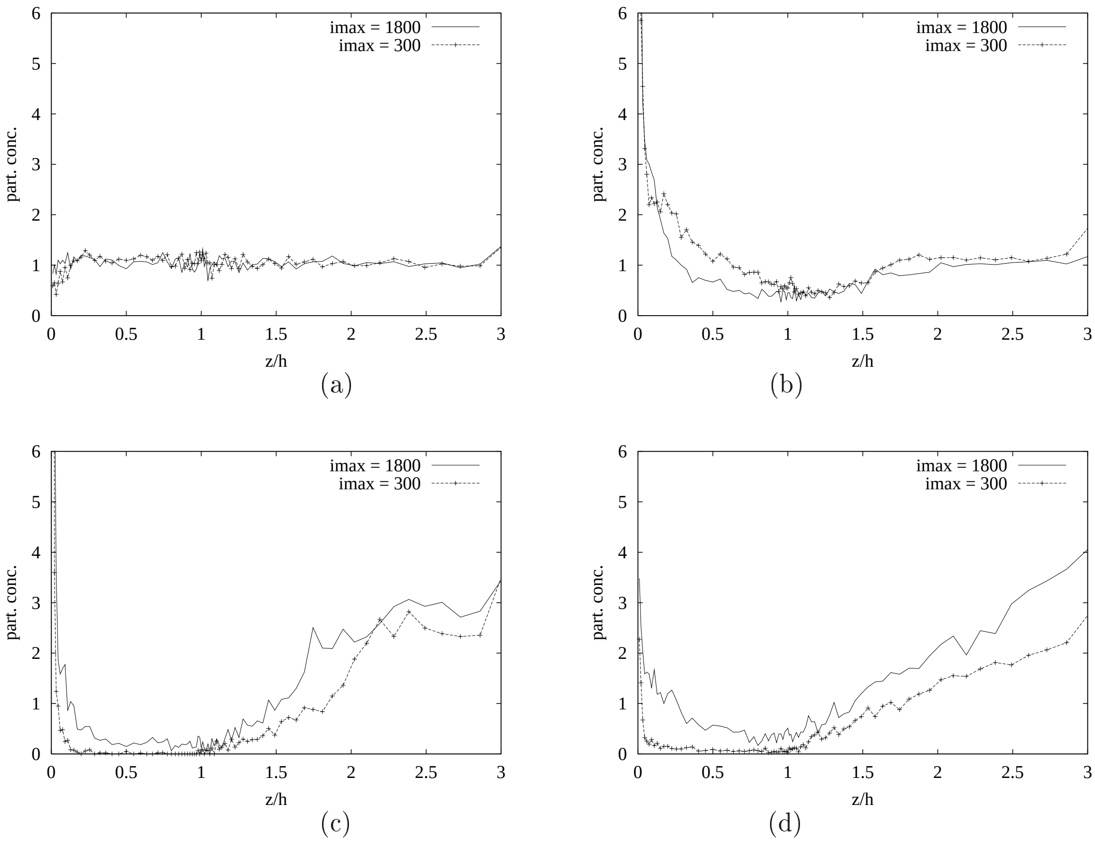

Figure 5.22: *Time-averaged normalized particle concentration as a function of the height of the channel, around $x/h = 5$, for both resolutions (imax = 300 and imax = 1800) using (a) $\tau_p = 0.0004$ (b) $\tau_p = 0.04$ (c) $\tau_p = 0,4$ (d) $\tau_p = 4$*

and dent are a strictly 2-dimensional phenomenon (they are simply not there in the third dimension), this difference has no effect on our claim. We can conclude that our conclusions concerning the particles in section 5.2 are valid.

Deposition

In this section we test the principle of the experiment described in the patent [5]. This principle consists of their finding that when particle-filled vortices, shedded from a fence, encounter a second fence further downstream, the vortices dissolve and the particles will deposit in the vicinity of the second fence. They used small cavities in the lower wall around the second fence to remove these particles from the flow, in other words to substantiate deposition. This two-fence channel flow should therefore provide us with a way to extract particles from a flow, one of the initial goals of this study.

To study this two laminar simulations are performed. A simulation of a channel with one fence and a simulation with two fences. Both simulations are performed using similar parameters as the ones used above, i.e. $Re_h = 750$ and $h/H = 1/3$ for all fences. These two values fall within the range prescribed by the patent. The resolution used is $3840 \times 1 \times 40$ for a channel of size $64h \times 1h \times 3h$. The first fence is positioned $6h$ downstream of the inlet and the second fence, in case of the two-fence simulation, $36h$ downstream of the inlet.

Two sizes of particles are used having a relaxation time of respectively $\tau_p = 0,4$ and $\tau_p = 4$. Since the first of these two is found to be most strongly confined by the vortices, it should also deposit best according to the patent. To check this the other particles are included, which are

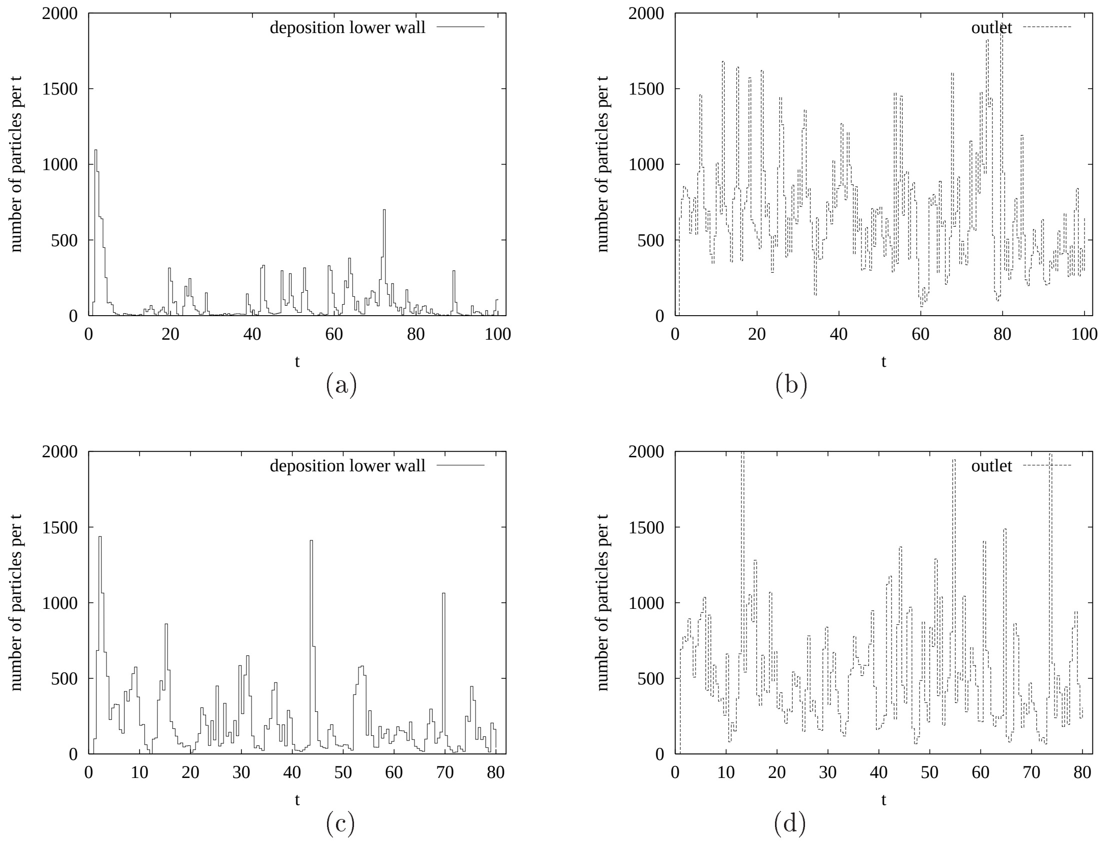

Figure 5.23: *Number of particles escaping the channel per t for: (a) lower wall/1-fence (b) outlet/1-fence (c) lower wall/2-fences (d) outlet/2-fences. Particles have relaxation time of* $\tau_p = 0.4$*.*

larger. In these simulations there is no gravity force acting on the particles. This is done to make sure that when the larger particles happen to deposit better on the lower wall, we will know it is not due to the gravity force. In other words the results concerning the deposition will not be destorted by a gravity force, which will be different for both kind of particles. It is fair to make the assumption that the gravity force, when applied, will only enhance the deposition of the particles on the lower wall. To simulate the deposition we don't create cavities in the lower wall but instead simply remove a particle from the flow when it reaches the lower wall. Just like the particles reaching the outlet they are reintroduced at the inlet where they get the same u-velocity as the fluid at the inlet. Thus the total number of particles in the channel remains constant. The boundary condition at the fences and the upper wall is an inelastic collision routine. Of each size of particle 50000 are introduced after the flow has established itself.

In figure 5.23 and 5.24 the number of particles deposited or escaping at the outlet per t is depicted for both relaxation times and for both the one- and two-fence simulation. In 5.24 one can see that the larger particles have a high deposition rate at the start and need some more time to adjust than the other particles. From figure 5.23 it seems that for this specific τ_p the principle of the patent works. After the same amount of time more particles have deposited in the two-fence simulation than in the one-fence simulation. When studying the total deposition, instead of the deposition rate, 1 out of 6 particles deposit in the two-fence simulation and 1 out of 12 in the one-fence simulation.
However for the larger particles, figure 5.24, the principle doesn't seem to work, indicating that the question whether or not a second fence increases deposition is dependent on the particle relaxation time. Here 1 out 3 particles is deposited for both the one- and two-fence simulation.
Comparing the two-fence simulation for both kind of particles, figure 5.23 (c) and (d) and 5.24

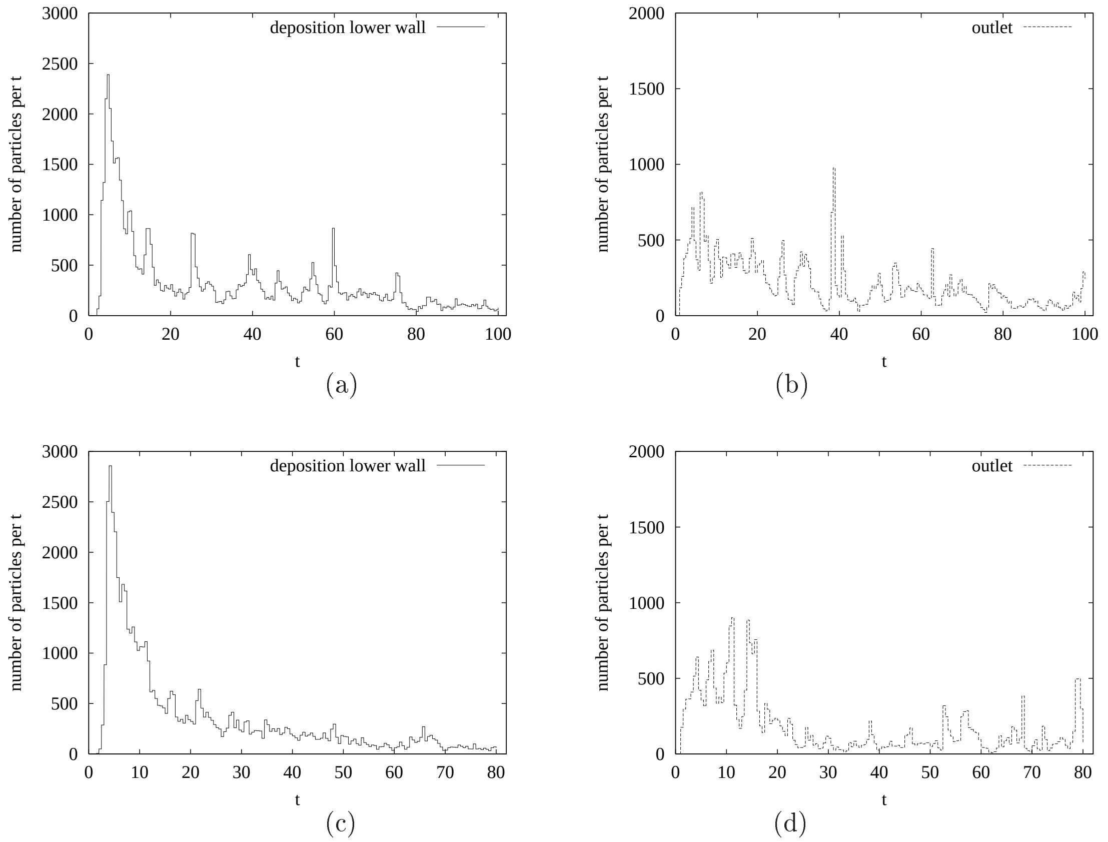

Figure 5.24: *Number of particles escaping the channel per t for: (a) lower wall/1-fence (b) outlet/1-fence (c) lower wall/2-fences (d) outlet/2-fences. Particles have relaxation time of* $\tau_p = 4$.

(c) and (d), shows the particles with $\tau_p = 4$ depositing much better. When comparing figure 5.25 to 5.26 it is clear that much less particles are present with $\tau_p = 4$, at the end of the channel, than particles with $\tau_p = 0.4$. We know this is not due to gravity. The same goes for the one-fence simulation, figure 5.23 (a) and (b) and 5.24 (a) and (b). This is probably due to the fact that much more of the smaller particles, $\tau_p = 0.4$, reach the outlet of the channel than do the larger particles. This is not surprising since these smaller particles are much more confined to the vortices and are therefore less likely to reach the lower wall. All in all we can now say that a second fence will only improve the deposition of particles when these particles are trapped in vortices. It seems much more beneficial for deposition to avoid particles getting caught in vortices and thereby eliminating the need for a second fence.

Figure 5.25: *xz-Cross-section of the channel with the velocity vectors of the particles plotted at their instantaneous positions for* $\tau_p = 0.4$.

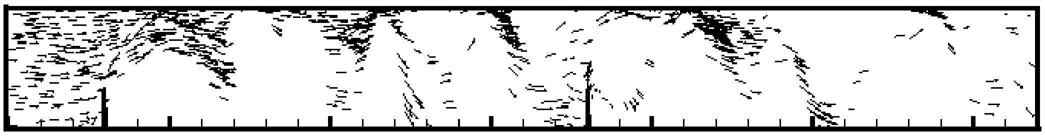

Figure 5.26: *xz-Cross-section of the channel with the velocity vectors of the particles plotted at their instantaneous positions for* $\tau_p = 4$.

5.4 3-D simulations

5.4.1 Conditions for turbulent flapping and stability

In this section we discuss in short the problems we encounter when establishing a working 3-dimensional simulation. The simulations adressed in the previous section are all basically 2-dimensional flows. The number of grid cells in the y-direction is in all cases much too low to substantiate a turbulent flow. (Only 1 or 4 cells for the y-direction.) In this section we take the 2-dimensional simulation performed in section 5.3.1 but now use 20 grid cells for the y-direction. This increase of the y-resolution, i.e. the creation of a 3-dimensional flow, together with a high Reynolds number and a disturbance in the flow, as created by the fence, should result in a turbulent flow. For now however we stick to the low Reynolds number of $Re_h = 750$ as used for the 2-dimensional run in order to be able to better compare both simulations. Summarized this means a resolution is used of $300 \times 20 \times 40$ for a channel of size $20h \times 1.3h \times 2.7h$. All other parameters are kept equal to the 2-dimensional simulation.

During the simulation the fence initially sheds vortices, but the run explodes after $60t$. Normally this indicates that there is fluid flowing back into the channel at the outlet and this indeed seems to be the case. This cannot be due to the wake behind the fence since it fits well within the channel. A likely reason is that the vortices have become larger and therefore, when they reach the end of the channel, more fluid flows back into the channel. Findings by Peng and Hwang [3] show that for laminar flow a 2-dimensional simulation has a significantly shorter recirculation zone than the experimental data, while a 3-dimensional simulation corresponds well with the data. If a larger wake also gives larger vortices, this would suggest a larger vortex radius for a 3-dimensional simulation. For the initial period the fence sheds vortices the results are given in figure 5.27. In

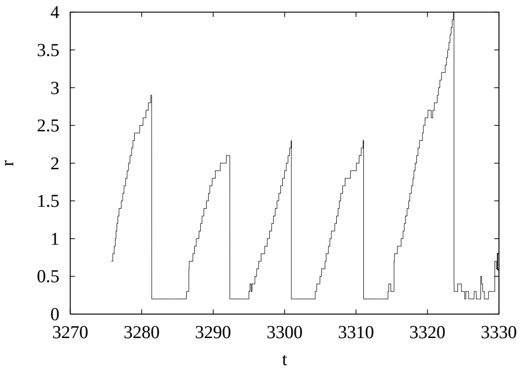

(a)

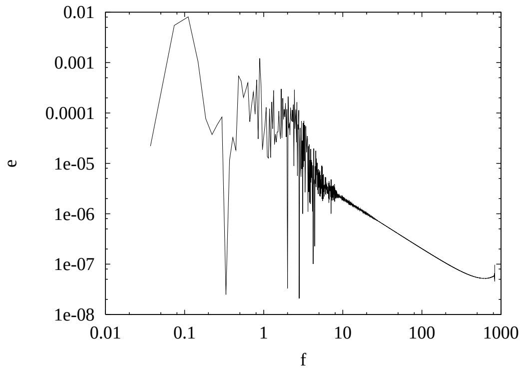

(b)

Figure 5.27: *(a) The vortex radius r as a function of time t determined at the height* $z/h = 1$. *(b) Energy spectrum of the u-velocity at position* $x/h = 2.3$, $z/h = 1$. *The frequency is depicted on the horizontal axis.*

(a) a very large vortex is indeed just shed before the run explodes, and could be the culprit.

Since we want to achieve a 3-dimensional model that works for various values of parameters, several attempts are made to prevent the channel from exploding, as listed below.

- Expanding the channel to a length of 40 respectively 50 dimensionless length scales, results again initially in shedding vortices. However after about 3 shedding periods the shedding stops and the simulation explodes. Regardless of the results, expanding the channel beyond a length of 30 is not really an option because of the calculation time involved.

- Switching on the subgrid model, i.e. transforming the simulation into a LES. In a LES the viscosity generally has a larger value and it is this larger value that could damp the vortices in such a way in order for the channel length to suffice. In this model a Van Driest constant is calculated as was defined in equation 4.26 in order to reduce the viscosity near the walls. Until now it was only calculated for the upper and lower wall, not the fence. Here however we also make this viscosity adjustment near the fence.

  After $25t$ only one vortex has shed. Furthermore the simulation uses a very small timestep, making the run extremely slow. This small timestep is determined by the flow in the region just above the top of the fence, where there's grid refinement in the z-direction. Here the distance to the fence is very small and since the Van Driest constant at a certain point is determined using the shortest distance to a wall (or fence), it takes on a large value just above the fence. Actually resulting in the largest value for the Van Driest-constant throughout the channel. This results in a lower viscosity and thus a higher velocity. Hence the smaller timestep.

  This very small timestep immediately eliminates the option of adjusting the Van Driest constant for the top of the fence, since we simply cannot afford the computation time needed. When we only make the adjustement for the sides of the fence and not the top, the timestep doesn't decrease from its original value. Furthermore the timestep keeps its value when using a higher resolution in the x-direction needed for a well solved flow, (1800 grid cells instead of 300). Even here the timestep is still determined at the top of the fence.

  However using the subgrid model, with or without various adjustments to the Van Driest constant, doesn't prevent the simulation from exploding. In the simulations to follow, in this and following sections, we only use adjustments of the Van Driest constant for the sides of the fence, not the top. We do perhaps make a consession to physical reality by making this adjustment only for both sides of the fence and not the top, though all these adjustements seem to have no effect on the shedding of vortices.

- The implementation of a convective boundary condition at the outlet of the channel. This boundary condition is applied to all directions of the flow and is given by

  $$\frac{\partial \mathbf{u}}{\partial t} + U_0 \frac{\partial \mathbf{u}}{\partial x} = 0 \tag{5.5}$$

  The simulation (without the subgrid model) starts to shed very irregularly after 4 shedding periods and eventually explodes. Near the upper wall very large fluctuations of the velocity are found probably due to grid cells too large.

- Grid refinement is then applied near the upper wall and the convective boundary condition is used. The resolution used is $300 \times 20 \times 80$. The simulation explodes for various distributions of the grid cells for the z-direction.

- To the attempt above the subgrid model is added. This should increase the overall viscosity and slightly have damped the vortices when they reach the end of the channel. After $45t$ and 5 shedded vortices the divergence becomes too large and the simulation explodes.

- The simulation mentioned in the previous item but with a reduced Reynolds number of $Re_h = 100$ again explodes. One expects the low Reynolds number to increase the viscosity and consequently damp the vortices even more.

- Finally we try a damping mechanism at the end of the channel, named the fringe method (see Lundbladh e.a. [6]). At the same time none of the above described adjustements is implemented. It consists of adding forcing terms to the NS equations in part of the computational domain to damp disturbances, i.e.

  $$\frac{\delta \mathbf{u}}{\delta t} = NS(\mathbf{u}) + \lambda(x)(\mathbf{v} - \mathbf{u}) \tag{5.6}$$

where $NS(\mathbf{u})$ is the normal part of the NS equations and $\mathbf{v}$ the prescribed velocity vector we want at the outlet of the channel. $\lambda(x)$ is called the fringe function and is non-zero only in a small region at the end of the channel, termed the fringe region. One possible form of this function is as follows

$$\lambda(x) = S(\frac{x - x_{end}}{\Delta_{region}} + 1) \tag{5.7}$$

where x_{end} is the end of the region where the damping function is non-zero, in our case the end of the channel. Δ_{region} is the extent of the fringe region, for which we use an x-distance of $\Delta_{region} = h$. $S(x)$ is a smooth step function rising from zero for negative x to one for $x = 1$

$$S(x) = \begin{cases} 0 & x \leq 0 \\ 1/[1 + \exp(\frac{1}{x-1} + \frac{1}{x})] & 0 < x < 1 \\ 1 & x = 1 \end{cases}$$

Now in our study we force the u-velocity at the end of the channel to a value of $1U_0$, whereas we force the v- and w-component of the velocity to a value of zero. When we implement this fringe method in the simulation mentioned above, the simulation does not explode. Though sadly at a certain point it stops shedding vortices.

Using this last fringe method we are finally able to perform a 3-dimensional simulation and in the following sections this method is applied in the simulations together with the before mentioned partial correction for the Van Driest constant and the subgrid model.

5.5 Large eddy simulations

Now that we are able to simulate a 3-dimensional channel flow with a surface-mounted fence, we take a closer look at two specific cases. First a channel flow is looked upon with a very small blockage ratio. The results from this simulation can be compared to data available in the literature. Next we study a channel flow with a large blockage ratio and a small Reynolds number, both of which fall within the prescriptions of the patent. We want to know if the fence sheds vortices.

5.5.1 $Re_h = 2950; h/H = 1/8$

Introduction

In this section a simulation is performed in order to compare its results with those of an experiment performed by Lee [7]. Lee studied the turbulent flow around a fence. He worked with a Reynolds number of $Re_h = 2950$ and a blockage ratio of $h/H = 1/8$. Here we use the exact same parameters. The resolution we use is $1800 \times 20 \times 100$ for a channel of size $30h \times 1h \times 8h$. For the z-direction grid refinement is applied to the lower wall and the top of the fence. In the simulation the fence is placed at $x = 7h$ downstream of the inlet, instead of a distance of $20h$ like the experiment. This is done in order to save computation time because of the high resolution for the x-direction. We know from Lee's experiment that at a distance of $5h$ upstream of the fence, where according to Lee the fence has yet no impact on the velocity profile, the boundary layer thickness should be about $\delta/h = 0.5$. In order to produce a similar inlet flow an extra (fenceless) channel is simulated simultaneously. The resolution used for this extra channel is $20 \times 20 \times 100$ for a domain of $4h \times 1h \times 8h$. The Reynolds number is again $Re_h = 2950$. The outlet velocity profile of this extra channel is used as the inlet profile for the main channel. Unfortunately in our simulation the flow in the extra channel has not yet established itself when we start the fence simulation. We only became aware of this fact after the simulation was performed. This regrettably makes it harder to make a good comparison with experimental data. In this extra channel it is made sure that the bulk velocity has a value of $U_0 = 1$ every single time step. This explains why the channel with the fence does still produce the u-velocity profile as was found by Lee at a distance of $5h$ before the fence, despite the non-established extra channel. At this same x-position we will find that in our simulation the flow is not yet influenced by the fence which is in agreement with the experiment. The total simulation time is $85t$. During the last $33t$ data is obtained. The simulation starts with the fence shedding vortices in a very irregular manner, but this shedding soon stops.

In this section we also discuss RANS-simulations making use of two turbulence models, respectively the $k - \epsilon$ model and the Re-stress model, described in section 4.4. Both models are applied using the commercial package FLUENT 6. In these simulations a geometry is used equal to the one used in our LES. However the grid we use when applying the two turbulence models is, apart from the z-direction, also non-equidistant for the x-direction, in order to save computation time. This means grid refinement around the fence for the x-direction. Special care is taken to make sure that enough grid cells are present for this direction throughout the domain to solve all interesting parts, most notably to determine the wake length with enough precision. Furthermore it is made sure that the smallest gridcells, present at the positions of grid refinement, have the same size as the ones used in the LES for both the x- and z-direction. FLUENT approaches the problem 2-dimensional so we can ignore the y-direction. Both the $k - \epsilon$ model and Re-stress model are solved using an unsteady 2nd order implicit scheme and 2nd order upwind discretization. At the inlet we provide a u-velocity of $U = 1m/s$ over the height of the channel, a turbulence intensity of 2% (as indicated by Lee) and a turbulence length scale of $0.5m$. This does not correspond to the inlet profile of our LES, as we know now, but should correspond to the inlet field of the experiment. Both models make use of standard wall functions. The unsteady simulations are performed using a fixed timestep of $0.001s$. This timestep is of the same order of magnitude as the one in the LES and thus should allow us to see periodic movements in the flow when present. The simulation using the $k - \epsilon$ model has a total simulation time of $54t$ of which the last $11t$ are used to calculate time-averages. For the Re-stress model the total simulation time is $77.6t$. Time-averaging takes place over the last $33.6t$. This simulation starts, just like the LES, initially with the shedding of vortices. This phenomenon is not observed when using the $k - \epsilon$ model.

Mean velocity field

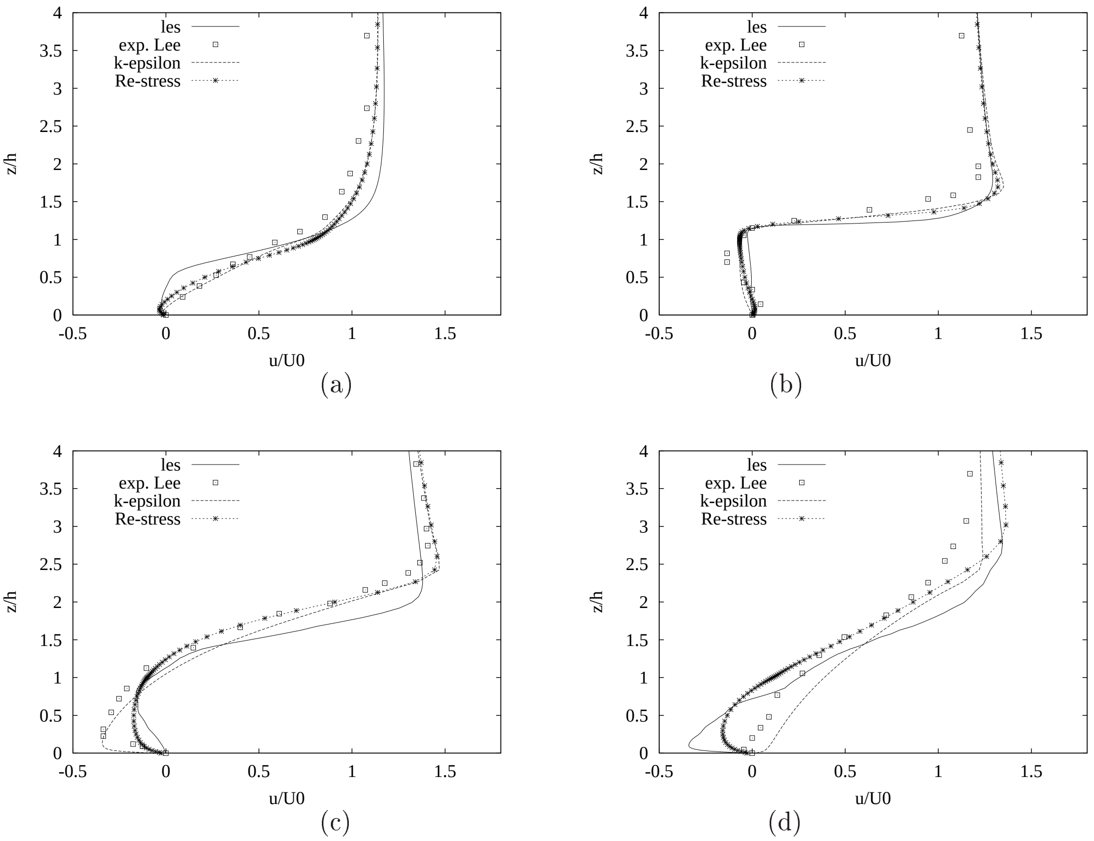

Figure 5.28: *The time-averaged u-velocity u/U_0 as a function of the height z/h for the following x-positions: (a) $x/h = 6.5$ (b) $x/h = 7.5$ (c) $x/h = 11$ (d) $x/h = 18$*

We first focus on the LES results. In figure 5.28 the time-averaged u-velocity as a function of the height of the channel is shown for four different x-positions. The results do not agree that well with the experimental data. First of all the reattachment length is much larger than the one found in the experiment. From the LES we find a value of $x_R = 14h$ whereas Lee found a value of $x_R = 11.2h$. This is very clear in graph (d) where in our simulation, in contrast to the experiment, there are still very large negative velocities near the lower wall. An explanation for this difference could be that the reattachment point moves intermittently back and forth on the wall. When analyzing instantaneous u-velocity profiles for successive times this movement can be detected. So, when calculating the time-averaged velocity profiles of figure 5.28, it is important to average over an exact number of periods of this movement. Naturally the exact time associated with a number of periods is hard to define and hence the solution will always be slightly biased. This bias can be reduced by averaging over a long period of time. This presents us with a problem since the computation time per timestep is very high. In order to finish the LES within a reasonable amount of time we were eventually only able to average over a time of $30t$ corresponding to one period of movement of the reattachment point. This would suggest a frequency of roughly $f = 0.033$ for the shifting of the reattachment point. Lee also mentioned this movement of the reattachment point and subscribed it to the downstream shedding of vortices. He claims to have observed this shedding, but adresses it only very briefly and for instance does not associate a time scale with it. However in our simulation the fence does not shed vortices.
Also apparent in figure 5.28 are the discrepancies that exist between the simulation and the experiment for z-positions within the wake . These are a consequence of the difference in wake length. One expects the maximum negative u-velocity to appear at the x-position in the middle of the wake and since the wake lengths are not equal, these negative velocities do not appear at

the same x-position. So it is of not much use to compare the u-velocities in the region of the wake. The maximum mean reverse u-velocity we find is $u/U0 = -0.32$ compared to $u/U0 = -0.36$ found by Lee.
Something else which is apparent from figure 5.28 is that for z-positions approaching $z/h = 4$ the simulation gives a higher u-velocity for most x-positions. This is probably due to the fact that Lee based his Reynolds number on the free-stream velocity which differs slightly from the bulk velocity we use when using the same Reynolds number.

We also plotted in figure 5.28 the averaged velocity profiles produced using the $k - \epsilon$ model and the Re-stress model. Both models produce a different time-averaged reattachment length. This can be seen in graph (d), for an x-position which is out of the wake for the $k - \epsilon$ model and in the wake of the Re-stress model. More specificially the $k - \epsilon$ model results in a reattachment length of $x_R = 10.2h$, which is even shorter than the length found by Lee. This short length could be related to the fact that the model doesn't solve a second recirculation zone behind the fence, as do the other simulations. The Re-stress model gives a length of $x_R = 13.1h$, which is close to the length found for the LES. In (a) and (b), where their difference in wake length has none to little effect, the velocity profiles of both models compare to eachother very well. For z-positions approaching $z/h = 4$ they also have larger velocity values than the experimental ones, probably for the same reason as mentioned before.

Another set of experimental data used by Jakirlic [8] is available. Here the Reynolds number is $Re_h = 3000$ and the blockage ratio is $h/H = 1/7.5$. Both parameters only differ slightly from the ones we use in our simulation and should therefore not play any significant role. In figure 5.29 the time-averaged u-velocity is again plotted for various x-positions together with the experimental data used by Jakirlic. Once again it appears that the reattachment length for the LES is not well predicted. The averaged length given by Jakirlic is $11.7h$. Hence it is no use comparing the profiles for z-positions within the wake.
Furthermore the u-velocity for z-positions higher than the fence height is systematically underpredicted for the LES. Although one expects the u-velocity of these z-positions for the experiment to be a bit higher due to an increased blockage ratio, the increase of around 0.2 seems a lot. This suggests that the two experimental data sets don't compare that well themselves. Because no data exists for the exact same x-positions in both experiments an actual comparison cannot be made.

Again the averaged profiles resulting from the $k - \epsilon$ model and Re-stress model are shown in the figure. For the x-position of the fence, graph (b), FLUENT was unable to plot the velocities correctly. We blame this on the plotting tool of FLUENT, since for instantaneous velocity profiles the values are plotted correctly. We already know the models produce different wake lengths. Hence the somewhat different profiles for both models in graphs (c) to (f). At x-positions before and on the fence both models agree perfectly with eachother and reasonably with the LES.
Just like the LES, the other simulations systematically result in smaller u-velocities for z-positions higher than the fence compared to the experiments. The comparison of both models to the LES is not perfect since their recirculation zones downstream of the fence have a different size compared to the LES. On the x-position of the fence they compare very well. Overall the profiles of the models are more similar to the LES results than to the experimental profiles.

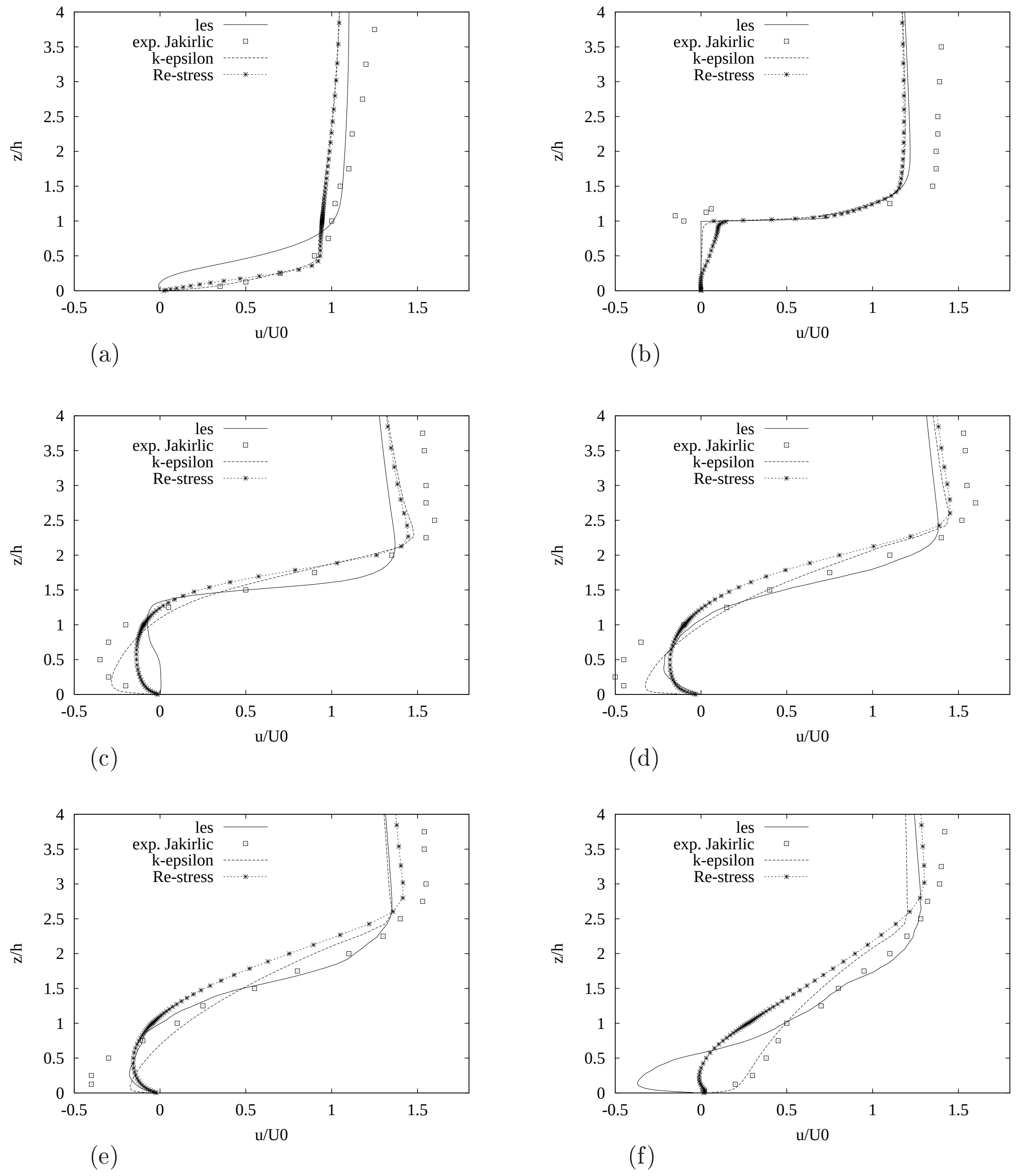

Figure 5.29: *The time-averaged u-velocity u/U_0 as a function of the height z/h for the following x-positions: (a) $x/h = 4.5$ (b) $x/h = 7$ (c) $x/h = 9.5$ (d) $x/h = 12$ (e) $x/h = 14.5$ (f) $x/h = 20$*

Turbulence statistics

The experimental data obtained by Jakirlic [8] also provides material for comparison concerning the Reynolds shear stress as a function of the height. For several x-positions this stress is plotted in figure 5.30. For all x-positions the LES gives much lower values of the shear stress. Furthermore for x-positions upstream of the fence and on the fence, (a) and (b), there is almost no shear stress to be detected. One expects to see peaks of high stress values near the walls. This is a direct consequence of the inlet flow not being turbulent and this non-established inlet flow can to a certain degree explain why the LES values are systematically less negative compared to the experimental data. The Reynolds shear stress as calculated by the Re-stress model is also plotted. It must be noted that this is not the result of time-averaging but rather the instantaneous value long after

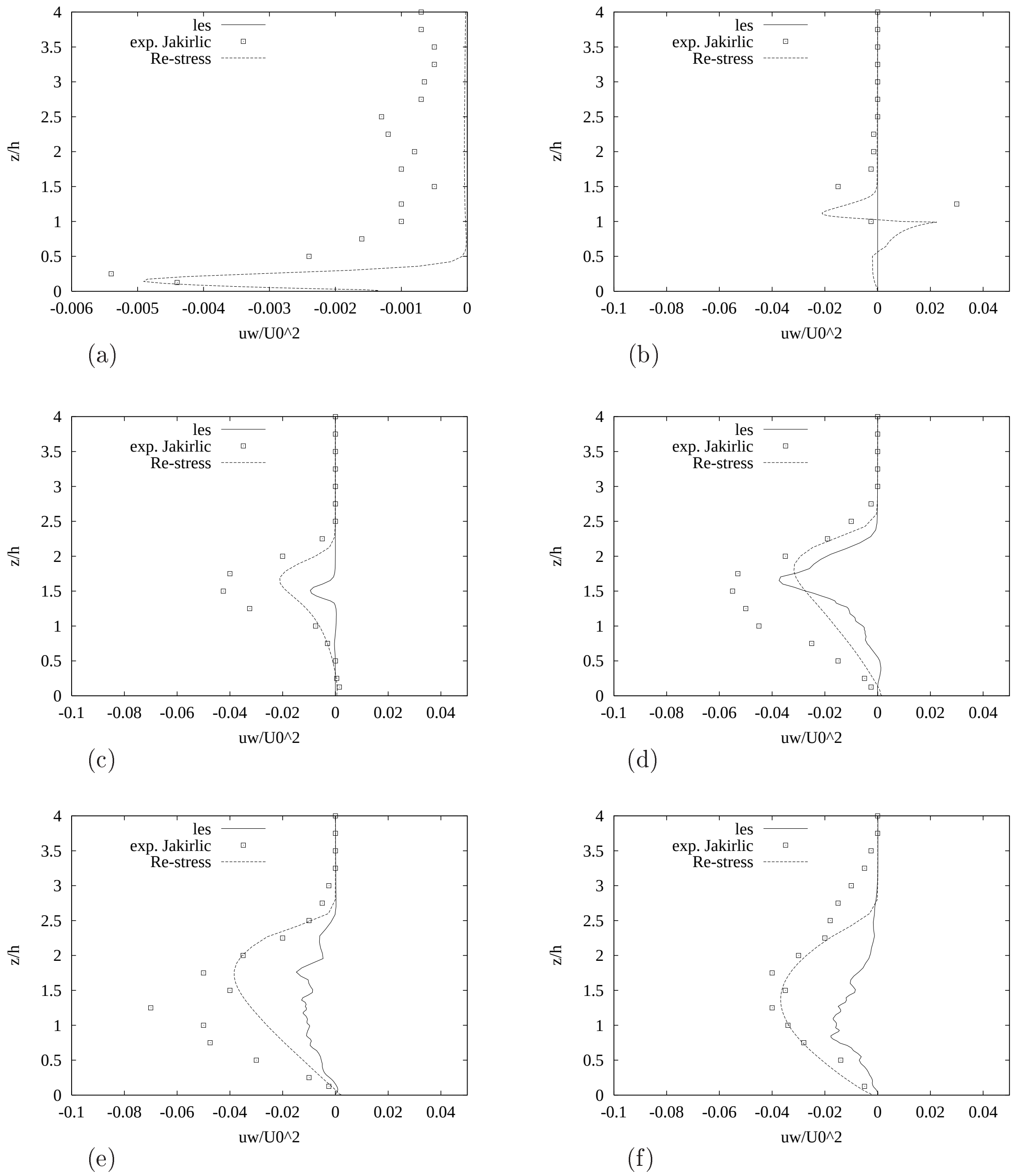

Figure 5.30: *The time-averaged Reynold shear stress* $uw/{U_0}^2$ *as a function of the height* z/h *for the following x-positions: (a)* $x/h = 4.5$ *(b)* $x/h = 7$ *(c)* $x/h = 9.5$ *(d)* $x/h = 12$ *(e)* $x/h = 14.5$ *(f)* $x/h = 20$

the flow reached a steady state, which should provide a good indication. Again the results for the Re-stress model are misplotted on the fence. As can be seen in the figure, the turbulence model produces a value of the shear stress inbetween those of the LES and the experiment. Jakirlic, who compared the experiment with simulations of his own using a.o. the turbulence models we use, also observed smaller values compared to the experiments when using the Re-stress model. Curiously the experimental data gives a positive value of the shear stress on the x-position of the fence above its top. This was also observed by Lee from his experiments, but the other simulations do not produce a positive value. Perhaps this is because we use infinitely thin fences in our simulations. Lee used a fence with a certain thickness, which results in a recirculation zone on top of the fence as we will see later on.

In figure 5.31 the turbulence kinetic energy k is plotted as a function of the height. And again the values produced by the LES are much smaller than values from the experiment. One does see the shear layer become larger when travelling downstream, a feature observed for various channel flows with obstacles. It is also obvious from graph (a) that the flow upstream of the fence is not the turbulent flow as we meant it to be. The results of the turbulence models are also plotted in the figure. Again FLUENT is unable to correctly represent the values on the fence. And again the RANS-values fall in between those of the LES and the experiment for all x-positions. Surprisingly the results from the $k-\epsilon$ model compare better to the experimental results than do the Re-stress results. Jakirlic also observed this and thought it a coincidental consequence of the weaknesses of the model. Using the $k-\epsilon$ model does not result in a perfect flow. For example there is no extra recirculation zone behind the fence. This makes it doubtful if the better results, compared to the Re-stress results, are actually an improvement.

In figure 5.32 the time-averaged subgrid energy is plotted for two different x-positions. When one compares the values to the kinetic energy for these same x-positions, figure 5.31 (c) and (d), one can conclude that the subgrid energy is small enough not to have much influence.

As an extra indication of what the effect of the subgrid model is on the flow, figure 5.33 is included. Here the total viscosity and the Reynolds viscosity are plotted as a function of the height. Both are time-averaged and shown for x-position $x/h = 12$, a x-position with a relatively high subgrid energy as could be seen from the previous figure. As can be seen the contribution of the subgrid model to the total viscosity is very small. This makes it more probable that any non-physical behaviour brought on by using a model is neglegible. One can also observe that the value of the total energy does not change much over the height of the channel.

In figure 5.34 the wall y_+ for the lower wall and for the fence is shown. From graph (a) we see that for all x-positions the values of y_+ are all well within the viscous sublayer, except for the region of the channel where the fringe method is applied. In other words all the different scales are simulated. From graph (b) one can tell the same is true for the fence. One can also see a sharp peak in the profile from graph (b), which is due to the recirculation zone in front of the fence.

Other simulations

Here we look at some extra RANS-simulations to try to explain some curiosities we have found. First of all, from figure 5.29 it followed that the u-velocities from the experiment provided by Jakirlic systematically have a higher value than the LES and the simulations using the turbulence models for z-positions above the wake. To find out whether or not this is a result from the small differences in Reynolds number and blockage ratio between the simulations and the experiment, some more simulations are performed. That is for both the $k-\epsilon$ model and the Re-stress model the simulations are repeated, but using this time a Reynolds number of $Re_h = 3000$ and a blockage ratio of $h/H = 1/7.5$, the parameters used by Jakirlic. The $k-\epsilon$ simulation has a total simulation time of $54.9t$ of which the last $12.9t$ are used for time-averaging. The Re-stress simulation has a total simulation time of $70.6t$ of which the last $10.6t$ are used for time-averaging.

For neither turbulence model the adjustement of the parameters has much impact on the velocity field. For example the time-averaged reattachment lengths remain almost equal: $x_R = 17.3h$ for the $k-\epsilon$ model (instead of $x_R = 17.2h$) and $x_R = 19.8h$ for the Re-stress model (instead of $x_R = 20.1h$). We already know from Tropea and Gackstatter [4] that for a turbulent flow x_R does not vary much with the Reynolds number.

In figure 5.35 the u-velocity profiles on the x-position of the fence is shown for both the original simulation as well as for the adjusted simulation. From both graphs it is quite clear that there is a very small increase of the maximum u-velocity. This increase however is so small that it does not justify the large difference with the experimental velocities that we have found. As already mentioned the profiles of the data from Lee compare much better to our simulations for these z-positions. Since the difference in parameters seems to give no explanation, it seems fair to assume that the experiments indeed don't compare that well themselves. This makes it much harder to verify the LES.

In our simulations we use an infinitely thin fence. The experiments on the other hand natu-

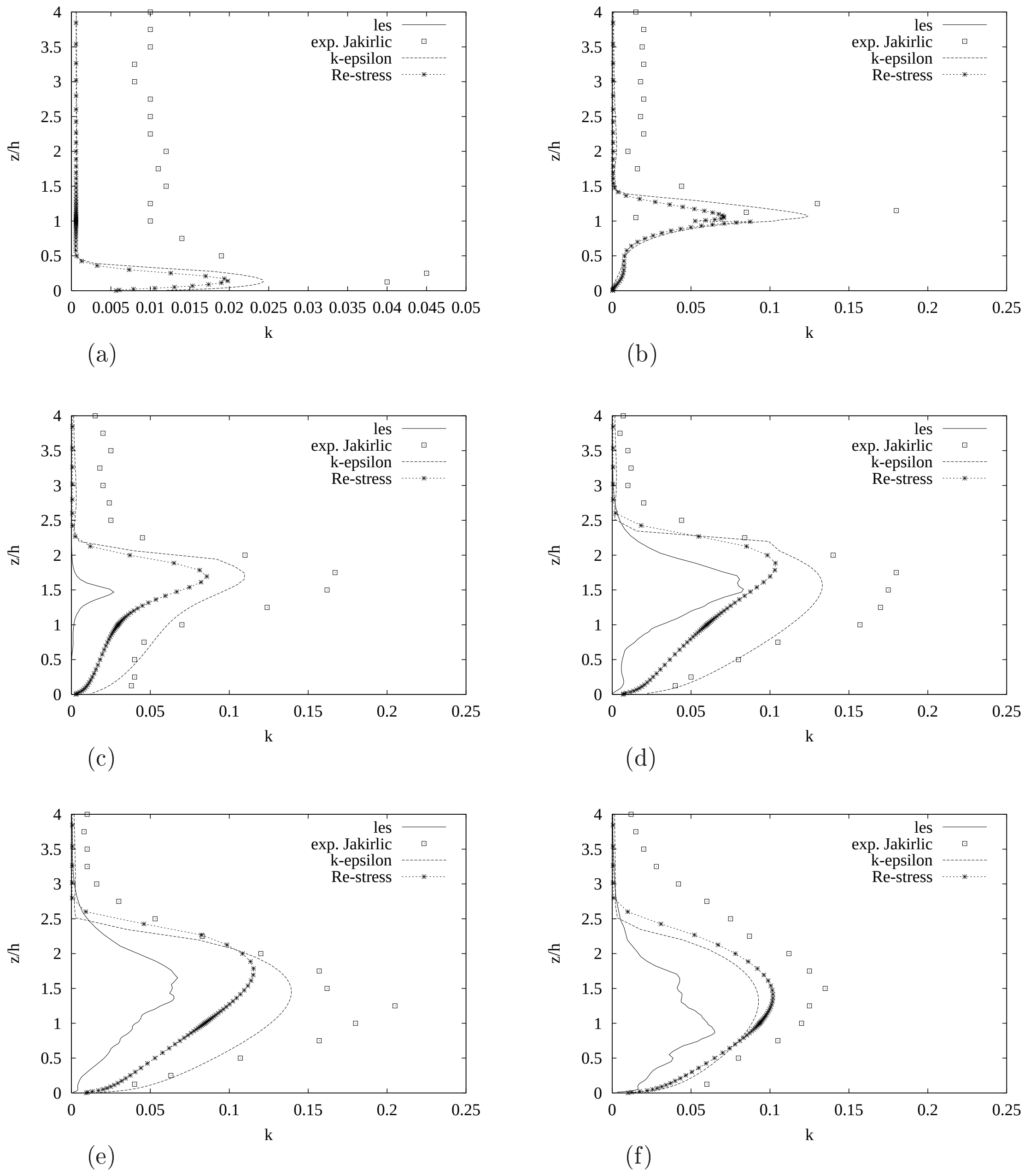

Figure 5.31: *The time-averaged turbulent kinetic energy $k/{U_0}^2$ as a function of the height z/h for the following x-positions: (a) $x/h = 4.5$ (b) $x/h = 7$ (c) $x/h = 9.5$ (d) $x/h = 12$ (e) $x/h = 14.5$ (f) $x/h = 20$*

rally were performed using a fence with a certain thickness. Specificially Lee used a fence with thickness $l/h = 0.12$ and the data of Jakirlic was produced using a fence thickness of $l/h = 0.25$. To find out what the effect is of changing this thickness two simulations, using respectively the $k - \epsilon$ model and the Re-stress model, are performed using a fence thickness of $l/h = 0.25$. The total simulation time of the $k - \epsilon$ simulation is $180t$ and of the Re-stress simulation $85.5t$. Time-averaging for the former simulation took place over $46t$ and for the latter over $43.5t$.
Some interesting results are found. For instance the reattachment lengths have become somewhat smaller. The $k - \epsilon$ simulation generates an averaged length of $x_R = 9.8h$ instead of $10.2h$ and the Re-stress simulation generates an averaged length of $x_R = 12.1h$ instead of $13.1h$. This trend agrees with the findings of Tropea and Gackstatter [4] who found smaller reattachment lengths

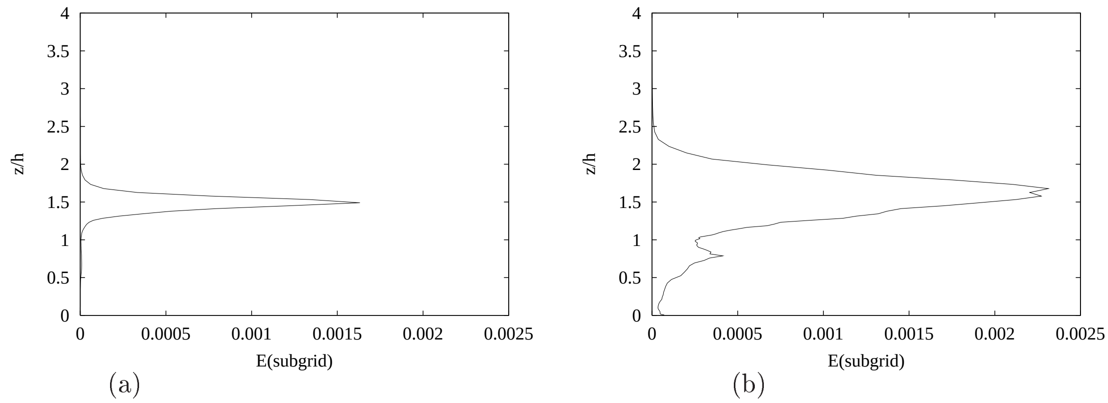

Figure 5.32: *The time-averaged subgrid energy $E_{subgrid}$ as a function of the channel height z/h on the following x-positions: (a) $x/h = 9.5$ (b) $x/h = 12$.*

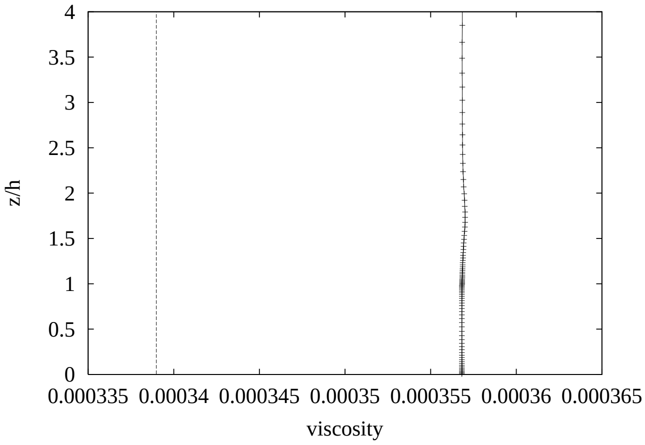

Figure 5.33: *The time-averaged viscosity as a function of the height z/h at x-position $x/h = 12$ for (dotted line:) $\mu_t + 1/Re$ and (line:) $1/Re$. Note that the viscosities on the horizontal axis do not start at zero value.*

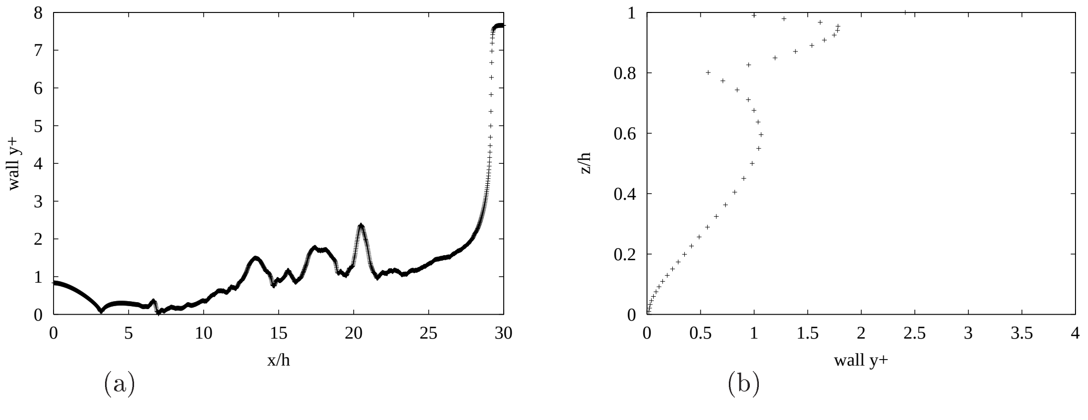

Figure 5.34: *The time-averaged wall y_+ as a function of: (a) the length of the channel x/h (b) the height of the fence z/h.*

for thicker fences. This explains to a small extent why the reattachment length from the LES

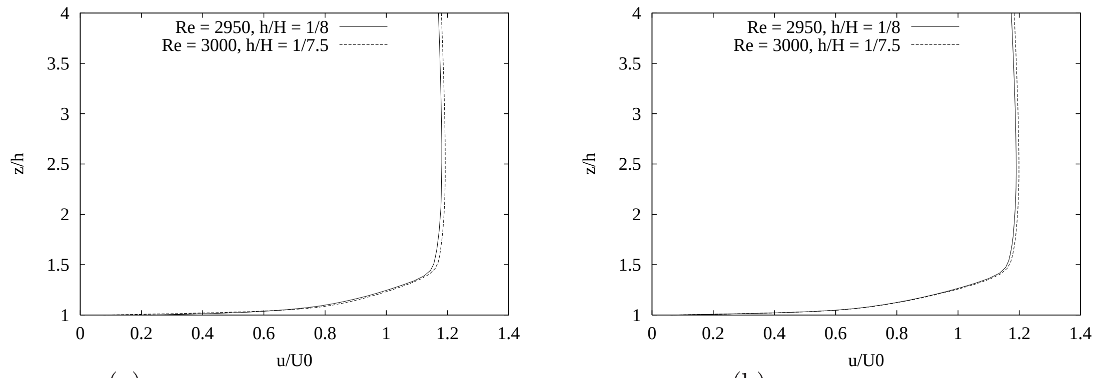

(a) (b)

Figure 5.35: *The time-averaged u-velocity u/U_0 as a function of the channel height z/h on the x-position of the fence $x/h = 7$ when using the: (a) Re-stress model (b) $k - \epsilon$ model.*

is much larger than the experimental ones. Durst and Rastogi [9] put it more strongly. They found that a fence with a sharp edge, instead of a rectangular form, consistently resulted in longer reattachment lengths. Since we use an infinitely thin fence, this could be a reason for our long reattachment lengths.
In figure 5.36 the time-averaged u-velocity profiles are shown for the x-position of the fence. The

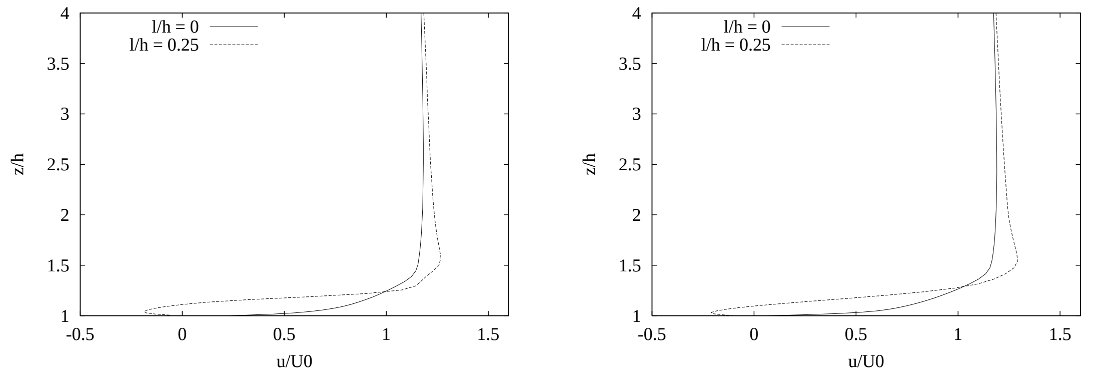

(a) (b)

Figure 5.36: *The time-averaged u-velocity u/U_0 as a function of the channel height z/h on the x-position of the fence $x/h = 7$ when using the: (a) Re-stress model (b) $k - \epsilon$ model.*

simulations with a thick fence show negative values on top of the fence also observed in the experiments (figure 5.29 (b)). Furthermore when looking at the shear stress as a function of the height, positive values (as observed in the experimental data of figure 5.30 (b)) can indeed be found on top of the fence for thick fence simulations.

Verification RANS-simulations

In order to find out whether the grid for our simulations is fine enough, several simulations are performed with twice as many grid cells for all directions. The smallest grid cells near the walls and fence keep their original size. In figure 5.37, for both the turbulent models, the time-averaged u-velocity profile is shown at the supposed ends of their wakes, i.e. $x/h = 17.2$ for the $k - \epsilon$ model and $x/h = 20.1$ for the Reynolds stress model. For both models the profiles overlap mostly. This behaviour is also observed at different x-positions and for w-velocities. This indicates we are allowed to use the somewhat coarser and therefore less time consuming grid.

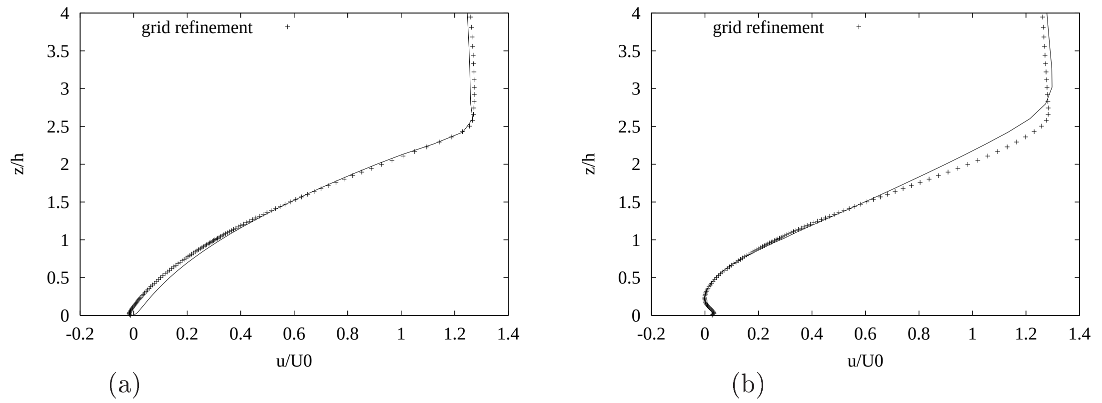

Figure 5.37: *The time-averaged downstream velocity u/U_0 as a function of the height z/h using two different grids at x-position: (a) $x/h = 17.2$ using the $k-\epsilon$ model (b) $x/h = 20.1$ using the Reynolds stress model.*

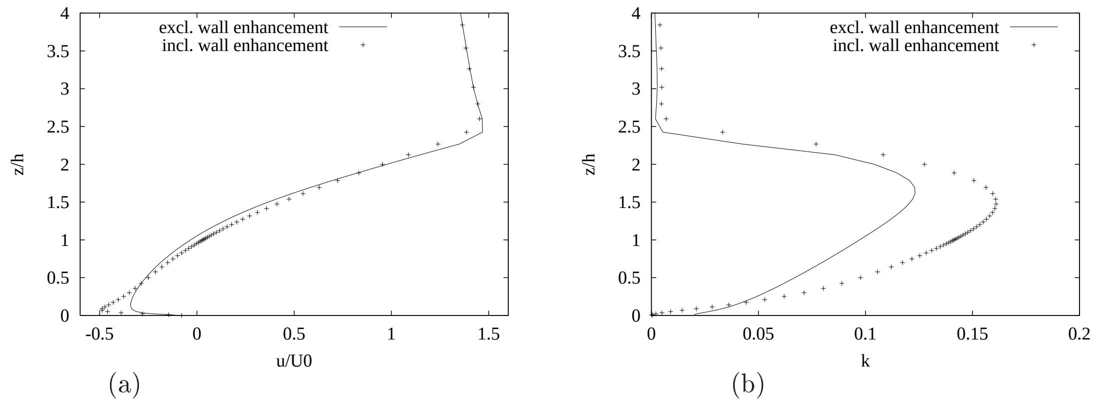

Figure 5.38: *The time-averaged results for the $k-\epsilon$ model at x-position $x/h = 11$: (a) u-velocity u/U_0 as a function of the height z/h. (b) kinetic energy $k/{U_0}^2$ as a function of the height z/h.*

Another subject of investigation is whether or not we should apply the enhanced wall treatment, as described in subsection 4.4.3. Since we use a large Reynolds number and hence have a relatively small near-wall region, this shouldn't be necessary. For both models we now perform simulations with enhanced wall treatment. In figure 5.38 and 5.39 some results are shown. In graph (a) of both figures the time-averaged u-velocity profiles are shown. The profiles near the wall are very different when comparing both turbulence models, the reason being that in the $k-\epsilon$ model the eddy viscosity μ_t is considered to be isotropic, even near a wall. The application of the enhanced wall treatment doesn't seem to have much effect on the velocity profiles, except for the $k-\epsilon$ model near the wall. The reattachment lengths however remain equal. The reason for the difference in velocity values near the wall, is unclear

In the graphs (b) of the figures the kinetic energy k is plotted as a function of the height. Again for the $k-\epsilon$ model there is a large difference with the original simulation when using the enhanced wall treatment. However not just near the wall, but over the total height of the channel. The same is true for the eddy viscosity plotted in figure 5.40.

For this particular Reynolds number, using the enhanced wall treatment does not seem to have much effect on the results of the Re-stress model. For the $k-\epsilon$ model the treatment should have been used. This follows from figure 5.41. Here the wall y_+ is shown for the lower wall and the

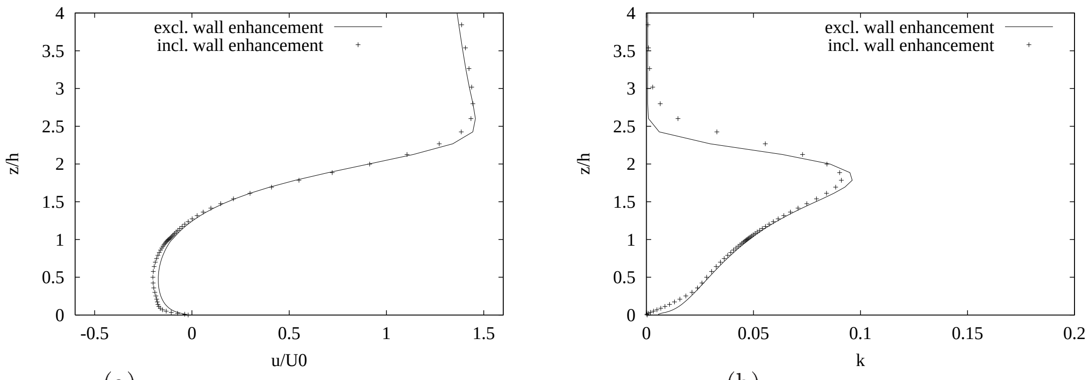

(a) (b)

Figure 5.39: *The time-averaged results for the Re-stress model at x-position* $x/h = 11$*: (a) u-velocity* u/U_0 *as a function of the height* z/h*. (b) kinetic energy* $k/{U_0}^2$ *as a function of the height* z/h*.*

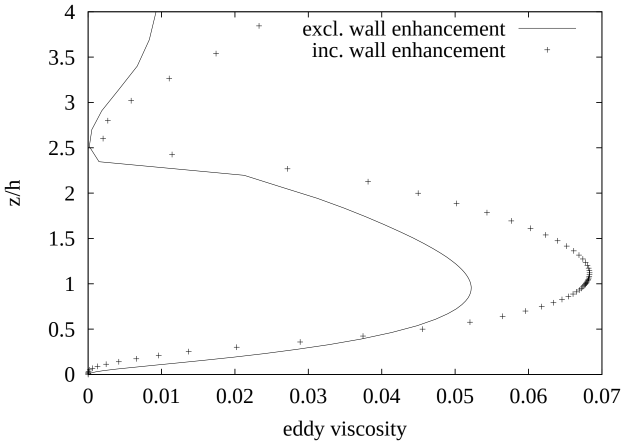

Figure 5.40: *The eddy viscosity as a function of the height* z/h *at x-position* $x/h = 11$*.*

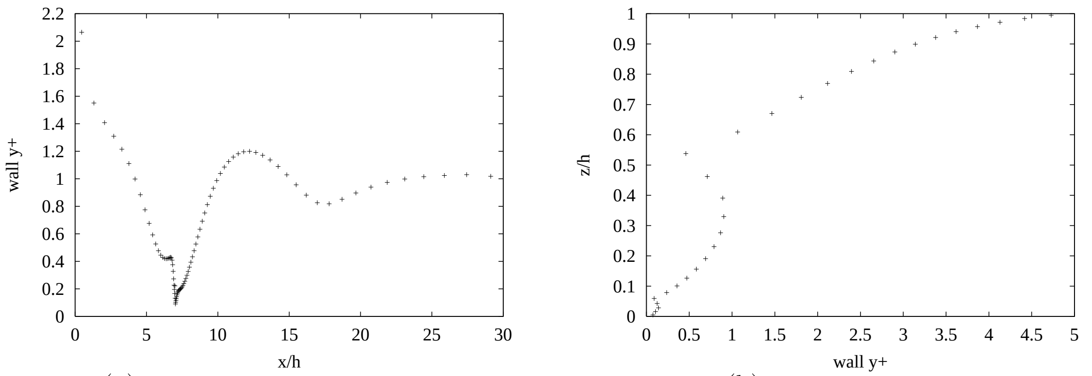

(a) (b)

Figure 5.41: *The wall* y_+ *as a function of: (a) the channel length* x/h *(b) the fence height* z/h*.*

fence. Both in graph (a) and (b) the value of the y_+ lies well within the viscous sublayer. In other words the grid is so fine that one should use the enhanced wall treatment, which should give more accurate results near the walls. When looking at the results in figure 5.31, one can see that when applying the treatment, the resulting more accurate results for the kinetic energy would deviate even more from the results of the LES and the Reynolds stress model.

5.5.2 $Re_h = 750; h/H = 1/4$

From section 5.3.1 we know that a 2-dimensional laminar flow with Reynolds number $Re_h = 750$ and a blockage ratio of $h/H = 1/4$ sheds vortices. Here we want to find out whether or not a 3-dimensional simulation, established according to section 5.4.1, also sheds vortices. Furthermore we are interested if there are any differences between a 2-dimensional and 3-dimensional simulation. And again a comparison is made to a simulation with the Re-stress model provided by FLUENT.

The channel we use has a size of $30h \times 1h \times 4h$ with a resolution of $1800 \times 20 \times 80$. For the z-direction grid refinement is applied to the lower and upper wall as well as to the top of the fence. For this direction 40 out of the 80 grid cells are used along the height of the fence. The fence is placed at a distance of $2h$ from the inlet. This is extremely close, but the distance is chosen in order to make a good comparison to the laminar case, without introducing an extra parameter, namely the upstream distance to the fence.

When looking at an instantaneous xz-plot of the streamlines in the channel produced by the

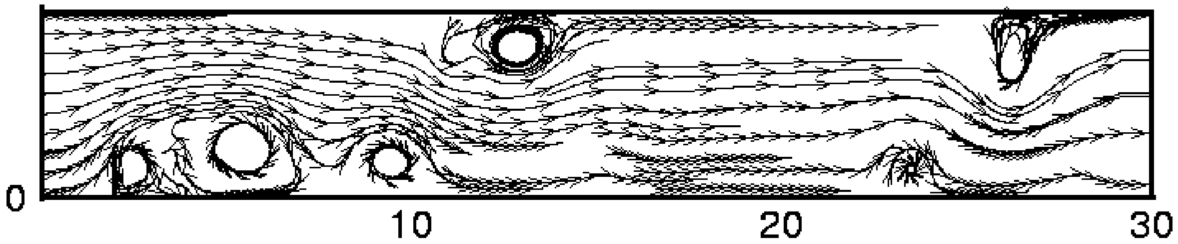

Figure 5.42: *xz-Cross-section of the channel with fence showing instantaneous streamlines.*

LES, one can clearly detect vortices. See figure 5.42. When looking at a series of these plots for successive timesteps one can see these vortices travel through the channel. However spectra of timeseries consisting of velocities show no distinct peak and therefore no reliable shedding frequency can be determined. The simulation starts off shedding large vortices in a way similar to the laminar case. But eventually the vortices become somewhat smaller and the shedding becomes more irregular. Also clear are various recirculating zones at the upper wall. These rotate counterclockwise and are therefore not the same as the shedded vortices from the fence, which rotate clockwise. They seem to originate at the upper wall around $x/h = 9$ and they too travel through the channel. We didn't encounter them in the 2-dimensional simulations performed in section **??**. This is not a result of the difference in dimension, because in the 2-dimensional simulations of section 5.3.2 (concerning particle deposition) these recirculating zones do exist. The reason for the difference is the number of gridcells for the z-direction. In the simulations of section **??** we use only 40 gridcells for the total z-direction and therefore cannot see these extra recirculating zones.

We know from Tropea, Gackstatter [4] and Peng, Hwang [3] that for some laminar fence flows an extra recirculation zone can be found at the upper wall. They found this extra zone at low Reynolds numbers and blockage ratio's of $h/H = 0.5$ and $h/H = 0.75$. However not for a blockage ratio of $h/H = 0.25$. They also don't mention these zones travelling throughout the channel, but then they neither mention the fence shedding vortices.

In figure 5.43 the time-averaged u/U_0 and u_{rms}/U_0 are shown as a function of the height z/h for positions on the fence. Both are shown to provide us with an indication of how well the force-method, discussed in section 4.3.1, works. As can be seen from (a) and (b) the method works extremely well. Both u and u_{rms} have a value of the order of 10^{-6} - 10^{-5}, neglegible compared to the velocities surrounding the fence. Since we use a staggered grid no v- and w-velocities are shown.

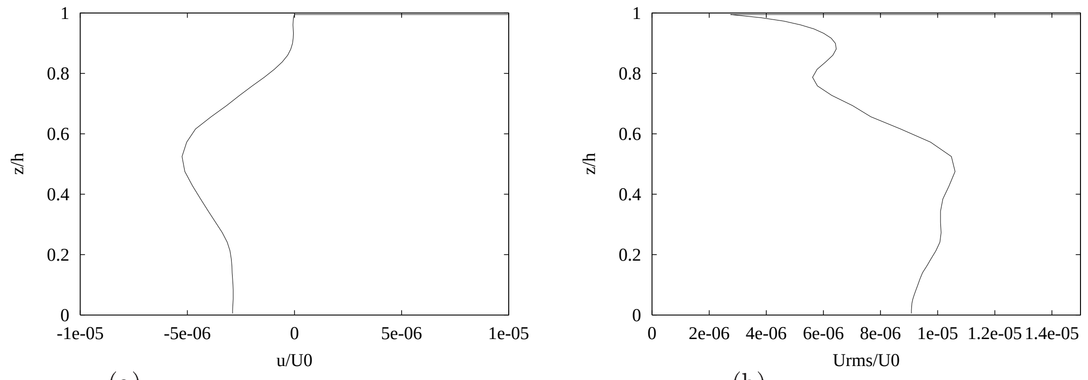

(a) (b)

Figure 5.43: *(a): The time-averaged u-velocity $u/U0$ as a function of the fence height z/h on the fence $x/h = 2$. (b): The u_{rms} as a function of the fence height z/h on the fence $x/h = 2$.*

Comparison to other simulations

Here we compare our LES to a 2-dimensional simulation using the same parameters and to a simulation that uses the Re-stress model. This last simulation is done by means of the commercial package FLUENT 6. The geometry used is equal to our LES. The grid however is, besides the z-direction, also non-equidistant for the x-direction. The smallest grid cells, present at the walls and fence, have the same size as their equals in the LES. Furthermore attention is paid that, for the x-direction, enough grid cells are present throughout the whole channel to solve possible vortices. The Re-stress model is solved using an unsteady 2nd order implicit scheme. We use an inlet velocity of $U = 1m/s$ with no V- or W-components similar to the inlet condition of the LES. Since we use a small Reynolds number we apply the enhanced wall treatment for the near-wall region. The simulation is performed using a fixed timestep of $0.001s$. The total simulation time is $152t$. The last $100t$ are used for time-averaging.

For the 3-dimensional simulation we find a reattachment length of $x_R = 7.7h$. For the 2-dimensional simulation we have found a reattachment length of $x_R = 6.9h$, a decline of 10%. This complies well with the findings of Peng and Hwang [3] who performed a 2- and 3-dimensional simulation of a certain fence flow. When stepping from a 3-dimensional to a 2-dimensional flow, they found a decline of the reattachment length of 14%, a value near our 10%. When we perform the simulation using the Re-stress model, we find a much larger reattachment length of $x_R = 11.5h$. However, in contrast to the LES and laminar simulation, no shedding of vortices takes place. Although at the start of the simulation vortices are shed, this soon stops. This lack of shedding could well be the reason that the reattachment length is much longer for the Re-stress model.

In figure 5.44, for two x-positions, the time-averaged streamwise velocity profiles are shown for all three simulations. For all x-positions upstream of the fence and of the fence itself, the profiles overlap one another nicely. Downstream however they deviate from one another and it seems that the longer the recirculation zone the less the value of their negative u-velocities. This last trend is valid for all x-positions in the wake.

Next we look at some graphs depicting the $\mathbf{u}_{rms}$ as a function of the height z/h of the channel for all three simulations. In figure 5.45 the RMS-profiles are shown for x-position $x/h = 5$. For all three simulations this is a x-position within the wake. When we compare the RMS-values of all these simulations it is apparent that the 2-dimensional simulation has the largest values for both the u_{rms} and w_{rms}. The Re-stress model has the smallest values. The w_{rms} values in figure 5.46 are in comparison to the other simulations so small, they cannot even be detected. The RMS-values give us an indication of how strong the vortices are. We know that using the Re-stress model results in a flow where no shedding takes place, which could be the reason that we find

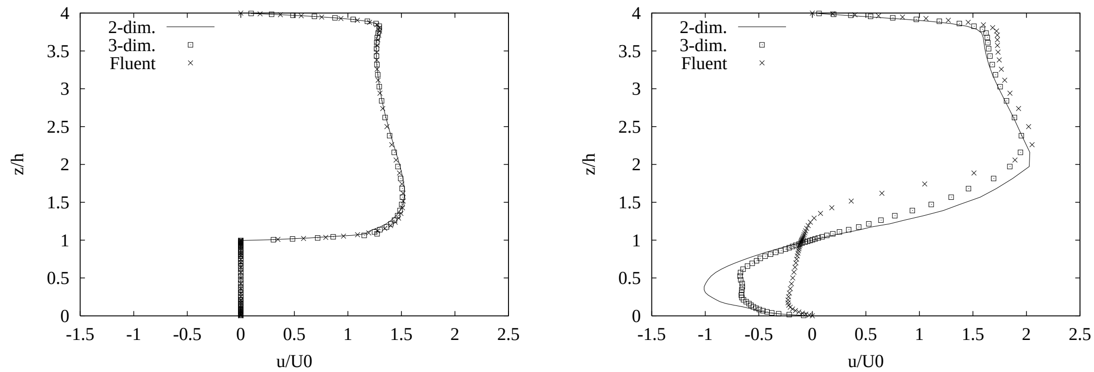

(a) (b)

Figure 5.44: *The time-averaged u-velocity u/U_0 as a function of the height z/h for the following x-positions: (a) $x/h = 2$ (b) $x/h = 5$*

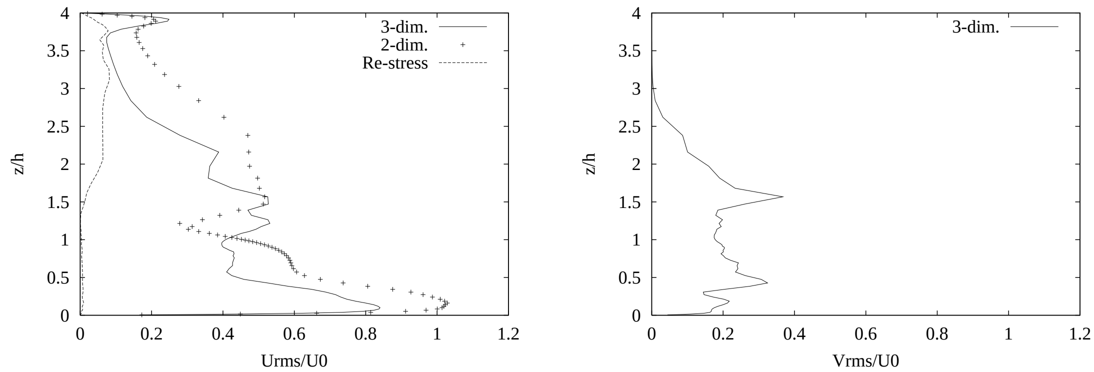

(a) (b)

Figure 5.45: *The u- and v-rms-values, u_{rms}/U_0 and v_{rms}/U_0, at x-position $x/h = 5$ as a function of the height z/h for the 2- and 3-dimensional and RANS simulation.*

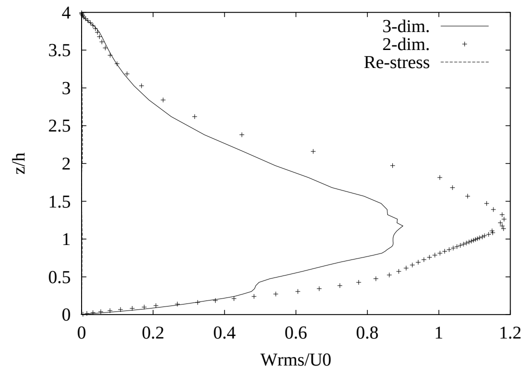

Figure 5.46: *The w-rms-values w_{rms}/U_0 at x-position $x/h = 5$ as a function of the height z/h for the 2- and 3-dimensional and RANS simulation.*

very small RMS-velocities. For the 3-dimensional, i.e. the LES, simulation we already observed the shedded vortices being somewhat smaller than those in the 2-dimensional case. This is due to the fact that of all the energy available for the vortices in the 2-dimensional simulation, for the 3-dimensional simulation some of it goes to the resolved turbulence and the subgrid turbulence. Hence for the 3-dimensional simulation, the vortices are less strong and this results in the smaller

RMS-values.

When we look somewhat further downstream, at x-position $x/h = 10$, we find the profiles

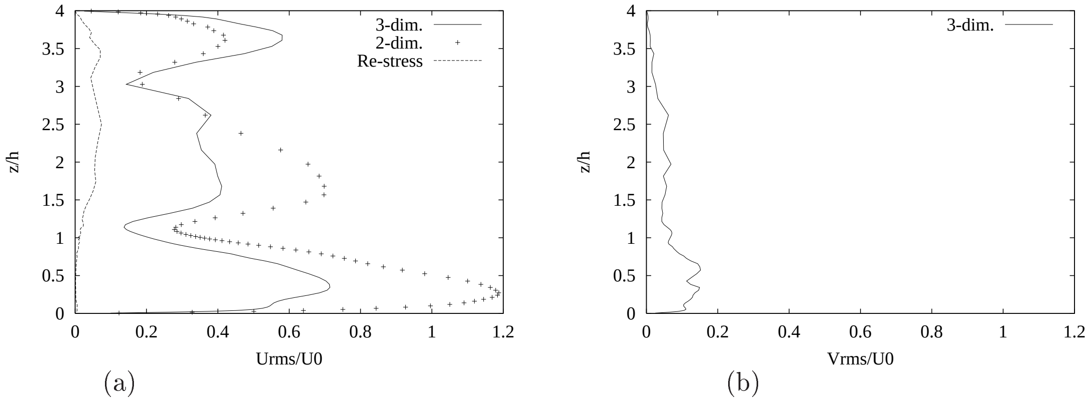

Figure 5.47: *The u- and v-rms-values, u_{rms}/U_0 and v_{rms}/U_0, at x-position $x/h = 10$ as a function of the height z/h for the 2- and 3-dimensional and RANS simulation.*

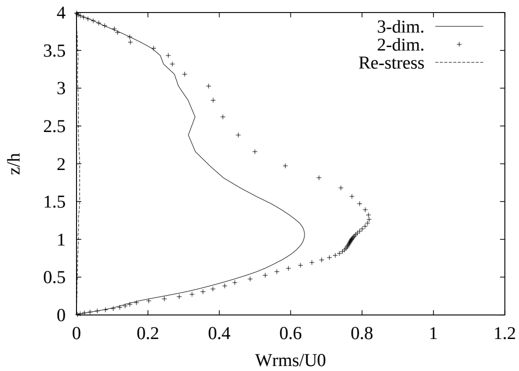

Figure 5.48: *The w-rms-values w_{rms}/U_0 at x-position $x/h = 10$ as a function of the height z/h for the 2- and 3-dimensional and RANS simulation.*

shown in figure 5.47 and 5.48. For the Re-stress model we find roughly the same profiles as in the previous figure, because we are still in its recirculation zone. The other two simulations have got a distinctively different profile. We are now at a x-position beyond both their wakes. Both dents in the profiles of u_{rms} cannot just be there due to the existence of respectively the vortex shedded from the fence and the upper wall. The laminar simulation after all did not show vortices at the upper wall. Furthermore in the w_{rms} profile the 2nd peak, corresponding to the dent, is not so clear. It must be said that the profile is shown for a x-position near the one where the upper wall vortices originate and where these vortices are therefore still very small. When looking at the u_{rms}-profiles one can also distinguish three peaks besides the two dents. The two peaks, and thus the two dents, originating near the walls are not just the beginning of peaks due to turbulence normally found when looking at u_{rms}-profiles of fenceless channels, since they also appear for the 2-dimensional situation.

Particles

After the flow has established itself we introduce different particles to the simulation in the same manner as the first simulation described in section 5.3.2. Summarized this means particles with four different relaxation times ($\tau_p = 4 * 10^{-4}$, $\tau_p = 0.04$, $\tau_p = 0.4$ and $\tau_p = 4$), for every relaxation time 5000 particles, an elastic collision routine as boundary condition for the channel walls and fence and no gravity acting on the particles. The results are shown in figure 5.49. The behaviour

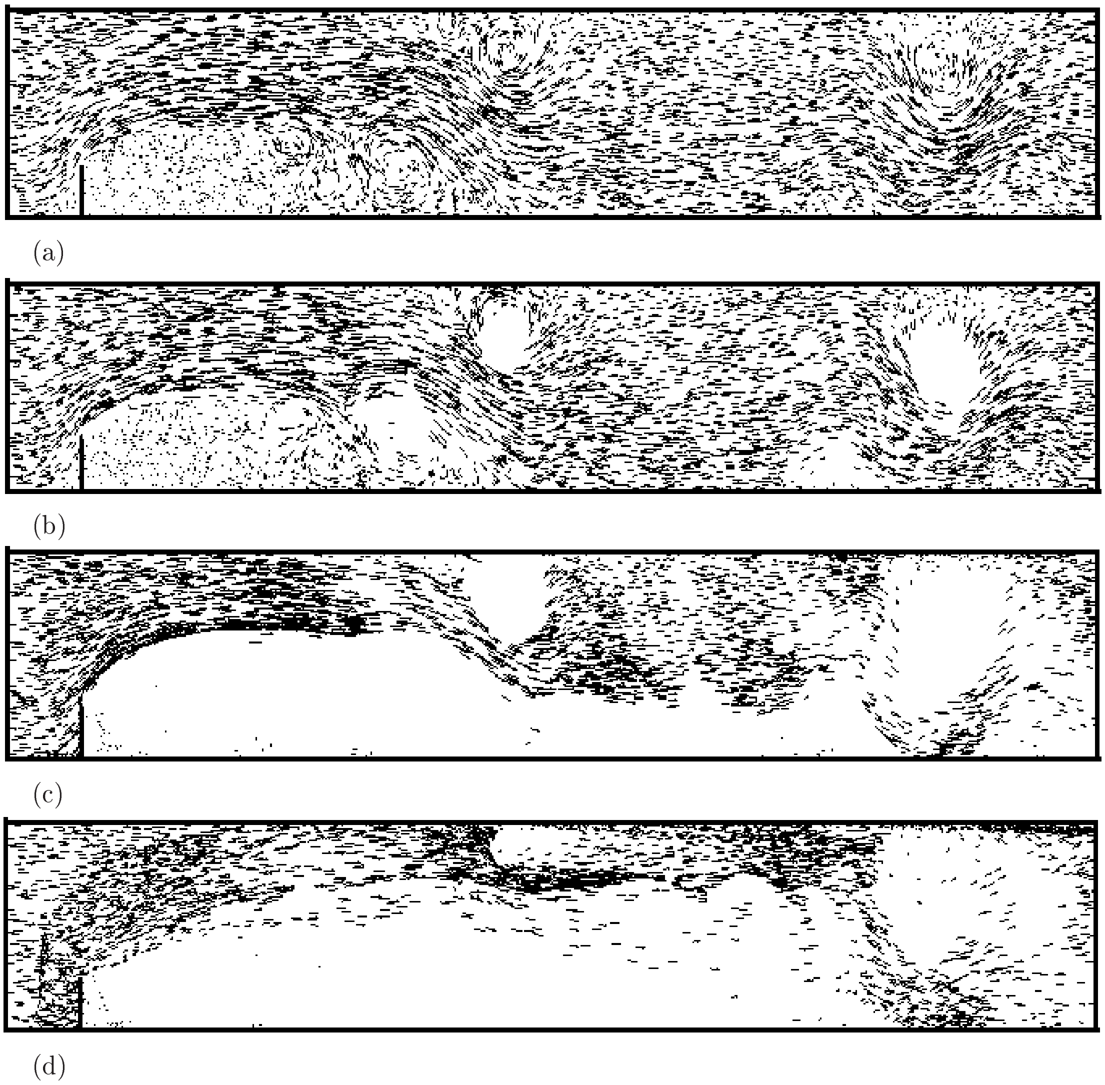

Figure 5.49: *xz-Cross section of the channel with the velocity vectors of the particles plotted at their instantaneous positions for (a)* $\tau_p = 0.0004$ *(b)* $\tau_p = 0.04$ *(c)* $\tau_p = 0.4$ *(d)* $\tau_p = 4$

is less convincing than the one shown in picture 5.19 for the laminar case. Probably because the vortices, which are supposed to influence the particle behaviour, are somewhat weaker compared to the laminar case.

We perform the same simulation, including the particles, using the commercial package FLUENT 6. We do this making use of the Reynolds stress model with enhanced wall-treatment. The calculation of the particle trajectories in FLUENT is based on the same equation as was discussed in section 4.5.1 (equation 4.65). In order to predict possible dispersion of particles due to turbulence, the package uses a stochastic method to determine the instantanious flow velocity. The values of its fluctuating components are kept constant over an interval of time

$$\mathbf{u}' = \zeta\sqrt{\overline{\mathbf{u}'^2}} \tag{5.8}$$

with ζ a normally distributed random number. The mentioned interval of time is determined by the characteristic lifetime of eddies. This characteristic lifetime of the eddy is defined as a random variation about T where the integral time scale T is given by

$$T \approx 0.30 \frac{k}{\epsilon} \tag{5.9}$$

When this time characteristic eddy lifetime is reached a new value of the instantaneous velocity is obtained by applying a new value of ζ in 5.8.

This is the method used by the package to calculate the particle trajectories. All the conditions applied in the previous discussed Re-stress simulation are also applied when making use of the particle routine provided by the package. Among other things the gravity force is ignored and the same particle boundary conditions are applied to the upper/lower wall and the fence. When a particle reaches the outlet of the channel it is taken out of the simulation and unlike the previous simulation it is not reintroduced at the inlet. This falls not within the capabilities of the package. The particle routine available in FLUENT 6 has some more serious restrictions:

- When injecting the particles the package is not able to randomize the particle positions over the inlet of the channel. It positions the particles uniform over the inlet, thereby influencing possible statistics. When using a User Defined Function (UDF-) routine which takes care of this randomizing, the package no longer works correctly. It randomly aborts particle trajectories.
- The package can only inject particles every single timestep, not every other timestep or twice per timestep. Since we want to limit the amount of particles in the channel in order to prevent the simulation becoming extremely slow, we have to choose between a very large timestep or a really small number of particles to inject every timestep. This forces us to find a balance, deviating from the conditions of the simulations we want to compare to.
- The particle statistics provided by the package have shortcomings. For example the package is unable to calculate the particle concentrations for one-way coupling. This forces one to write so-called user-defined routines, which for the case of the particle concentrations we were unable to do. Furthermore when stopping a simulation including particles at a time when the package is calculating the discrete phase, all the current positions of the particles are lost. In order to recover them one has to calculate one timestep without the particle routine and switch the routine back on in the next timestep. This makes the routine hardly efficient.

All these restrictions make it very hard to make a good quantative comparison. Unlike the previous simulation we cannot work with a constant number of particles. We'll have to use a larger timestep and a different injection condition on the inlet.

In figure 5.50 the instaneous particle positions for the different particle relaxation times are shown, calculated by the package. When we compare these graphs to those depicted in figure 5.49 some very general aspects can be noted. When concentrating at the wake directly behind the fence, in both figures the trend is found that the larger the relaxation time of the particles the less they get trapped in the wake. In both figure's graph (c) one can find a somewhat higher concentration of particles in the shear layer sharply visualizing the edge of the wake, that is the wake directly behind the fence. And in (d) in both figures one can clearly see the particles bounce back from the fence to about one fencelength. Also apparent here, are a group of particles with somewhat horizontal trajectories ignoring the wake. Summarizing one can say that concerning the particle results of the package no hard conclusions can be made. First of all because the RANS-simulation does not shed vortices. Second the package has enough complications, as listed above, to prevent us from making a sound quantative comparison.

Since we are still interested in the particle behaviour around vortices, the same simulation is performed using the laminar model provided by FLUENT. Applying this laminar model results in the fence shedding vortices. For the particles with $\tau_p = 0.04$ their instantaneous positions are shown in figure 5.51. They indeed show the distinctive behaviour we encountered before.

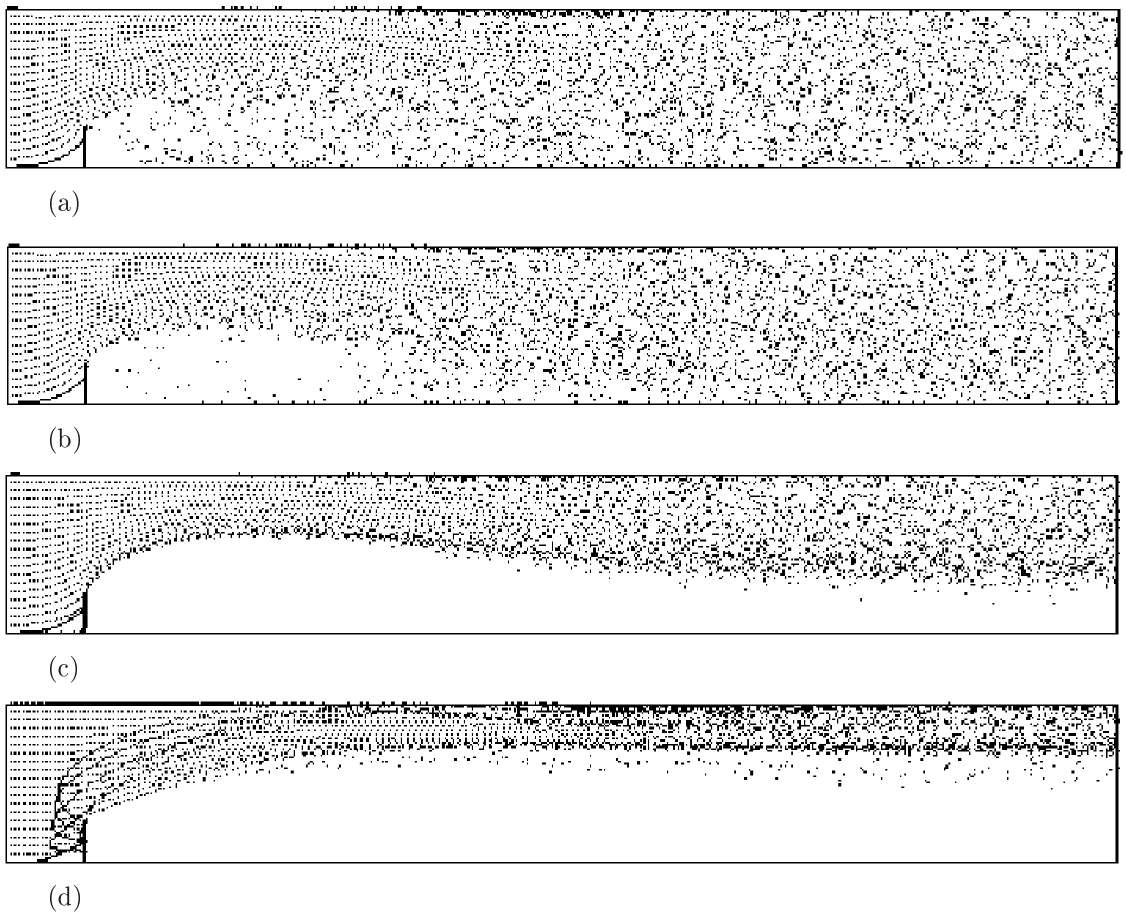

Figure 5.50: *xz-Cross section of the channel produced by FLUENT depicting the instantaneous particle positions for (a)* $\tau_p = 0.0004$ *(b)* $\tau_p = 0.04$ *(c)* $\tau_p = 0.4$ *(d)* $\tau_p = 4$

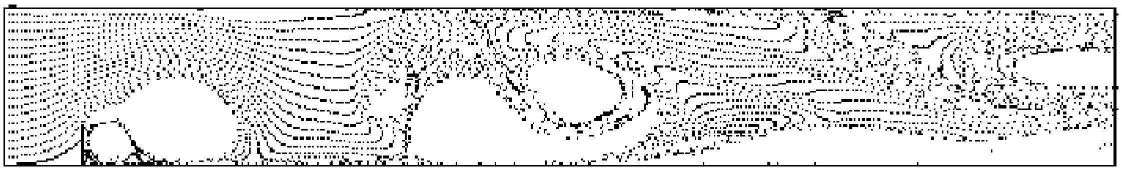

Figure 5.51: *xz-Cross section of the channel produced by FLUENT depicting the instantaneous particle positions for* $\tau_p = 0.04$

Chapter 6

Conclusions

This section is divided in four parts, each one containing the various conclusions made concerning the three goals set in the introduction plus an extra part concerning the numerical aspects of this study.

Numerical aspects

From the start of this study we have found the need for very high resolutions for the particular geometry we use. Lack of resolution resulted in wiggles and a dent in the velocity profiles and not all the recirculation zones around the fence could be seen. This finding, concerning the numerical grid, was also encountered by others for fence flow, like Durst and Rastogi [9]. Just like them, we are "...somewhat disconcerted about the requirements of such fine grids for separated flow, and about the corresponding long computing times." Orellano and Wengle [2] encountered this same requirement of high resolution and even have neglected to resolve the resulting wiggles entirely to save computation time. To make things worse we have been forced to use an equidistant grid in this study, in contrast to the mentioned authors, since we wanted to be sure that possible vortices could also be seen at the end of the channel. This increases the amount of grid cells in the x-direction considerably and hence the computation time, because of the need for a large downstream channel for fence flows.

General flow characteristics

Several observations were made concerning the general behaviour for fence. We found the height of the wake to be around two times the fence height, regardless of the Reynolds number and blockage ratio. A property ascribed to fence flow in the literature. For certain low Reynolds numbers and high blockage ratio's we find recirculation zones on the upper wall, a phenomenon which is very sensitive to the mentioned parameters. Also we found that the longer the reattachment length, the less the values of u-velocities in the wake. Making use of a thick fence instead of a infinitely small fence results in smaller reattachment lengths and an extra recirculation zone on top of the fence.

Concerning the two ideas of separating particles from parts of the flow, described in the introduction, we can state the following. When using two fences with the second fence within a certain distance of the first fence, the shear layer originating from this first fence will bend towards the top of the second fence. The impact this will have on the particles is described further on.

The second idea concerns using the shedding of vortices. The literature is not very clear about this shedding phenomenon. When adressed at all, the literature is very vague about it. For this shedding we can make some conclusions. For a blockage ratio of $h/H = 1/4$ we found that shedding takes place only for a certain range of Reynolds numbers. We find that no shedding takes place for laminar flows with $Re_h \leq 125$ and turbulent flows with $Re_h \geq 3333$. We also claim that whether or not the fence sheds vortices, has a big impact on the reattachment length. For both laminar and turbulent flows vortex shedding reduces the reattachment length strongly.

For laminar fence flows some more conclusions can be made regarding the effect of increasing the Reynolds number. Increasing the Reynolds number results in somewhat longer reattachment lengths and seems to result in vortices that stay stronger for a longer distance. The Reynolds number does not have any effect on the Strouhal number. The phenomenon of shedding seems to be very sensitive for the Reynolds number.

Concerning the differences between a 2- and 3-dimensional run we can state two things. First a 3-dimensional simulation will result in a wake with a larger recirculation zone. Second, when vortices are shed, they will be less strong in the 3-dimensional case.

Particles

We have seen that for a geometry, where a second higher fence is placed close to a first lower fence, most particles are swept over both fences. The second fence however is intended for the particles to collide with and get caught in the wake. Hence the principle does not work for the particular particles we used.

In the two-fence application where the second fence is placed further away from the first fence, we expected to be able to to use the particle/vortex interaction to get separation. Concerning this interaction we have found that different sizes of particles behave differently around vortices. We saw small particles ($St < 1$) follow the streamlines of the flow and hence be present in the vortices and wake. Large particles ($St > 1$) on the other hand were unaffected by the flow. Intermediate sizes of particles ($St \approx 1$) were found to accumulate at the edges of the vortices and wake.

When we placed a second fence further downstream, we indeed found that when particles are confined by vortices ($\tau_p = 0.4$), placing a second fence will increase deposition. However when particles are not effected by vortices ($\tau_p = 4$), placing a second fence is of no use. Furthermore these unaffected particles ($\tau_p = 4$) deposit better than the confined particles ($\tau_p = 0.4$). It appears that using no fences at all for particle deposition might be much more beneficial, since we know that in a fenceless channel small particles will accumulate near the walls anyway. Very large particles however will in theory accumulate in the center of the channel. For this range of particles it could be useful to use the principle of the patent. The only drawback is one has to create strong enough vortices and this strongness of the vortices is very sensitive on the Reynolds number.

RANS-simulations vs. LES

Both the turbulence models, the $k-\epsilon$ model and Re-stress model, as provided by FLUENT seemed to result in simulations which compare better to the experimental data than did the LES using $Re_h = 2950$ and $h/H = 1/8$. Especially when studying the shear stress and kinetic energy, the simulations using the turbulence models give results that approach the experimental data better than the LES. We know now that to a certain degree this is due to differences at the inlet between the LES and RANS-simulations, since for the LES the flow in the extra channel had not established itself. The $k-\epsilon$ model seems to work even better than the Re-stress model. However the $k-\epsilon$ model does not see the second small recirculation zone behind the fence, which is present in the experiments, LES and Re-stress simulation. From this we conclude that the seemingly better performance of the $k-\epsilon$ model is probably coincidental, something which was also observed by Jakirlic [8]. The use of the Re-stress model to simulate a fence flow seems to be reasonably justified.

However when using RANS-simulations to simulate the low Reynolds number fence flow ($Re_h = 750, h/H = 1/4$), no shedded vortices were found in contrast to a LES of the same particular fence flow. This is true for both the $k-\epsilon$ and Re-stress model. This discrepancy in shedding, results in huge differences in both velocities, rms-velocities and reattachment lengths between the LES and RANS-simulations. Hence using the Re-stress model to simulate a fence flow which sheds vortices is not justified. This means that using the Re-stress model to simulate particle/vortex interaction becomes useless. In other words the Re-stress model can only be applied to fence flow when it is known in advance that in physical reality the fence won't shed vortices.

Concerning the particle routine in FLUENT we cannot make any hard conclusions. An exact comparison could not be made since in the RANS-simulations no shedding of vortices took place and particle statistics were not available. For a laminar simulation using FLUENT, where vortex shedding did take place, the particles seem to behave in a similar fashion to our own simulations. Also it must be noted that the commercial package FLUENT 6 is not that efficient to work with, due to several bugs in the package concerning the simulation of both the flow and the particles.

Finally we can note that simulating a channel flow with a surface-mounted fence is much more complicated than anticipated. It appears that a fence flow is very sensitive for both numerical and physical aspects. The most important numerical aspect being the resolution resulting in very high computation times for our simulations. Some of the physical aspects, besides the Reynolds number and blockage ratio, are the thickness of the fence and the geometrical shape of the top of the fence. Moreover the phenomenon of clear vortex shedding cannot be taken for granted. Since it is very sensitive to a.o. the Reynolds number, it is not just applicable to any physical situation.

Bibliography

[1] Fang, F., Hsieh W.D., Jong S.W. and She, J.J., 1997. Unsteady turbulent flow past solid fence. *Journal of Hydraulic Engineering*, **123**, 560-565.

[2] Orellano, A. and Wengle, H., 2000. Numerical simulation (DNS and LES) of manipulated turbulent boundary layer flow over a surface-mounted fence. *Eur. J. Mech. B*, **19**, 765-788.

[3] Peng, Y.H. and Hwang, R.R., 1999. On the three-dimensional study of flows over a fence in a duct. *International Journal of Computational Fluid Dynamics*, **12**, 119-132.

[4] Tropea, C.D. and Gackstatter, R., 1985. The flow over two-dimensional surface-mounted obstacles at low Reynolds numbers. *Journal of Fluids Engineering*, **107**, 489-494.

[5] Wai, P.C. and Rogers, S. Liquid metal launder. *United States Patent.* Number: 4,869,750 Date: 26 Sep 1989. Alcan International Limited.

[6] Lundbladh A., Schmid P.S., Berlin S., Henningson D.S., 1994. Simulations of bypass transition for spatially evolving disturbances. *AGARD-CP-551*, 18.1-18.13.

[7] Lee, S.J., 1999. Development of two-frame PTV system and application to a turbulent separated fence flow. *3rd ASME/JSME Joint Fluids Engineering Conference*, San Francisco, California.

[8] Jakirlic, S.Z., 1997. Reynolds-Spannungs-Modellierung komplexer turbulenter Strömungen. *Ph.D. thesis.* Universität Erlangen-Nürnberg, Erlangen, Deutschland.

[9] Durst, F. and Rastogi, A.K., 1980. Turbulent flow over two-dimensional fences. *Turbulent Shear Flows* **2**, 218-232.

[10] Heist, D.K. and Gouldin, F.C., 1997. Turbulent flow normal to a triangular cylinder. *Journal of Fluid Mechanics*, **331**, 107-125.

[11] Fadlun E.A., Verzicco R., Orlandi P., Mohd-Yusof J., 2000. Combined immersed-boundary finite-difference methods for three-dimensional complex flow simulations. *Journal of Computational Physics* **161**, 35-60.

[12] Moin, P. and Kim, J., 1982. Numerical investigation of turbulent channel flow. *Journal of Fluid Mechanics*, **118**, 341-377.

[13] Mols, B., 1999. Particle dispersion and deposition in horizontal turbulent channel and tube flows. *Ph.D. thesis.* Delft University of Technology.